

Washington University in St. Louis

Washington University Open Scholarship

McKelvey School of Engineering Theses & Dissertations

McKelvey School of Engineering

Winter 12-15-2017

Two-component Hydrogel as Biomimetic Vitreous Substitutes

Sruthi Santhanam

Washington University in St. Louis

Follow this and additional works at: https://openscholarship.wustl.edu/eng_etds



Part of the [Chemical Engineering Commons](#), [Ophthalmology Commons](#), and the [Polymer Chemistry Commons](#)

Recommended Citation

Santhanam, Sruthi, "Two-component Hydrogel as Biomimetic Vitreous Substitutes" (2017). *McKelvey School of Engineering Theses & Dissertations*. 296.
https://openscholarship.wustl.edu/eng_etds/296

This Dissertation is brought to you for free and open access by the McKelvey School of Engineering at Washington University Open Scholarship. It has been accepted for inclusion in McKelvey School of Engineering Theses & Dissertations by an authorized administrator of Washington University Open Scholarship. For more information, please contact digital@wumail.wustl.edu.

WASHINGTON UNIVERSITY IN ST. LOUIS

School of Engineering and Applied Science
Department of Energy, Environmental, and Chemical Engineering

Dissertation Examination Committee:

Nathan Ravi, Chair

Marcus Foston

Daniel Giammar

Rithwick Rajagopal

Palghat Ramachandran

Srikanth Singamaneni

Two-component Hydrogel as Biomimetic Vitreous Substitutes

by

Sruthi Santhanam

A dissertation presented to
The Graduate School
of Washington University in
partial fulfillment of the
requirements for the degree
of Doctor of Philosophy

December 2017
St. Louis, Missouri

© 2017, Sruthi Santhanam

Table of Contents

List of Figures	v
List of Tables	xii
Acknowledgments.....	xiii
Abstract of the Dissertation	xv
Chapter 1: Introduction	1
1.1 Vitreous humor.....	1
1.1.1 Structural Macromolecules and their Bio-Synthesis.....	1
1.1.2 Functions and Properties.....	3
1.1.3 Pathology and Pathophysiology.....	9
1.2 Vitrectomy and Vitreous Substitutes.....	10
1.2.1 Polymeric Hydrogels as Potential Vitreous Substitutes.....	11
1.3 Research Objectives	15
Chapter 2: Synthesis of the Two-Component Hydrogels	18
2.1 Materials and Methods	18
2.1.1 Materials	18
2.1.2. Thiolation of Gellan.....	18
2.1.3. Synthesis of poly(MAM-co-MAA-co-BMAC)	19
2.1.4 Characterizations of the Polymers	20
2.2 Results and Discussion.....	22
2.2.1 Thiolation and Characterization of Gellan.....	22
2.2.2 Synthesis and Characterizations of poly(MAM-co-MAA-co-BMAC).....	25
2.2.3 Development of Two-Component Hydrogels.....	28
2.3 Conclusions	30
Chapter 3: Network Properties of the Two-Component Hydrogels	31
3.1 Materials and Methods	31
3.1.1 Materials	31
3.1.2 Response Surface Method Design	32
3.1.3 Two-Component Hydrogels Preparation	33
3.1.4 Sol-Gel Transition Temperature Measurements	34

3.1.5	Shear Modulus Measurements	34
3.1.6	Osmotic Swelling Behavior of Hydrogels	35
3.1.7	Optical and Physical Properties of Hydrogels	36
3.1.8	Oxygen Transport Studies.....	37
3.1.9	Statistical Analysis.....	44
3.2	Results and Discussion.....	44
3.2.1	Sol-Gel Transition Temperature Characteristics of Hydrogels.....	46
3.2.2	Rheological Characteristics of Hydrogels.....	50
3.2.3	Osmotic Swelling Characteristics of Hydrogels	53
3.2.4	Osmotic Swelling Characteristics of the Native Vitreous.....	56
3.2.5	Optimization of Hydrogels.....	59
3.2.5	Osmotic Swelling Pressure Produced by the Two Optimized Hydrogels.....	61
3.2.6	Oxygen Transport through the Two Optimized Hydrogels	62
3.3	Conclusions	70
Chapter 4: Biocompatibility of the Two-Component Hydrogels		72
4.1	Materials and Methods	72
4.1.1	Materials	72
4.1.2	Isolation of Primary Porcine Retinal Pigment Epithelial Cells.....	73
4.1.3	Growth of Cell Lines.....	73
4.1.4	Hydrogel Preparation.....	74
4.1.5	<i>In Vitro</i> Biocompatibility Tests.....	75
4.1.6	Degradation Studies	77
4.1.7	Animal Preparation and Study Protocol.....	78
4.1.8	Vitreotomy and Injection of Vitreous Substitute	78
4.1.9	Rabbit Pre- and Post-operative Examinations.....	79
4.1.10	Statistical Analysis.....	82
4.2	Results and Discussion.....	83
4.2.1	Growth Curves of Different Cell Lines.....	83
4.2.2	<i>In Vitro</i> Biocompatibility and Proliferation Tests for Hydrogels	87
4.2.3	<i>In Vitro</i> Degradation of Hydrogels	97
4.2.4	Biocompatibility Evaluations of Hydrogels on Rabbits.....	98
4.2.5	<i>In Vivo</i> Oxygen Tension Evaluations for Vitreous Substitutes.....	107
4.3	Conclusions	109

Chapter 5: Conclusions and Recommendations	111
References.....	115
Appendix A.....	125
Response Surface Methodology	125
A1 Experimental Design Development	126
A1.1 Linear Model.....	127
A1.2 Simple Second-order Model	133
A1.3 Simple Quadratic Model	135
A1.4 Quadratic Model of a D-optimal Design of RSM.....	137
A2 Conclusions	140
References.....	140
Appendix B	142
Investigating Thiol-Modification on Hyaluronan via Carbodiimide Chemistry using Response Surface Methodology.....	142
B1 Materials and Methods.....	143
B1.1 Materials	143
B1.2 Design of Experiments.....	144
B1.3 Amidation of HA	145
B1.4 Determination of degree of amidation via disulfide linkage.....	146
B1.5 Ellman's reaction	146
B1.6 Characterization of Amidated HA	147
B2 Results and Discussion.....	147
B2.1 Amidation and Characterization of HA	147
B2.2 Fractional factorial design.....	150
B2.3 D-optimal design of RSM.....	155
B2.4 Optimization of factors	159
B3 Conclusions	160
References.....	161
Curriculum Vitae	164

List of Figures

Figure 1.1:	Anatomy of the human eye. Vitreous is a transparent material that fills the posterior segment of the eye. (Figure reproduced from Bishop et al. [3])	1
Figure 1.2:	Schematic diagram of rigid-rod like collagen fibrils. The collagen molecules of types II, V/XI and IX may co-assemble into heterotypic collagen fibrils. (Scheme reproduced from Sebag et al. [4]).....	2
Figure 1.3:	Elastic modulus of vitreous determined by various investigators (Figure reproduced from Swindle et al. [25]).	5
Figure 1.4:	The anatomy of the vitreous as hypothesized by Nickerson et al. [27]	7
Figure 1.5:	Computational model of oxygen gradient in the posterior human eye. (Figure reproduced from Filas et al. [32]).....	8
Figure 1.6:	<i>In situ</i> -forming polyacrylamide based hydrogels with reversible thiol crosslinking system. The hydrogel with S-S linkages, developed through free radical polymerization of monomers, were reduced back to –SH groups. The reduced polymeric solution was injected into the vitreous cavity, which re-establishes the S-S linkages, forming a stable hydrogel. (Figure reproduced from Swindle et al. [55, 56].	13
Figure 2.1:	Reaction scheme for thiolation of gellan using carbodiimide chemistry.....	24
Figure 2.2:	Copolymerization of MAM, MAA, and BMAC. (Figure reproduced from Liang et al. [69])	26
Figure 2.3:	¹ HNMR spectra of poly(MAM-co-MAA-co-BMAC) in D ₂ O.....	27
Figure 2.4:	Schematic representation of our two-component polymer solution injected via syringe into the vitreous cavity. Thiolated gellan in the formulation undergoes phase-transition to form a physically cross-linked hydrogel instantaneously upon cooling. The thiols in the polymeric mixture oxidize to form mixed disulfide linkages and establish a chemically crosslinked network.	28
Figure 3.1:	Design points used in the D-optimal design of RSM. The variables – concentrations of thiolated gellan and poly(MAM-co-MAA-co-BMAC) – were varied between 0.5 – 1.5 and 5.0 – 15.0 mg/mL respectively. The points represent each hydrogel formulation, and the numbers represent the number of replicates at each point.	32
Figure 3.2:	Experimental set-up of the 1D-diffusion chamber. (A) Three-chamber diffusion cell. (B) Schematic diagram of overall set-up (not drawn to scale). In a three chamber diffusion cell set-up, the top-chamber is filled with a flow of aerated solvent (1X PBS) via the inlet and outlet at 10 mL/min. The mid-chamber is filled	

with the hydrogel sample/controls, and the bottom chamber remains empty. The top- and the mid-chambers are separated by a semi-permeable membrane with a MWCO of 3.5 kDa, whereas the bottom chamber is blocked by an aluminum sheet instead of a semi-permeable membrane. At 10 mm from the top of the mid-chamber, there is a 1mm hole, through which a 21G 1 ½" needle containing the oxygen measuring probe (OxyLab pO₂ E-Series Sensor) is inserted. The oxygen probe is connected to a computer interface that records the measured partial pressure data in real time. 37

Figure 3.3: Boundary conditions for oxygen transport through the hydrogels 40

Figure 3.4: Optical transmittance (%) of natural vitreous and two-component hydrogels for wavelength from 200 to 800 nm. The hydrogels are either of formulation 1.5 mg/mL of thiolated gellan and 10 mg/mL of copolymer (1.5G_10CoP), or 0.9 mg/mL of thiolated gellan and 12 mg/mL of copolymer (0.9G_12CoP). Error bars are the standard deviation of three replicates of each sample. 45

Figure 3.5: Temperature scans for a mixture of 0.9 mg/mL thiolated gellan and 12 mg/mL poly(MAM-co-MAA-co-BMAC). 47

Figure 3.6: A modelled cubic surface plot of sol-gel transition temperature against the concentration of thiolated gellan and copolymer in mg/mL.  represents increasing transition temperature from 35.5 to 43 °C. 48

Figure 3.7: Variation in transition temperature of two-component hydrogels made of 1.5 mg/mL gellan combined with increasing concentrations of copolymer, from 5 mg/mL (1.5G_5CoP) to 15 mg/mL (1.5G_15CoP). 49

Figure 3.8: Storage and loss moduli of a two-component hydrogel 0.9 mg/mL thiolated gellan and 12 mg/mL poly(MAM-co-MAA-co-BMAC). The storage moduli were greater than loss moduli at all frequencies from 0.01-10 Hz, indicating a gel-like behavior. 50

Figure 3.9: A modelled surface plot of storage modulus in Pa at 1 Hz against change in concentration of thiolated gellan and copolymer (CoP) in mg/mL. The storage moduli results from 17 two-component hydrogels were analyzed and fitted to the modelled surface with a p-value of <0.001 obtained from ANOVA.  represents the increasing storage modulus from 3 to 358 Pa. 51

Figure 3.10: Normalized degree of swelling (DoS) of the two-component hydrogel, 1.5G_15CoP, compared to that of each of its component, thiolated gellan (1.5G) and CoP (15CoP), in 1X PBS. 53

Figure 3.11: Surface model fit for normalized DoS of 17 hydrogels, designed using RSM, in 1X PBS for varying [G] and [CoP]. The color gradient represents increasing normalized DoS, from 1.2 to 1.7. The experimental results fit the modelled surface with a p-value of <0.001. 54

Figure 3.12:	Surface model fit for normalized DoS of 17 hydrogels in macroscopic polymer solution at 3 kPa osmotic pressure. The color gradient represents increasing normalized DoS, from 0.4 to 1.0.	55
Figure 3.13:	Swelling pressure produced by two optimized hydrogel formulations (n = 5 each) for varying ratios of injected polymer solution volume vs. volume of the native vitreous removed from the eye.	61
Figure 3.14:	Oxygen level in water at 23 °C (A, C), and at 38 °C (B, D) over time. (A, B) represent the partial pressure of oxygen measured over time. (C, D) represent the logarithmic conversion of dimensionless oxygen concentration over time. In all the plots, the experimental data is given in solid line (different colors represent the replicates), and the linear fit in C, D is represented in dashed line.	63
Figure 3.15:	Oxygen concentration of the experimental controls over time. The logarithmic form of dimensionless oxygen concentration decreases linearly over time. Solid lines indicate the experimental data (different colors represent the number of replicates), and dashed lines represent the fit.	65
Figure 3.16:	Logarithmic form of the dimensionless oxygen concentration of hydrogel samples over time. (A) 0.9G_12CoP hydrogel (B) 1.5G_10CoP hydrogel. Experimental data for different repeats are given in solid lines of different colors, and the linear curve fits are represented in dashed line.	66
Figure 3.17:	Oxygen diffusion coefficient in controls and hydrogels. All the other mediums are measured at 38 °C. Data represent Mean diffusivity, and error bars indicate the standard deviation. The significant difference between the values, with p<0.05 is represented as (*) and p<0.01 as (**).	67
Figure 4.1:	(A) Anatomy of the rabbit eye with the sites where the partial pressure of oxygen was measured. (B) Image of the oxygen measuring probe. The probe (extending from the white head) is very thin compared to the 25G needle represented in blue for reference.	80
Figure 4.2:	Path of current flow through monolayer of cells plated over gold electrode at different frequencies in ECIS. (Figure reproduced from Applied Biophysics)	83
Figure 4.3:	The measured resistance of (A) ppRPE and (B) rMC-1 cells seeded at different cell densities over time. The resistances were measured at 4000 Hz.	84
Figure 4.4:	The growth behavior of the retinal muler cells (rMC-1) after reaching confluency. (1) Bright-field images of cells at different time periods. (A) At confluence, (B) 2 days after confluency, and (C) 3 days after confluency. (2) Measured resistance at 4000 Hz over time corresponding to the time periods A, B, and C. Note that media was added/exchanged on days 2, 3, 4, and 5.	85

Figure 4.5:	Capacitance of the cells measured at 64,000 Hz as a function of time. (A) ppRPE cells (B) rMC-1 cells. The slope of the experimental data, are fitted with linear regression models.	86
Figure 4.6:	Doubling times of cells seeded at different cell densities (# of cells/well).	87
Figure 4.7:	The measured resistance of ARPE-19 and ppRPE cells in contact with three different thiolated gellan hydrogel formulations over time. Controls are cells without hydrogel. All measurements were at the 4000 Hz, the optimal frequency for measuring the biocompatibility of the cells in either high density (non-proliferative, A–C) or low density (proliferative, D–F) conditions. The resistance spikes on days 1, 4, and 7 represent the exchange of cell medium.	88
Figure 4.8:	The measured resistance of cells after addition of hydrogels of different formulations. Control is cells without hydrogel. All measurements were at the 4000 Hz, the optimal frequency for measuring the biocompatibility of the hydrogels in contact with a confluent layer of cells. (A) ARPE-19 cells, (B) ppRPE cells, (C) 3T3/NIH cells, and (D) rMC-1 cells. Note that the resistance measurements were represented from the time after the addition of polymer solution to the cells. Data represents the Mean (n=4) ± SE.	90
Figure 4.9:	Morphology of rMC-1 at different time periods. The hydrogels were added over a confluent layer of the RMCs and were found to be biocompatible without any drastic change in the morphology. The cell densities of rMC-1 increase with each day and curl up after 2 days of confluency due to excessive growth.	91
Figure 4.10:	The % biocompatibility of hydrogels from MTT, and Cell count analysis. The biocompatibility of the control (cells without the hydrogel) was fixed at 100%. Data represents the Mean (n=4) ± SE.	92
Figure 4.11:	Measured resistance of proliferating layer of cells in contact with three hydrogel formulations over time. Control is the cells without hydrogel. The resistances were measured at 4000 Hz frequency. Each data point in the hydrogels and control represents the average of 15 wells and 3 respectively. Data represents the Mean (n=4) ± SE.	93
Figure 4.12:	Bright-field images of (A) ARPE-19, (B) ppRPE, and (C) 3T3/NIH cells alone (control on 11th day) and in contact with composite hydrogel 0.9G_12CoP on the 4th, 7th and 11th day post polymer addition (Scale bar – 100 um).	95
Figure 4.13:	Barrier resistance measurements in Ohm.cm ² over time (days) for ppRPE cells plated at high density (40,000 cells/well) for three different formulations of hydrogel. The spikes in resistances denote medium exchanges. Data represents the Mean (n=4) ± SE.	96
Figure 4.14:	Degradation studies. (A) Percent of mass remaining in the 0.9G_12CoP and 1.5G_10CoP hydrogels after 4 weeks in the presence of lysozyme and trypsin. (B) Storage moduli of 1.5G_10CoP and 0.9G_12CoP at different frequencies. Control	

is the hydrogel in 1X PBS. Error bars are the standard deviations from three replicates of each sample..... 97

Figure 4.15: Degradation study on the hydrogel. Confocal images of the ppRPE cells. The image shows the monolayer of cells stained for nuclei (blue; DAPI) and cell matrix – actin fibers (red; phalloidin) in (i) Control medium (without hydrogel contact) and in contact with (ii) 1.5G_10CoP hydrogel and (iii) 0.9G_12CoP hydrogel. No toxic effect was observed. 98

Figure 4.16: (A) Fundoscopic and (B) OCT images of rabbit vitreous cavities and retinas. (1) Non-surgical control (2) Silicone oil vitreous replacement (3) 0.9G_12CoP replacement, and (4) 1.5G_10CoP hydrogel replacement. No vitreous opacity, vitreous hemorrhage, membrane formation, chorio-retinal lesions, or atrophy in retinal layers is observed. 100

Figure 4.17: Pre-surgical and post-surgical IOP measurements in all experimental groups. Data represents the mean \pm SE. At 30 days post-operation, no significant difference was observed in IOPs of the hydrogel-treated rabbits (n=10 for 0.9G_12CoP and n=8 for 1.5G_10CoP gel) compared to the controls (n=10 for silicone oil and n=24 for non-surgical control). 101

Figure 4.18: ERG response (n=5) of a rabbit retina elicited by light stimuli under mesopic conditions (moderate light conditions where both rods and cones are active). The ERG responses were obtained before and 30 days post-operation, where rabbit vitreous was partially replaced with a 0.9G_12CoP hydrogel. Data represent the mean amplitudes (n=5) \pm SE. 102

Figure 4.19: The characteristic ratios of post- to pre-operative a-wave and b-wave amplitudes (A, C, D), and corresponding implicit times (B) of the vitreous-substitute- treated (right, R) eye and the control (left, L) eye, when stimulated with standard mesopic (2.526 cd·s·m⁻²) light (A, B), scotopic light in dark adapted conditions (C), and photopic flash in light adapted conditions (D). (A) compares the amplitude between substitutes, and (B) compares the implicit times between substitutes. The photoreceptor activity was normal and functional with the hydrogels. 104

Figure 4.20: Bright-field microscopic image (H&E staining, Scale bar = 50 μ m) of rabbit retinas. (A) Non-surgical control. (B) Silicone oil, (C) 0.9G_12CoP hydrogel, and (D) 1.5G_10CoP hydrogel. B, C, and D are retinas of rabbit eyes with partial vitreous replacements. All retinal layers were intact, without any retinal atrophy. 105

Figure 4.21: Histopathology scores for rabbit retinas with silicone oil (n=9), 0.9G_12CoP (n=8), and 1.5G_10CoP (n=8) hydrogel as vitreous replacements. Scores from 0 to 4 indicate severity, from null to severe. Data represent the mean \pm SE. No significant difference was observed between the hydrogels and the controls, with the exception for the mononuclear cell inflammation, which was common, but minimal (score~1)..... 106

Figure 4.22: Oxygen tension (partial pressure of oxygen (pO_2) in mm Hg) values for different substitutes measured 30 days post-surgery. Data represents the Mean \pm SE. The number of repeats (animals) was 8, 3, and 9 for the left eye, silicone oil and the 1.5G_10CoP hydrogel respectively. At the vitrectomy site, there is a significant increase in pO_2 values for silicone oil compared to the left eye control and the 1.5G_10CoP hydrogel. A significant increase in pO_2 was also observed between the vitrectomy and the intra-vitreous site for rabbits replaced with silicone oil..... 108

Figure A1: Design space for a linear model of an RSM. Squares represent the formulation, and the number represents the number of repeats at each formulation..... 128

Figure A2: A modeled planar surface plot of sol-gel transition temperature against the concentration of thiolated gellan [G] and copolymer [CoP] in mg/mL.  represents increasing transition temperature from 35.5 to 43 °C..... 131

Figure A3: Design space for a simplest second-order model of an RSM. Squares represent the formulation, and the number represents the number of repeats at each formulation. 134

Figure A4: A modeled planar surface plot of sol-gel transition temperature against the concentration of thiolated gellan [G] and copolymer [CoP] in mg/mL.  represents increasing transition temperature from 35.5 to 43 °C..... 135

Figure A5: Design space for a simple quadratic model of an RSM. Squares represent the formulation, and the number represents the number of repeats at each formulation. 136

Figure A6: A modeled quadratic surface plot of sol-gel transition temperature against the concentration of thiolated gellan [G] and copolymer [CoP] in mg/mL.  represents increasing transition temperature from 35.5 to 43 °C..... 137

Figure A7: Design space for a quadratic model of a D-optimal RSM design. Squares represent the formulation, and the number represents the number of repeats at each formulation. 138

Figure A8: A modeled cubic surface plot of sol-gel transition temperature against the concentration of thiolated gellan and copolymer in mg/mL.  represents increasing transition temperature from 35.5 to 43 °C..... 139

Figure B1: Carbodiimide crosslinking reaction of HA and Cys with EDC and NHS 147

Figure B2: Normal probability plot of the effects of the factors and their interactions. Effect of single factors is represented by A, B, C, D, E; their interactions with other variables are represented as AB, BC, etc. In this figure, A- Cys; B- pH; D- EDC; BD- two factorial interaction of pH and EDC.  represents positive effects; while  represents negative effects. The model is framed based on selecting the dominant factors that are highlighted, and labeled in plots; other factors are considered as errors..... 150

Figure B3:	(a) Pareto chart representing the effect of each factor over response variable in the descending order from greatest to lowest contribution for FF design. Bonferroni limit is the threshold where the effect emerging above this limit are significant. T limit is the threshold where the effect emerging above this but below Bonferroni limit may possibly be significant. Effects D, B, BD, A are significant. b) Box-Cox plot of power transforms representing the required transformation of data for FF design. In this figure, blue line represents lambda current = 0; green line is best lambda current = -0.13. The recommended transform is Log transformation with lambda = 0.	151
Figure B4:	Residual analysis of the FF design. (a) Plot of normal probability of residuals and (b) Plot of external studentised residuals with each run.	153
Figure B5:	Model graph depicting the nature of interactions between the factors EDC and the pH of the reaction medium in response to amidation at constant values of other factors of Cys = 10 (moles), NHS = 0.1 (moles), time = 3.5 h for FF design. Note that thiol content is a surrogate for amide content.	154
Figure B6:	Model graph depicting the nature of interaction between factors EDC and Cys in response to thiol derivatization at constant values of other factors of pH = 6.5, NHS = 0.5 (moles), and time = 3.5 h D-optimal design of RSM.	157
Figure B7:	A characteristic ^1H NMR spectrum of amidated HA with side product.	158
Figure B8:	Model graph depicting the nature of interaction between factors EDC and Cys in response to the side reaction.	159

List of Tables

Table 3.1:	Sol-gel transition temperature, storage and loss moduli, and percentage swelling for 17 hydrogels designed using RSM.....	46
Table 3.2:	Rheological and physical properties of three RSM optimized formulations of the two-component hydrogel.....	60
Table 4.1:	Amplitudes and implicit times of characteristic waves in response to standard mesopic, scotopic, and photopic light stimuli.	103
Table A1:	The factors and response for a linear model of RSM.	128
Table A2:	ANOVA for a linear model based on coded factors.	132
Table B1:	Alias structure of the 2(5-1) fractional-factorial design	144
Table B2:	The experimental condition (factors) and thiol content (response) obtained from a disulfide test for each experiment using FF design.....	148
Table B3:	Table representing the experimental conditions (factors) and thiol content (response) obtained from disulfide tests for each experiment using response-surface design	152
Table B4:	Model Summary Statistics of the FF and RSM Models	153

Acknowledgments

I am grateful to my adviser, Prof. Nathan Ravi, for his valuable mentorship, encouragement, support, genuine care and concern. Many thanks to my colleagues and collaborators who made this endeavor pleasant and stimulating: Dr. Jue Liang, Dr. Josh Davis, Dr. Ying-Bo Shui, Dr. Rinku Baid, and Ms. Jessica Struckhoff. Special thanks to Mr. Paul Hamilton and Ms. Bedia Begum Karakocak for being my pillar of strengths throughout this journey. I would like to thank my committee members, Prof. Palghat Ramachandran, Prof. Daniel Giammar, Prof. Srikanth Singamaneni, Prof. Marcus Foston and Dr. Rithwick Rajagopal for helpful discussions. Heartfelt thanks to Prof. James Ballard for reviewing and providing constructive comments to improve my dissertation. Special mention goes to my friend, Dr. Anchal Ghai, for her valuable support, care and encouragement. I am indebted to my family for their boundless love, care, support, and for believing in me.

This work was supported in part by the NIH grant, EY021620, the Department of Veterans Affairs rehab merit review grant, RX000657-01, Research to Prevent Blindness, Inc., and NIH Core Grant P30 EY02687. I am thankful to the Department of Energy, Environmental, and Chemical Engineering for their funding, and the Department of Ophthalmology and Visual Sciences for their core facilities to pursue this work.

Sruthi Santhanam

Washington University in St. Louis

December 2017

Dedicated to my family.

ABSTRACT OF THE DISSERTATION

Two-Component Hydrogel as Biomimetic Vitreous Substitutes

by

Sruthi Santhanam

Doctor of Philosophy in Energy, Environmental, and Chemical Engineering

Washington University in St. Louis, 2017

Professor Nathan Ravi, Chair

The vitreous humor of the eye is a biological hydrogel principally composed of fibrillary collagen interspersed with semi-flexible polyelectrolyte, hyaluronic acid (HA). Certain pathological conditions necessitate its removal and replacement. Current vitreous substitutes, such as silicone oils and perfluorocarbons, are hydrophobic, do not resemble the properties of the vitreous, and have known complications. An ideal vitreous substitute should have properties of the natural vitreous, perform its functions, and be biocompatible in the eye. Inspired by the structure and composition of the natural vitreous, we used bio-mimicry to develop an injectable two-component hydrogel. The hydrogel is composed of a fibrillary gellan, an analogue of collagen, and a semi-flexible polyelectrolyte poly[methacrylamide-co-(methacrylic acid)], an analogue of hyaluronic acid, both endowed with thiol cross-linkers for reversible covalent linkage. The gellan, in the polymeric mixture, undergoes coil-helix transition near physiological temperature, enabling instantaneous *in situ* physical gelation of the solution. The thiol cross-linkers that later oxidize to disulfides under physiological conditions, make the hydrogel non-absorbable, non-degradable, and reversible, for facile removal if needed.

We used response surface methodology to investigate the structure-property relationships of eleven two-component hydrogels, and identified two hydrogel formulations that match the

primary properties of the vitreous. We determined how each component of the hydrogel affects their optical, mechanical, sol-gel transition temperature, and osmotic swelling properties. All the hydrogels were transparent to visible light, with density and refractive indexes nearly equivalent to those of the natural vitreous. The shear storage moduli of the hydrogels, at 1Hz, ranged from 3 to 358 Pa, and the sol-gel transition temperatures, from 35.5 to 43 °C. In addition, as expected, all the hydrogels swelled in physiological solutions. Interestingly, we discovered that the relatively large swelling capacity of the semi-flexible ionic copolymer was significantly restricted by the minimally swellable fibrillary gellan network. The tightly swollen gel of two dissimilar networks produced Donnan osmotic swelling pressure in physiological solutions, which is also the driving force for re-attachment of the retina. Insights from the biomimetic nature of the gel, led us to propose that the natural vitreous also exhibits controlled swelling, where ionic HA's swelling capacity is restricted by fibrillary collagen. The Donnan swelling pressure produced by the tightly swollen vitreous gel maintains the delicate internal structure of the eye, and perhaps plays a critical role during the ocular development.

We evaluated the biocompatibility of the two optimized formulations of the hydrogels on different cell lines, and in rabbits. Both hydrogels were found to be biocompatible on primary porcine retinal pigment epithelial cells, human retinal pigment epithelial cells, and fibroblast (3T3/NIH) cells, by electric cell-substrate impedance sensing system. Furthermore, the hydrogels did not impair tight junction formation or affect proliferation of the cells. The hydrogels were also non-degradable in enzymatic solutions and in contact with ocular cell line for four weeks. Judged against silicone oil, a clinically-accepted vitreous replacement, both hydrogel formulations were biocompatible in rabbits for 30 days. Both hydrogels maintained optical clarity, physiological intra-ocular pressure, and intact retinal layers that displayed normal

electroretinographs. In two cases of the iatrogenic retinal tear, the hydrogels reattached the retina by producing osmotic swelling pressure. The hydrogels also maintained the low oxygen environment, compared to silicone oil, in the rabbit's vitreous cavity for 30 days post-surgery.

In conclusion, the two hydrogels reattach the retina via a unique mechanism of osmotic swelling pressure. They overcome the limitations of silicone oil with comparable *in-vivo* biocompatibility, and merit further evaluations as an artificial vitreous. In addition, the ability to control the mechanical and swelling properties of the two-component hydrogels over a wide range suggests their utility as biomimetic replacements of other soft tissues, such as cornea, nucleus pulposus, and cartilage.

Chapter 1: Introduction

1.1 Vitreous humor

1.1.1 Structural Macromolecules and their Bio-Synthesis

Vitreous humor is a clear, jelly-like structure in the posterior segment of the eye that occupies two-thirds of the human eye (by volume) [1]. It is firmly attached to the surrounding tissues at the pars plana of the ciliary body and at the peripheral retina, the vitreous base, the macula, and the optic nerve disc. It is transparent to visual light, has a refractive index (RI) between 1.3345-1.3348, and a density between 1.0053-1.0089. It allows circulation of metabolic solutes and nutrients throughout the eye. It is a virtually acellular, highly hydrated extracellular gel matrix primarily composed of water, both bound and free water, with less than 1% (w) of collagen fibrils and polymer chains of glycosaminoglycan (GAG) – hyaluronic acid (HA). Other vitreal proteins include fibrillin, chondroitin sulfate, versican, tenascin, and serum proteins, such as albumin, fibronectin and transferrin [2, 3].

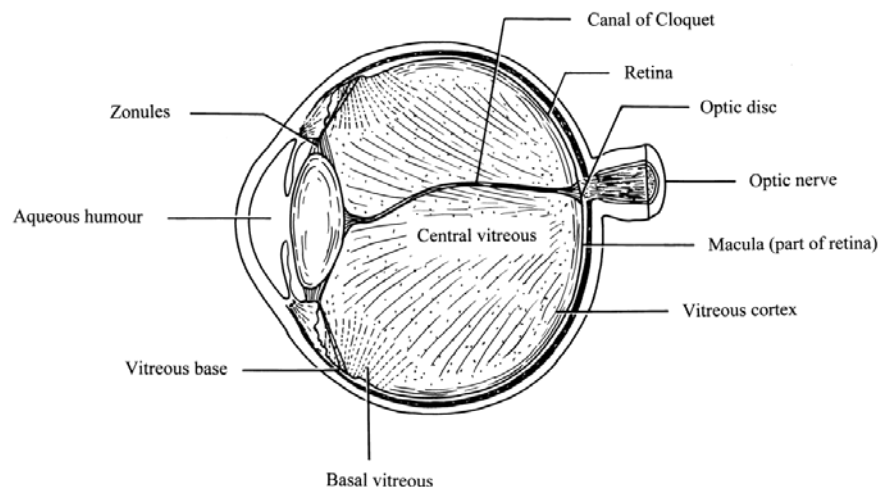


Figure 1.1: Anatomy of the human eye. Vitreous is a transparent material that fills the posterior segment of the eye. (Figure reproduced from Bishop et al. [3])

Collagen is the major structural protein essential for the shape, strength, and resistance to the swelling forces induced by the HA polymeric chains. Collagen fibrils are heterotypic in nature and are made of types II, V/XI, and IX (Figure 1.2).

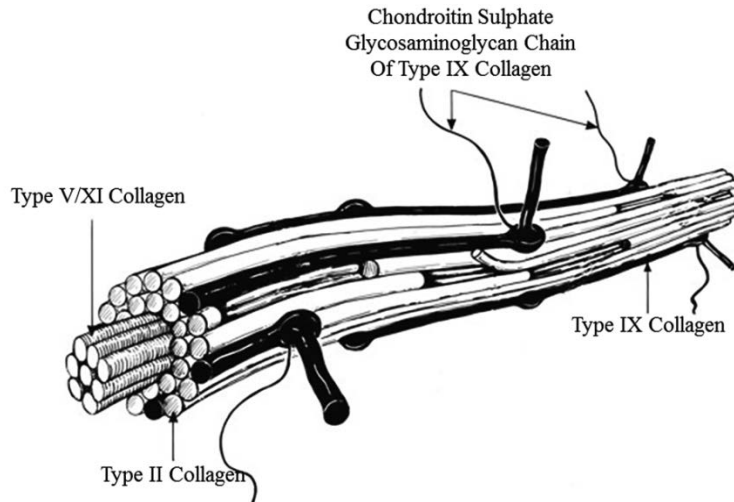


Figure 1.2: Schematic diagram of rigid-rod like collagen fibrils. The collagen molecules of types II, V/XI and IX may co-assemble into heterotypic collagen fibrils. (Scheme reproduced from Sebag et al. [4])

Type II is the predominant collagen type in the vitreous humor, constituting about 75% of the total collagen [5]. It is a member of the fibril-forming group of collagens, where type-II molecules form a triple helix structure with other collagen types. They are synthesized in the ciliary body. Type V/XI collagen constitute $\approx 10\%$ of the collagen in the vitreous, with roles in nucleating collagen fibril formation and regulating collagen fibril diameter [6]. Type IX collagen is not a fibril-forming collagen; however is found on the surface of collagen fibrils. They bind with the chondroitin sulfate and are considered as proteoglycan molecules [5]. Type IX collagen molecules predominantly originate from the non-pigment ciliary epithelium of the ciliary body. The total collagen concentration in the vitreous gel is estimated to be $\approx 286 \mu\text{g/mL}$ [1]. They are not uniformly distributed throughout the vitreous gel; highest concentration is near vitreous base and vitreous cortex, and lowest near central vitreous. Halfter et al. [2] showed that the rate of synthesis of structural vitreal proteins, such as collagen II and IV and laminin, in

humans and chick were abundant during embryogenesis and becomes barely detectable upon reaching adulthood. The down-regulation of vitreal protein synthesis occurs during early postnatal life, and is from then-on maintained throughout life with minimum turnover.

The proteoglycans (PG) are glycosylated proteins covalently bonded to the negatively charged glycosaminoglycan (GAG), a long un-branched highly polar polysaccharides that are water attracting and flexible around their ether bonds. Hyaluronic acid is the major GAG in the vitreous, critical for providing swelling pressure that inflates the gel and spaces the structural proteins [7]. They are non-sulfated and are synthesized on the cytoplasmic surface of the plasma membrane. The concentration of HA in the adult human vitreous is between $\approx 240 \mu\text{g/mL}$ and constitutes nearly 90% of the uronic acid-containing macromolecules in the eye [1, 8]. Major proportion occurs as high molecular weight polymer chains with molecular weight greater than 1000 kDa (average 2-4 million), and possesses viscoelastic properties [8]. The electrostatic interactions between the ionic side groups of the HA chains and the small mobile ions in the tissues, contribute significantly to the structural and functional organization of the vitreous. Similar to the collagen fibrils, HA are also non-uniformly distributed with highest concentration near the posterior vitreous cortex. Other PG of the vitreous includes chondroitin sulfate, versican, and collagen IX. The collagen IX and chondroitin sulfate molecules are thought to play a central role in maintaining the spacing between the collagen fibrils.

1.1.2 Functions and Properties

The complementary properties of the composite networks of the vitreous – rigid scaffolds of collagen and semi-flexible polyelectrolyte HA – are thought to play a central role in various functions of the vitreous. Important functions include maintaining optical transparency [9], acting as a viscoelastic damper that protects surrounding ocular tissues from sudden mechanical

impact [10, 11], supporting the growth of the eye [12], and mediating nutrient and oxygen transport [13-15]. In the vitreous, the specific organization of the bio-polymers (Collagen and HA) acts as a molecular sieve and limits the space for large molecules. Also, the exclusion of proteins and cells helps in maintaining transparency [1, 3].

The interaction between collagen and HA in the vitreous makes it a visco-elastic hydrogel [10] that acts as a shock absorber and dampens the intra-ocular motions and vibrations. Rheological characterizations on the vitreous revealed that the vitreous behaves as a viscoelastic solid under physiological frequencies. At these frequencies, the storage modulus (elastic component, G') is greater than the loss modulus (viscous component, G''). Various research groups have investigated the mechanical properties of vitreous in different species of organisms, such as porcine, bovine, and human vitreous. Different rheological methods have been employed to measure the visco-elastic properties of native vitreous. The different techniques include inserting compression chucks with dynamic viscoelastometer into the vitreous cavity[16], light scattering [17], torsional pendulum [18], magnetic microrheometer [10, 19, 20], shear rheometry [21, 22], capillary rheometry [23], and cavitation rheometry [24]. The elastic shear modulus of the vitreous measured using these techniques have been summarized by Swindle et al [25] as shown in the Figure 1.3.

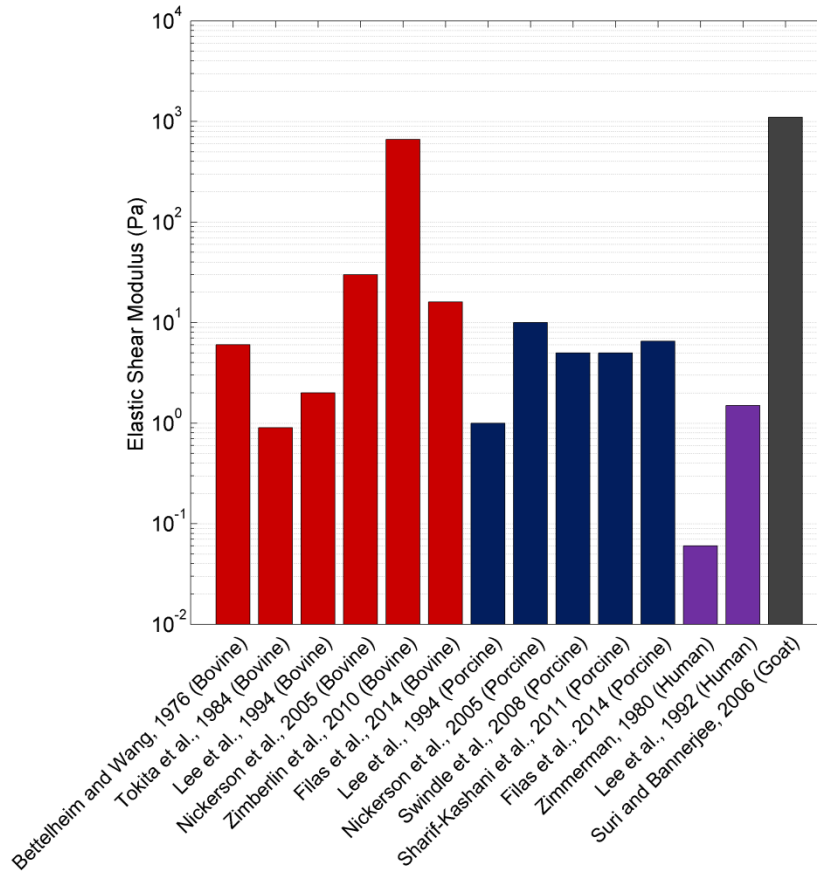


Figure 1.3: Elastic modulus of vitreous determined by various investigators (Figure reproduced from Swindle et al. [25]).

A few important conclusions that I would like to emphasize from these studies are the following: First, vitreous is a heterogeneous visco-elastic gel with collagen fibrils contributing to the elasticity, and HA to that of the viscosity of the material [16, 26]. Second, the combination of collagen and hyaluronic acid in the vitreous creates an interpenetrating mesh, which gets destroyed upon removal from the eye. This consequently results in a noticeable decrease in modulus of the vitreous over time outside the eye. Hence, the vitreous moduli are even higher when measured *in vivo* than the *ex vivo* [21, 22]. For instance, the storage modulus of the porcine vitreous is 10 ± 1.9 Pa and loss modulus is 3.9 ± 0.8 Pa, when measured outside the vitreous cavity. Similarly, G' is 32 ± 12 Pa and G'' is 7 ± 2 Pa when measured outside the

bovine vitreous cavity. Zimmerlin et al. [24] measured the storage modulus of bovine vitreous, via cavitation rheometry, *in vivo*, without disturbing the architecture of the vitreous. They found the G' to be approximately 120 Pa, which was way higher than those measured outside the cavity. The change in architecture of the vitreous when removed from its cavity suggests expecting a higher value *in vivo*. Finally, of the various animals, the mechanical properties of the human vitreous are similar to those of the porcine vitreous. Furthermore, the human vitreous most closely resembles that of the central region of the porcine vitreous, indicating that the porcine vitreous would serve as a suitable animal model for the human vitreous humor [10, 19, 20].

Another important, yet little-studied, is the role of the vitreous in generating osmotic swelling pressure. Experimental techniques to predict the swelling pressure lack due to the fragile biopolymer network of the native vitreous. Nickerson et al. [27] measured the rheological properties and the mass of porcine vitreous and noticed that both reduced with time when removed from the eye. Consequently, they hypothesized collagen as a stretched web of ropes that resists undulating due to loss of entropy. The HA was trapped between the web of collagen fibrils and the hydrostatic force exerted by the swelling HA approaches equilibrium against the tension from the collagen fibrils (Figure 1.4). This swelling induces an internal tension in the vitreous. Upon removal from the eye, the entropically favored reduction in collagen fibril's end-to-end length drives the HA out of network.



Figure 1.4: The anatomy of the vitreous as hypothesized by Nickerson et al. [27]

Halfter et al. [28] disrupted the vitreous body and the inner limiting membrane of chick embryos with collagenase, and observed an enlargement (predominantly axial) in the eye size. They also speculated that during scleral development, the cortical vitreous body and the inner limiting membrane of the retina, which are rich in collagen, provided the mechanical strength to withstand the pressure emanating from the core or the central vitreous that is relatively rich in hyaluronic acid. The ionic HA forms a highly swellable network that may have increased the weight of the vitreous body, and have caused the expansion of the eye orbit. From both these studies, it is conclusive that the vitreous may be capable of generating an osmotic swelling pressure, which may support the retina in its position and serve as a mechanical stimulus for growth of the eye during development.

The vitreous gel, by virtue of its large size and central location within the eye, is also assumed to be important in regulating intraocular oxygen tension. Distribution of oxygen is critical in the pathogenesis of various ocular diseases [29]. For instance, retinal hypoxia may contribute to diabetic retinopathy and other retinal ischemic diseases [30], while increased

exposure of oxygen near lens may contribute to nuclear sclerotic cataract [31]. Vitreous maintains an oxygen gradient to prevent the occurrence of above mentioned ocular diseases.

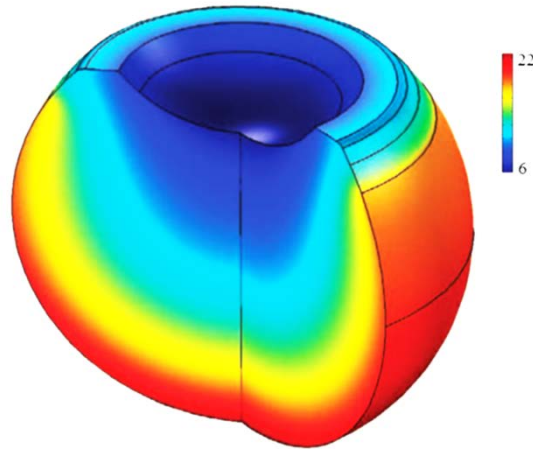


Figure 1.5: Computational model of oxygen gradient in the posterior human eye. (Figure reproduced from Filas et al. [32])

Shui et al. [33] determined that the oxygen level in the rabbit vitreous decreases from the posterior side of vitreous near retina (31 mm Hg in the eyes of rabbit breathing 20% oxygen at respiration rate) towards the anterior side of vitreous near lens (6 mm Hg) (Figure 1.5). In a healthy normal eye, the core of vitreous is under hypoxic conditions where the intra-ocular oxygen tension is 7.1 ± 0.5 mmHg [31]. The oxygen from the retinal vessels is consumed by the retinal epithelial cells and retinal cell layers. The vitreous gel is critical in preventing the diffusion of oxygen towards lens. Recent investigations on the oxygen tension, and the role of vitreous gel in metabolizing oxygen through an ascorbate-dependent manner, led to a new understanding of the vitreous gel [13, 34]. Filas et al. [32] determined that the vitreous gel possesses high concentration of ascorbate of approximately 2mM. A consecutive series of undiluted human vitreous gel samples from 62 eyes were measured for oxygen consumption with a micro-respirometer. They observed that ascorbate in pure water does not consume oxygen; however, ascorbate in the vitreous has the ability to consume oxygen. The molecular oxygen in

the vitreous reacts with ascorbate in the presence of an unknown catalyst found exclusively in the vitreous gel to form dehydroascorbate, water and half the initial amount of oxygen. Through this mechanism, the ascorbate level is depleted, and the oxygen is consumed, thereby maintaining the oxygen gradient. Although the mechanism is interesting, there are several observations that are not explained by the above mechanism. For example, how ascorbate is being replenished in the vitreous cavity, and the role of hyalocytes in oxygen consumption within the vitreous cavity, before and post-vitreectomy, is not yet elucidated. Additionally, when guinea pig lenses are placed in hyperbaric oxygen, they begin to form nuclear cataracts only when the glutathione levels are markedly decreased in the lens and not on the level of oxygen. Thus, it appears that the complications may be due to imbalances in redox buffer capacity that is ostensibly associated to only oxygen. Clearly further research is indicated to resolve the pathophysiology of post-vitreectomy ocular complications.

1.1.3 Pathology and Pathophysiology

The functions and properties of the vitreous are perturbed, because of aging, and pathological process, resulting in various vision-threatening ocular conditions. The changes in the vitreous network structure, composition, and the interaction between its structural macromolecules are presumed to cause the perturbation in its functions and properties. With aging (after 40 years), the gel volume of the vitreous drastically decreases with a concomitant increase in the liquid volume, resulting in an ocular disease called vitreous liquefaction [12]. Liquefaction causes derangement of the normal association between collagen and HA that results in aggregation of collagen fibrils into bundles of parallel fibrils known as 'floaters', and formation of pockets of liquid vitreous called 'lacunae'. Liquefaction of gel structure can cause degeneration or detachment of the vitreous and is associated with a number of vision-threatening

phenomena such as vitreous hemorrhage, macular hole, and detached retina. Also with vitreous liquefaction, the oxygen from the retinal vessels can be carried away from the retina and distributed throughout the eyes with eye movements, thereby causing nuclear cataract in lenses that have redox levels below threshold [35].

1.2 Vitrectomy and Vitreous Substitutes

In the past four decades, vitrectomy, the removal of vitreous humor of the eye, has become an important treatment option for various ocular diseases, such as diabetic vitreous hemorrhage, retinal tear and detachment, uveitis, and ocular trauma involving the vitreous [36]. Vitreous replacements are an essential component of all vitrectomy surgery. Air, balanced salt solutions, perfluorocarbons (PFC), expansile gases, and silicone oils are used as replacements for the vitreous based on the clinical need [37, 38]. Expansile PFC gases are used as short-term substitutes for post-operative endo-tamponade and PFC liquids as intra-surgery tool to temporarily flatten the retina, which are exchanged for long-term substitutes. Silicone oil is clinically accepted for short- or long-term tamponade (pushing force against retina) to treat complex or refractory retinal detachments. Generally, the substitutes perform well; however, the current vitreous substitutes have several shortcomings, and cause significant patient burden. For instance, when gases are used to seal retinal breaks, the patient is often positioned face down for days or weeks to keep the injected gas bubble against any retinal break. Other limitations include expansion of gases at high altitudes, the toxic nature of PFCs over an extended period, elevated intraocular pressure, and lipophilic nature, emulsification and post-vitrectomic complications, particularly with the use of silicone oils [39-41]. Silicone oils, although clinically accepted as a long term substitute, are hydrophobic and have poor contact with fluids. They

have a high refractive index, inhibit total filling of the cavity and must be surgically removed at a later date due to the risk of developing cataracts, glaucoma, band keratopathy and corneal decompensation [41]. In addition, current vitreous substitutes that work by surface tension and pneumatic pressure provide no insight into the physiology of the vitreous. Hence, there is a need for long-term vitreous substitute that has fewer complications and is more similar to the native vitreous. Our approach is to develop an *in situ*-forming hydrogel substitute that is developed from the first principles of structure and function of the vitreous. In doing so, it enables us to gain more insight into the structure and physiology of the native vitreous. Furthermore, such a biomimetic gel will expand our knowledge and provide insights on the role of the vitreous structure and its relation to its properties.

1.2.1 Polymeric Hydrogels as Potential Vitreous Substitutes

Ideal vitreous substitutes are easily implantable materials that mimic the structure and functions of the native vitreous, and are biocompatible with the surrounding tissues. Active research is now focused on developing vitreous substitutes using natural and synthetic water-swelling polymers [42-47] that mimics the physical and mechanical properties of native vitreous. Various polymers have been proposed as vitreous substitutes, including collagen [48], hyaluronic acid [49, 50]; poly (1-vinyl-2-pyrrolidinone) (PVP) [51], polyvinylalcohol (PVA) [52, 53], and polyacrylamide (PAM) [54-56]. Bairo [57], Kleinberg et al. [58], and Su et al. [59] have extensively reviewed the use of hydrogels, cross-linked water-soluble polymers, as promising vitreous substitutes.

In the past, progress in the use of the hydrogels has been stymied by shear-degrading of the pre-formed gels during injection [48, 60]. To overcome the problem, *in situ*-forming/injectable hydrogels have been successfully developed [45, 46, 61-64]. An *in situ*-

forming hydrogel has several substantial benefits, other than the physical and optical properties similar to the native vitreous. It can be easily injected into the vitreous cavity as a solution without any modification of the current vitrectomy procedure. It does not shear degrade during the injection, a process which can cause fragmentation of the pre-formed gel and introduces free radicals into the cavity. The mechanical properties and the network architecture of *in situ*-forming gels are unformed prior to injection and therefore remain consistent. The *in situ*-forming gels could also serve as depots for intra-vitreous drug delivery [65].

Various investigators have explored injectable hydrogels as vitreous substitutes. For example, Magnani et al. [52, 53] investigated the applicability of poly(vinyl alcohol) (PVA) hydrogels with a trisodiumtrimetaphosphate (STMP) cross-linker as vitreous replacements. They demonstrated that the hydrogel exhibited thixotropic behavior and was injectable. The rheological analysis revealed that one of the hydrogels (PVA:STMP 8:1) behave similar to that of the human vitreous. Though their light transmittance, water content measurements, diffusion coefficient, and *in vitro* cytotoxicity confirm the applicability of the hydrogel as vitreous substitute, further studies are needed to measure their retention time, *in vivo* mechanical properties, *in vivo* cytotoxicity, and their ability to reattach the retina.

Annaka [66] has developed an *in situ*-forming vitreous substitute hydrogel based on poly(ethylene glycol) (PEG) end-capped with an octadecyl groups (E10KDC18). In this hydrogel, flower micelles act as junctions that provide the elastic modulus. The hydrogel was tested in rabbits, and was found to be non-toxic by monitoring postoperative intraocular pressure (IOP) and by histopathologic examination of retinal layers. The moduli for the E10KDC18 hydrogel were approximately three orders magnitude higher than the porcine modulus values, and refractive index values were also higher than that of the native vitreous. Although the

material has the potential to match the rigidity of the vitreous by varying the concentration of the octadecyl groups and/or the molecular weight of PEG, further experiments are needed to confirm their applicability.

Barth et al. [67] investigated the use of a crosslinked sodium hyaluronic acid (HealafloTM) as a vitreous substitute. The hydrogel was optically clear, maintained its viscosity and were biocompatible in rabbit eyes, without affecting the retinal morphology or functionality. Although they look promising, the hydrogels slightly raised the intra-ocular pressure and had a short-residence time *in vivo*, restricting its long-term usage.

Hayashi et al. [68] synthesized a hydrogel with polymeric clusters of thiol and maleimide reactive tetra-armed poly(ethylene glycol). Formulations of this hydrogel with low (7.0 mg/mL) polymer concentrations gelled *in situ* within 10.0 minutes. They were found to be biocompatible in rabbit eyes and to produce low swelling pressure for retinal tamponade.

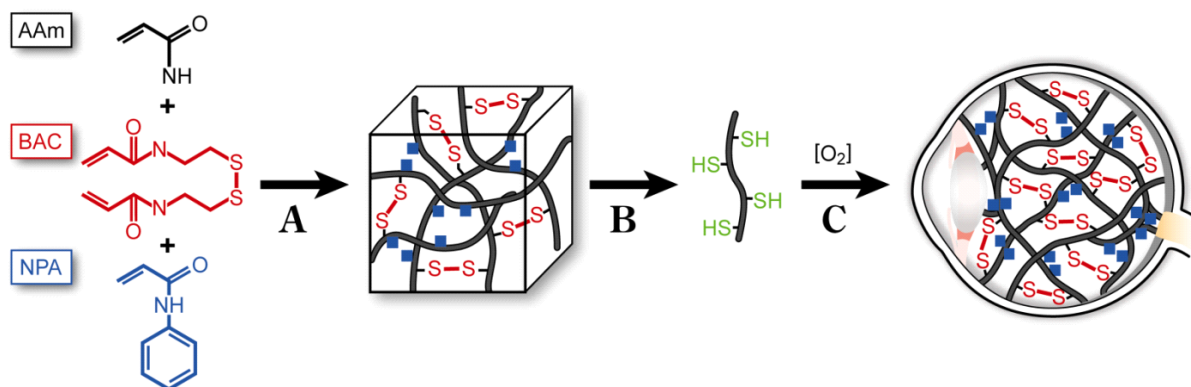


Figure 1.6: *In situ*-forming polyacrylamide based hydrogels with reversible thiol crosslinking system. The hydrogel with S-S linkages, developed through free radical polymerization of monomers, were reduced back to -SH groups. The reduced polymeric solution was injected into the vitreous cavity, which re-establishes the S-S linkages, forming a stable hydrogel. (Figure reproduced from Swindle et al. [55, 56].

Our laboratory has previously developed an *in situ*-forming polyacrylamide hydrogel using reversible disulfide cross-linker [55, 56]. The disulfide bond established between polymer chains can be reduced to thiol groups by dithiotheritol (DTT) (Figure 1.6). The reduced

polymeric solution re-gels to form a hydrogel upon consumption of oxygen in the vitreous cavity. The formation of disulfide cross-links establishes a stable hydrogel network that does not degrade easily and holds potential as a long-term vitreous substitute. Additionally, the reversibility potentially eliminates the need for a second vitrectomy in case the hydrogel needs to be removed. However, the polyacrylamide takes days to gel and becomes cloudy with time. To overcome these issues, our lab investigated and found the derivatives of polymethacrylamide that remains clear for months. Liang et al. [69], then synthesized the injectable hydrogel composed of copolymers of poly[methacrylamide-co-(methacrylic acid)] with thiol cross-linkers. The hydrogels were optically clear and transparent, with densities, refractive indexes and rheology similar to the vitreous, and were noted to be biocompatible *in vitro*. However, the hydrogels had long (3 days) duration of gelation.

Although polymeric hydrogels seem to be promising materials for long-term vitreous replacement, none have advanced sufficiently to reach clinical application. This is mainly because of their long-term toxicity, short residence time, degradation, or fragmentation – changes in viscoelastic properties and resiliency after injection through a small-gauge needle.

As an alternative to polymeric hydrogels, Gao et al. [70, 71] developed a novel artificial foldable capsular vitreous body (FCVB) to replace the native vitreous. The capsular material is made of silicone rubber, which is filled the capsule with different materials, such as saline or silicone oil [72], PVA hydrogel [73], and PEG sol [74]. The FCVB had optical, mechanical, and biocompatible properties similar to that of the native vitreous. This material is also undergoing clinical trials for its use as vitreous substitute. Although FCVB meets major functions of the native vitreous, it is not physiological and does not maintain the oxygen gradient within the vitreous cavity.

In summary, polymeric hydrogels and foldable capsular vitreous body achieved varying degrees of vitreous biomimicry. However, they do not meet all the essential functions of the native vitreous. Furthermore, the hydrogels provided only an incomplete understanding of the macromolecular structure and functions of the native vitreous, because they were all single component hydrogels that were analogous to the HA of the native vitreous, and lacked a fibrillary component analogous to the collagen fibrils. These observations prompted the investigation that is the subject of this dissertation. In the following section, I outline the research objectives.

1.3 Research Objectives

Ideal vitreous substitutes are easily implantable materials that mimic the structure and the properties of the native vitreous, perform its essential physiological functions, are biocompatible with the surrounding tissues, and are permanent. Our laboratory is steeped in vitreous related research and believes that a hydrogel that includes both a fibrillary and a semi-flexible component would be a truer biomimetic of the native vitreous, because of two main reasons: First, they would meet the essential requirements of an ideal vitreous substitute. Second, understanding the interplay of these two components would provide greater insights into the physiology and pathophysiology of the native vitreous.

Therefore, in this dissertation, my objectives, as a productive team member, are the following:

- a) To understand the complex anatomy and physiology of eye.
- b) To investigate the structure-property relationships of the two-component (rigid and flexible) hydrogel proposed by Dr. Ravi, and formulate the hydrogel that mimics the properties and functions of the native vitreous.

- c) To investigate the osmotic and oxygen diffusive properties bio-mimetic hydrogel, because they are critical for reducing post-vitreotomy complications.
- d) To evaluate the biocompatibility (*in vitro* and *in vivo*) of the hydrogel, in collaboration with the research members of our laboratory.

The two-component bio-mimetic hydrogel will consist of thiol derivatives of a fibrillary biopolymer and a semi-flexible polyelectrolyte. The fibrillary component is a biopolymer – gellan, and the semi-flexible component is poly[methacrylamide-co-(methacrylic acid)] based polyelectrolyte. The rigid component of our hydrogel, gellan, is a bio-polysaccharide, which undergoes sol-gel transition at a certain temperature and forms a physical gel almost instantaneously. This transition also occurs in the presence of mono/divalent cations. It is a stiff-biopolymer that has helical conformation below its transition temperature and swells minimally, analogous to collagen. Also, it is used in ophthalmic applications [43, 75]. On the other hand, the poly[methacrylamide-co-(methacrylic acid)] is a semi-flexible, ionic polyelectrolyte, which allows for variation in the swelling (osmotic pressure) and gelling properties of the hydrogels [76], analogous to HA at a mesoscopic level. Thiol groups will be endowed to both the polymer for safe and easy injection into the vitreous cavity, within which it will form an *in situ* hydrogel that is capable of generating osmotic pressure to reattach the retina.

Our central hypothesis is that the two-component composite hydrogel will (1) mimic the macroscopic-structure of native vitreous and exhibit optical, physical, rheological, and biocompatibility similar to those of the native vitreous, (2) and most importantly, generate osmotic pressure to reattach the retina.

As mentioned before, human vitreous has a density of 1.0053-1.0089 g/cm³ and a refractive index (RI) of 1.3345-1.3348 unlike the current vitreous substitute, silicone oil, with a

density of 0.96 g/cm³ and a refractive index of 1.404. It is transparent, and transmits more than 90% of visible light through it. Native vitreous is a viscoelastic solid with storage moduli higher than 10 Pa, and oxygen tension between 7-9 mmHg. The osmotic swelling pressure produced by the native vitreous within the vitreous cavity is not yet elucidated.

The central hypothesis was tested and addressed in three chapters as described below:

Chapter 2 discusses the polymer synthetic methodology for each component of the two-component hydrogel, followed by their characterizations, such as the degree of thiolation, their molecular weight distribution, structure, and composition. This chapter also briefly introduces the development of the two-component hydrogel.

Chapter 3 elaborates on the development of eleven two-component hydrogel formulations and discusses the effect of each component on their optical, physical, rheological, swelling, and sol-gel transition temperature properties. Two hydrogel formulations that most closely matched the properties of the native vitreous was then formulated and evaluated for the osmotic swelling pressure produced by them, and the oxygen transport through them.

Chapter 4 describes the investigations on the biocompatibility of the two optimized formulations of the hydrogel in contact with established ocular and fibroblast cells, and in approved rabbit models for one month. Furthermore, we also evaluated the resistance of these gels to degradation in enzymatic solutions and in the presence of ocular epithelial cells.

Chapter 5 summarizes the important conclusions of this entire work. Appendix A elaborates the development of the experimental response surface design, and Appendix B describes the optimization of the thiolation mechanism for the hyaluronic acid polymer to obtain the desired degree of thiolation. The insights gained from the thiolation mechanism were useful to synthesize the gellan component of the two-component hydrogel.

Chapter 2: Synthesis of the Two-Component Hydrogels

The vitreous is a meshwork of rigid rod-like collagen fibrils interspersed with flexible hyaluronic acid polymer chains. In this work, we reverse-engineered the critical aspects of the natural vitreous and developed a two-component bio-mimetic hydrogel. This chapter describes the synthesis and characterizations of each component of the hydrogel: (1) Thiolated gellan, which is a fibrillary polysaccharide analogous to collagen, and (2) poly[methacrylamide-co-(methacrylic acid)-co-*N,N'*-bis(methylacryloyl-cystamine)] (poly(MAM-co-MAA-co-BMAC)), a semi-flexible polyelectrolyte that is analogous to HA. The endowed thiol groups in each component cross-link with each other and form a permanent *in situ*-forming hydrogel. This chapter uses materials from References [69], and [77].

2.1 Materials and Methods

2.1.1 Materials

Reagents were purchased from Sigma Aldrich Co. (St Louis, MO) and used as received unless otherwise stated. Methacrylic acid (MAA) (99%) was purchased from Sigma Aldrich Co. (St Louis, MO) and vacuum distilled before using.

2.1.2. Thiolation of Gellan

A stock aqueous solution of gellan 1.33% (w/v) was prepared by dissolving the required quantity of gellan (4 g, 6.2 meq of COOH) in 300 mL of water at 70 °C. The pH of the gellan solution was adjusted to 4.5, and the solution was cooled to 50 °C. 1-Ethyl-3-(3-

dimethylaminopropyl) carbodiimide (EDC; 0.76 g, 4.0 mmol), N-hydroxysuccinimide (NHS; 0.26 g, 2.2 mmol), and cystamine dihydrochloride (Cys; 0.70 g, 6.2 mmol) were dissolved in 100 mL of water, and this solution was added to the gellan solution at 50 °C with stirring. The reaction mixture was continuously stirred and cooled to room temperature in 30 minutes. The mixture formed a gel at room temperature, and was allowed to react for four more hours. Thereafter, the reaction was terminated by adjusting the final pH to 8-9. The excess EDC, NHS, and Cys were removed from the reaction mixture by dialysis (Semi-permeable membrane with a molecular weight cut off (MWCO) 6000-8000) in de-ionized (DI) H₂O (three times). Then, the pH of the mixture was adjusted to 7.5, and the disulfide bonds were reduced with a 5 molar excess of Dithiotheritol (DTT) for 3 hours, yielding a solution. The excess DTT was removed by dialysis in N₂-bubbled 1 mM hydrochloric acid (HCl) (4 L, six times). Finally, the samples were analyzed for the degree of thiolation of gellan by using the 2-nitro-5-thiosulfobenzonate (NTSB) assay [78].

2.1.3. Synthesis of poly(MAM-co-MAA-co-BMAC)

A characteristic procedure for copolymerization of methacrylamide (MAM), MAA, and *N,N'*-bis(methylacryloyl-cystamine) (BMAC) is provided [69]. MAA was distilled at 45 °C under reduced pressure (~10 Torr) to remove the inhibitor and any impurities. A stock 2, 2'-Azobis(2-methylpropionitrile)/ Dimethylformamide (AIBN/DMF) solution (20 mg/mL) was made with 100 mg of AIBN and 5 mL of DMF. MAM (2.84 g, 33 mmol), MAA (0.78 g, 9.1 mmol), and BMAC (0.39 g, 1.35 mmol, and 2.7 meq of vinyl groups) were added to a 20 mL glass vial equipped with a magnetic stir bar and were dissolved in 16 mL of DMF. The solution was purged with nitrogen at 22 °C for 20 min to remove the dissolved oxygen. The stock AIBN/DMF solution (0.5 mL, 10 mg) was syringed into the vial, and the mixture was purged

with nitrogen for another 20 min at 22 °C. The reaction was incubated at 60 °C for 18 h. The obtained solid was suspended in 200 mL of DI water. The suspension was transferred to four 50 mL centrifuge tubes, and centrifuged at 2500 rpm for 10 min. The supernatant was decanted. This procedure was repeated three times to remove the DMF, and the DMF-free solid polymer was re-suspended in 200 mL of DI water.

A 1 N sodium hydroxide (NaOH) solution was added to the suspension to adjust the pH to ~7.75, yielding a viscous mixture. A 10-molar excess of DTT (0.69 g, 4.5 mmol) was added to reduce the disulfide bonds. The mixture was stirred at 22 °C for 18 h, and the suspension became clear and less viscous. An aliquot diluted to ≈ 2 mg/mL for gel permeation chromatography (GPC) characterization.

A 1 N HCl solution (20 mL) was then added to adjust the pH to ≈ 3 . A white solid precipitated and was separated via centrifuge (4000 rpm, 6 min). The product was washed four times with nitrogen-purged 1 mM HCl aqueous solution, followed by washing with a 1 mM HCl/ethanol solution. The copolymer was washed with nitrogen-purged 1 mM HCl aqueous solution again, and then lyophilized, yielding a white solid.

2.1.4 Characterizations of the Polymers

2-nitro-5-thiosulfobenzonate (NTSB) assay

The total disulfide content of the derivatized polymer, before and after reducing it with DTT, was determined, using the 2-nitro-5-thiosulfobenzonate (NTSB) assay [78]. Briefly, Cys standards, with concentrations from 0.05 to 1.5 mM, were prepared using a 10 mM Cys stock by serial dilution, using N₂-bubbled DI water. About 900 μ L of NTSB solution, prepared as described in the literature [78], was added to 100 μ L of the sample and the standards. Because

the reactions are photo-activated, assay samples were incubated in the dark for 15 minutes, and their absorbance was read with a spectrophotometer at 412 nm.

Ellman's reaction

The amount of thiol content was determined spectrophotometrically, using Ellman's reaction [79]. Briefly, 10 mg of each lyophilized sample was dissolved in 2 mL of N₂-bubbled water. About 500 μL of 0.1 M phosphate buffer (pH 8), 400 μL of water, and 50 μL of Ellman's reagent were added to 100 μL of the sample. Samples were incubated for 15 min at room temperature, and their absorbance was measured at 412 nm in a spectrophotometer. Thiol content was calculated by this equation:

$$\frac{-\text{SH (moles)}}{\text{g of polymer}} = \left(\frac{\text{Ab}}{13,600} \right) \times \left(\frac{V_{\text{total}}}{V_{\text{sample}}} \right) \times \left(\frac{1}{\text{Polymer conc}} \right), \quad [\text{Equation 1}]$$

where Ab is the absorbance, V_{total} is the total volume, V_{sample} is the sample volume, and 13,600 is the extinction coefficient. The concentration of the polymer (polymer conc) is in mg/mL.

¹H NMR spectroscopy

The polymer thiol contents and their purities were characterized using ¹H NMR spectroscopy on a Varian Unity Inova 500 (Palo Alto, CA). Polymer samples were dissolved in D₂O (8 mg/mL) with NaOD (20 μmol). NaOD was used to enhance the solubility of the polymers in D₂O. Each sample was scanned for 128 times at 25 °C.

Gel permeation chromatography (GPC)

The molecular weight of the reduced poly(MAM-co-MAA-co-BMAC) was determined using GPC. The GPC system employed a VE 1122 pump with a VE 7510 degasser (Viscotek/Malvern, Houston, TX, USA) that was equipped with a TDA302 triple detector system that measured the refractive index (RI), multi-angle laser light scattering, and viscosity. The column used was a G5000PWXL (Tosoh Biosep, Montgomeryville, PA, USA). Viscotek

Omnisec software was used to calculate the RI area, weight-averaged molecular weight, intrinsic viscosity, and hydrodynamic radius. Samples (100 μ L) were injected at a concentration of 2 mg/mL. The column buffer (pH 7.6) contained 20 mM of sodium phosphate, and the flow rate was 0.8 mL/min. The measurements were conducted at 37 $^{\circ}$ C.

2.2 Results and Discussion

2.2.1 Thiolation and Characterization of Gellan

Deacylated gellan gum is an anionic high molecular weight polysaccharide that has the repeat units of a tetra-saccharide (D-glucose, D-glucuronic acid, and L-rhamnose in a molar ratio of 2:1:1) [80]. Gellan undergoes a rapid phase change from a random-coil to a double-helix structure when cooled below their sol-gel transition temperature or in the presence of mono/divalent cations. The mechanism of gelation involves the formation of double helical junction zones followed by aggregation of the double-helical segments. Furthermore, complexation with cations and hydrogen bonding with water results in a 3-D rigid-rod-like fibrillar network [80, 81]. It is biocompatible and used in the food industry and ophthalmic medications (Timpotic XE) as a thickener, and in tissue engineering applications [82-84]. Du et al. [85] from our laboratory have chemically modified the gellan chains and endowed them with thiol group via carbodiimide chemistry. The thiol group air oxidized to form disulfide linkages, and hence a stable chemical cross-linked hydrogel. They demonstrated that the chemical modification did not alter the gellan's characteristic 3D conformation, and still had its quick physical gelation ability. The combination of physical and chemical gelation enabled the fabrication of injectable gellan hydrogels. Also, they showed that the sol-gel transition temperature decreases with increase in thiol modification. The thiolated gellan were also

biocompatible with retinal pigment epithelial cell lines and were a promising material for tissue engineering applications.

Carbodiimide chemistry is a well-established method for introducing chemical cross-links in polysaccharides. For instance, previously hyaluronic acid was thiolated via the carbodiimide chemistry. The effect of various factors, such as temperature, reactant concentrations, and pH, on the degree of thiolation of the hydrogel, was analyzed using the statistical design of experiments [86].

In this work, the carboxylic moieties of gellan were derivatized, with an amide-containing thiol group, cystamine dihydrochloride, via carbodiimide crosslinking chemistry (Figure 2.1). Mechanistically, the negatively charged carboxylate group attacks the electron-deficient diimide carbon atom on the carbodiimide molecule (EDC) to form the activated *O*-acylisourea intermediate. As a result, the carbon atom of the gellan's carboxylate group becomes sufficiently electron-deficient to be susceptible to nucleophilic attack by the lone pair of electrons on the amine group of the Cys, thereby forming an amide-substituted gellan molecule and acylurea. The *O*-acylisourea, which is very unstable, is usually stabilized by reacting with NHS, but still maintaining it in an active form. The amide-substituted gellan is reduced to thiol-substituted gellan (thiolated gellan), by using DTT. The thiolated gellan is then lyophilized and stored at -20 °C.

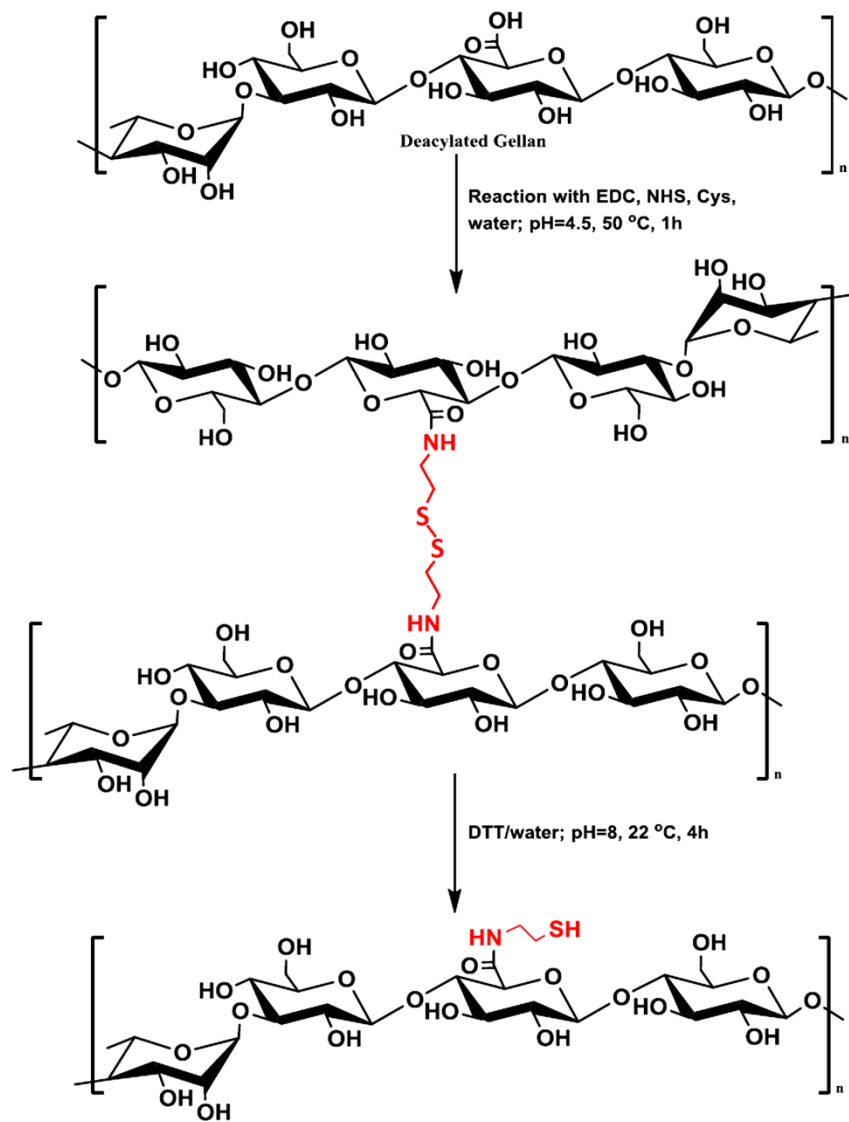


Figure 2.1: Reaction scheme for thiolation of gellan using carbodiimide chemistry.

Based on our previous studies, the biocompatibility and the sol-gel transition temperature of the hydrogel were noted to decrease with the increase in the thiol content. Therefore, the gellan was designed to have 11 mol % of thiolation for this study. The gellan was chemically modified and confirmed to have the thiol content as 11% (mol) of the repeat unit, using NTSB and Ellman's assay. The effect of concentration of thiolated gellan on the sol-gel transition

temperature, mechanical properties, and biocompatibility of the two-component hydrogels were determined and discussed in chapters 3 and 4.

2.2.2 Synthesis and Characterizations of poly(MAM-co-MAA-co-BMAC)

Copolymerization is a promising strategy to synthesize polymeric materials with properties that are tunable between those of the respective homopolymers. In this study, the desirable properties of MAM, MAA, and BMAC were combined to make copolymers suitable for use as a vitreous substitute. The MAM repeating units comprise the majority of the backbone, and the ionic MAA repeating units help the copolymers to form gels at a lower concentration, to increase the swelling ability, and the optical clarity. BMAC was incorporated into the copolymers to introduce pendent thiol groups, which were used as sites for reversible crosslinking. The disulfide bonds were reduced by DTT to generate a linear soluble thiol-containing copolymer. This reduced co-polymer, upon oxidation, reforms the original disulfide bonds and establishes a chemically crosslinked gel. The reactions are illustrated in Figure 2.2.

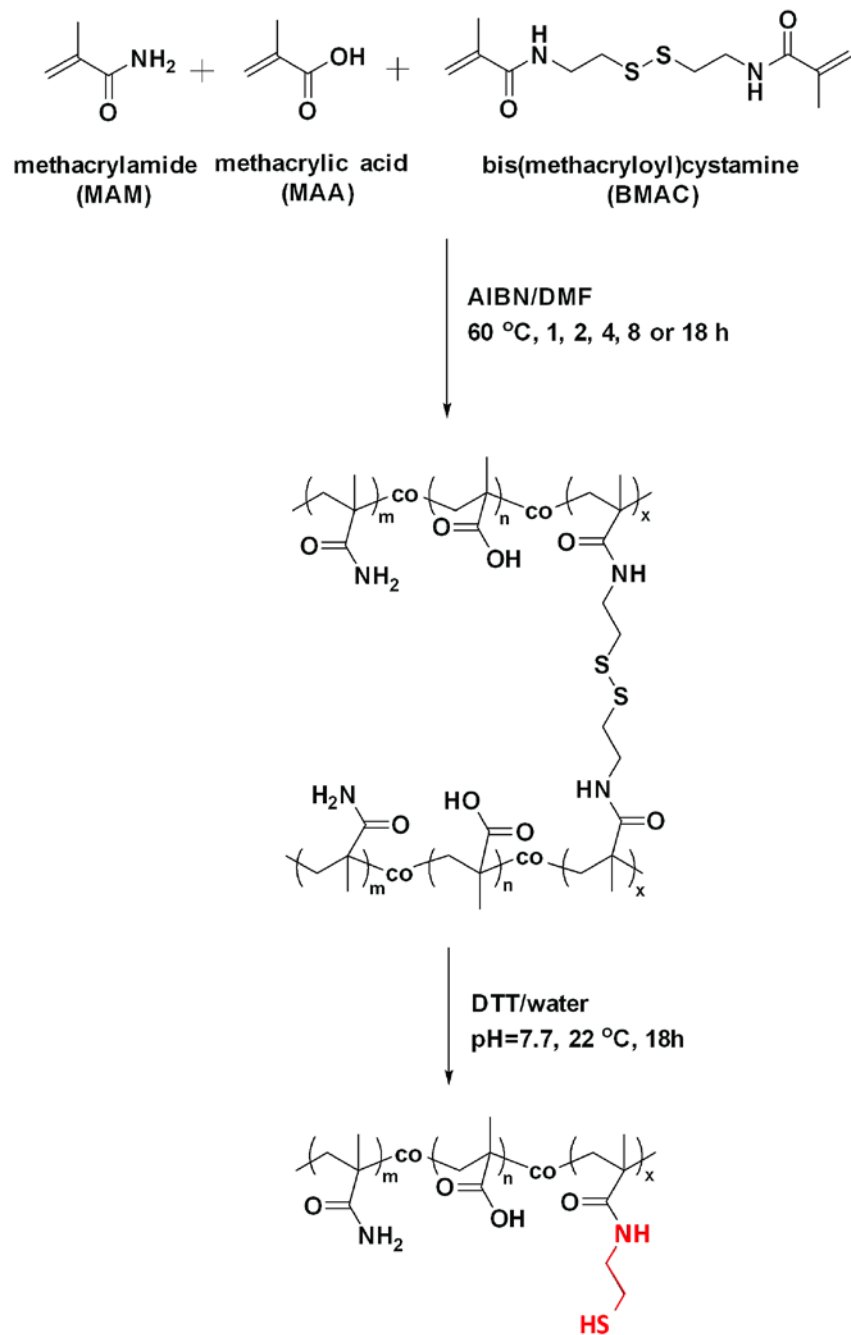


Figure 2.2: Copolymerization of MAM, MAA, and BMAC. (Figure reproduced from Liang et al. [69])

The molecular weight (M_n) of copolymers ranged from ≈ 100 k to ≈ 200 kDa, and their polydispersity indexes ranged from 1.47 to 2.63. The thiol content of the copolymer was 2% (mol), confirmed by NTSB assay, Ellman's assay, and ^1H NMR spectra (Figure 2.3). The effect of the MAA ionic component and the BMAC cross-linker in the copolymer and the

biocompatibility of the copolymer with various cell lines were studied in detail by my colleague Dr. Liang in the Ravi Laboratory. Liang et al. [87] showed that the poly(MAM-co-MAA-co-BMAC) with a 2% (mol) thiol cross-linker and a methacrylic acid content of 20% (mol) was a semi-flexible polymer, with a Mark-Houwink constant of 1.23. Furthermore, this copolymer was well-tolerated by ARPE-19 cells up to a concentration of 12.5 mg/mL. Beyond this concentration, increasing the mol % of thiol cross-linker was increasingly toxic to the cells.

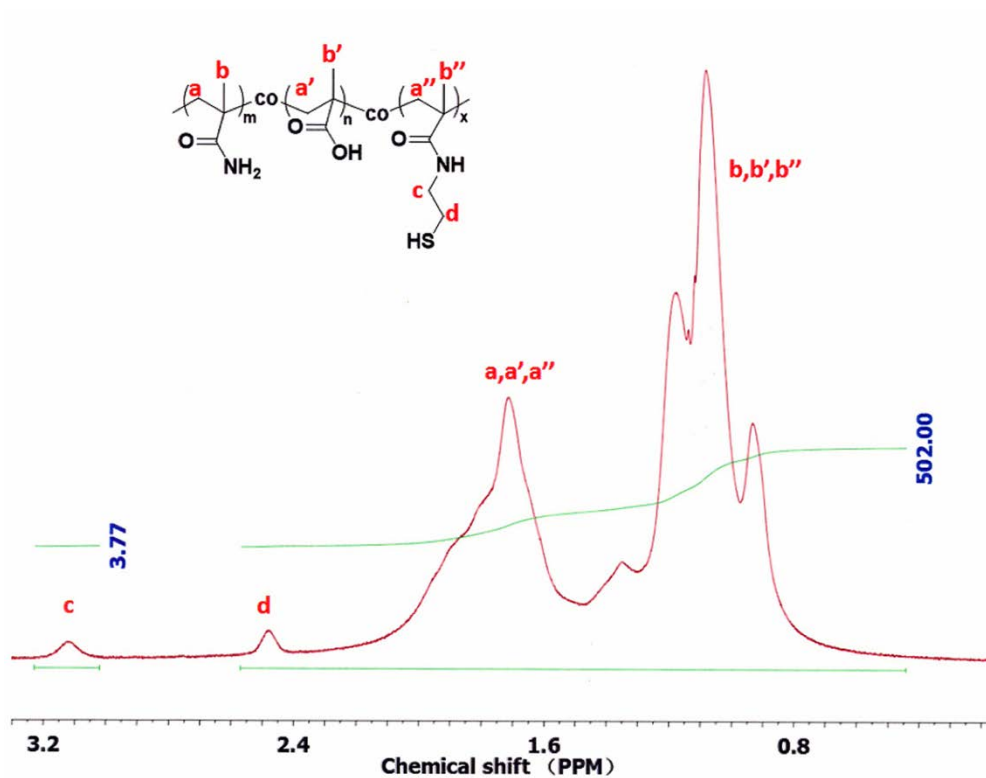


Figure 2.3: ¹H NMR spectra of poly(MAM-co-MAA-co-BMAC) in D₂O.

2.2.3 Development of Two-Component Hydrogels

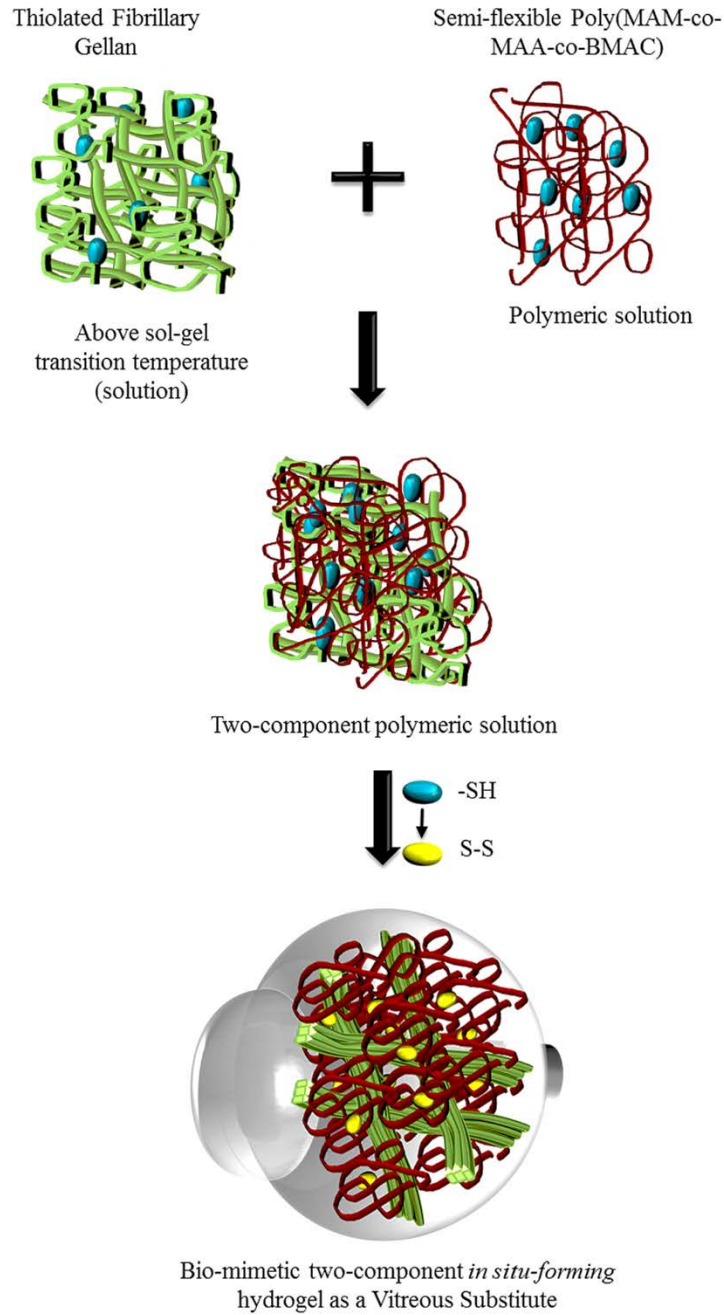


Figure 2.4: Schematic representation of our two-component polymer solution injected via syringe into the vitreous cavity. Thiolated gellan in the formulation undergoes phase-transition to form a physically cross-linked hydrogel instantaneously upon cooling. The thiols in the polymeric mixture oxidize to form mixed disulfide linkages and establish a chemically crosslinked network.

The two-component hydrogels were developed by mixing the polymeric solution of the rigid component of our hydrogel, thiolated gellan, and the semi-flexible ionic polyelectrolyte, poly(MAM-co-MAA-co-BMAC), at different proportions (Figure 2.4). The thiolated gellan in the polymeric mixture undergoes sol-gel transition at certain temperature, where the random coil polymer in the solution phase transforms to helical conformation almost instantaneously, forming a physically crosslinked gel. The physically crosslinked thiolated gellan network traps the copolymer, and prevents the diffusion of the polymer chains away from the location. The thiol groups in the physically crosslinked gel then oxidize over time to form a reversible chemically crosslinked hydrogel. The thiol cross-linkers make the hydrogel non-absorbable and non-degradable. They also provide easy injectability of the polymeric solution into the vitreous cavity, which is re-crosslinked by air-oxidation to form a gel *in situ*. The *in situ*-formed gel is superior when compared with a preformed gel, since the latter would be shear degraded by injection through a small gauge needle, and thus lose its elasticity and swelling ability that are necessary to hold the retina in place. Furthermore, the hydrogel can also be easily removed, by reducing the disulfide linkages back to thiol when needed. However, the inherent long-term stability and biocompatibility of the hydrogel should eliminate any need for its removal, avoiding secondary surgeries.

The properties of the two-component hydrogels are tunable with the change in concentration of each component. To ascertain the composition of this two-component hydrogel that can mimic the properties of natural vitreous, the optical, physical, mechanical, transition temperature, osmotic swelling, and biocompatible properties of a series of statistically designed (Response surface methodology, RSM) hydrogels (Chapters 3, and 4) were evaluated.

2.3 Conclusions

We have designed a potentially reversible *in situ*-forming two-component hydrogel that mimics the macroscopic composition of the native vitreous. The components are gellan, an analogue of collagen, and poly[methacrylamide-co-(methacrylic acid)], an analogue of hyaluronic acid; both endowed with thiol side groups. The degree of thiolation was found to be 11 % (mol) for gellan and 2 % (mol) for the copolymer. The thiolated gellan has the ability to form physical gel instantaneously upon cooling below its sol-gel transition temperature. The physically cross-linked thiolated gellan network traps the copolymer, and prevents the diffusion of the polymer chains away from the location. The thiol groups in the physically cross-linked gel then oxidize over time to form a reversible chemically cross-linked hydrogel. The effect of concentration of each component on the network properties of the two-component hydrogels is evaluated in the next chapter.

Chapter 3: Network Properties of the Two-Component Hydrogels

This chapter describes the network properties of the two-component hydrogels. Response surface methodology (RSM) was used to consider seventeen hydrogels, and to determine how each component affects their optical, mechanical, sol-gel transition temperature, and osmotic swelling properties. Three hydrogel formulations whose properties most closely matched those of the native vitreous were selected for biocompatibility evaluations. Two of the best performing hydrogels were further evaluated for their capacity to produce osmotic pressure, and for oxygen transport through them. Part of the work described in the chapter uses materials from reference [77].

3.1 Materials and Methods

3.1.1 Materials

All reagents were purchased from Sigma Aldrich Co. (St Louis, MO) and used as received unless otherwise stated. MAA (99%) was purchased from Sigma Aldrich Co. (St Louis, MO) and vacuum distilled before using.

3.1.2 Response Surface Method Design

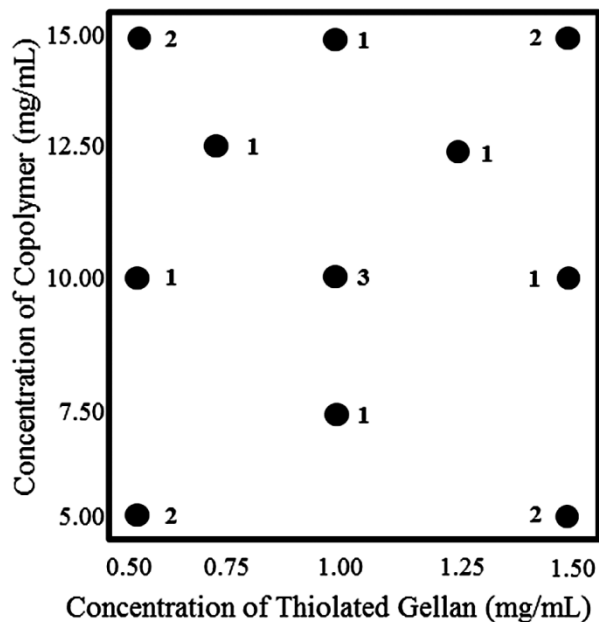


Figure 3.1: Design points used in the D-optimal design of RSM. The variables – concentrations of thiolated gellan and poly(MAM-co-MAA-co-BMAC) – were varied between 0.5 – 1.5 and 5.0 – 15.0 mg/mL respectively. The points represent each hydrogel formulation, and the numbers represent the number of replicates at each point.

To observe the relationship between the variables that govern the experiment and one or more responses, we used D-Optimal design of RSM (Design-Expert® software, version 7, Stat-Ease, Minneapolis, MN) with additional center points and replicates. The concentrations of thiolated gellan and poly(MAM-co-MAA-co-BMAC) were the two variables. Five different concentrations, of each were considered, with two replicates at each vertex of the design space and three replicates at the center point. In all, there were 17 hydrogel samples, with 11 formulations, as shown in Figure 3.1. Each formulation was characterized for storage modulus, loss modulus, refractive index, optical transmittance, density, sol-gel transition temperature, and degree of swelling.

Using the optimization tool available in the Design-Expert software, we selected three hydrogel formulations with refractive indexes between 1.334-1.338, densities between 1.002-

1.009, an optical transmittance greater than 85% in the visible wavelength, storage moduli between 100-200 Pa, and transition temperatures between 38-41°C. The three optimized formulations were used for *in vitro* biocompatibility studies. Two of the best performing gels were then chosen for further evaluation of the osmotic pressure they produced, oxygen transport through them, and their biocompatibility in rabbit eyes.

3.1.3 Two-Component Hydrogels Preparation

The thiolated gellan (synthesized as described in chapter 2) was dissolved at 2X the concentration of the final formulations (Table 3.1), in nitrogen (N₂) bubbled water. The poly(MAM-co-MAA-co-BMAC) (synthesized as described in chapter 2) was dissolved in 2X PBS (with 2% (v) Antibiotic/Antimycotic solution) at 2X the concentration of the final formulations. The pH of the solutions was adjusted to 7.5, they were separately heated to 55 °C for 15 minutes and finally mixed to investigate the sol-gel transition temperature. Three mL of the two-component polymer solution was immediately cast in a pre-weighed sterile 35-mm dish for rheological studies and was injected into a dialysis cassette with a semi-permeable membrane having a molecular weight cut off (MWCO) of 10 kDa (Slice-A-Lyzer, Thermo Scientific, Rockford, IL) for osmotic swelling studies. To form the S-S crosslinked two-component hydrogel, the two-component polymeric solution with thiol groups was oxidized for a week at 37 °C in a humidified chamber. The gelling of the two-component polymer solution was confirmed by tilting the dishes at 45° and checking for resistance to flow. Then, 1X PBS (- Ca²⁺, -Mg²⁺) was added to the dishes, and the gels were left at 37 °C for an additional seven days to reach equilibrium swelling, defined as when there was no more increase in the weight of the hydrogel.

3.1.4 Sol-Gel Transition Temperature Measurements

The sol-gel transition characteristic of each hydrogel formulation was measured using a Vilastic-3 oscillatory tube rheometer (Vilastic Scientific Inc., Austin, TX). The polymeric solution at 55 °C was filled into the oscillatory tube of the rheometer and cooled to 15 °C. The storage moduli of each polymeric solution were measured continuously as it transformed into a hydrogel. This thermal scan was performed at a 5% constant shear strain and 1.0 Hz constant frequency. A 3X molar excess of glutathione was added to the samples during measurement to prevent disulfide cross-linking.

3.1.5 Shear Modulus Measurements

To determine the shear modulus, frequency scans were performed for the hydrogels at 37 °C, using a plate-plate type modular compact rheometer (MCR rheometer; Anton Paar, TX, USA). Before testing, the excess PBS ($-\text{Ca}^{2+}$, $-\text{Mg}^{2+}$) was removed from the swollen hydrogels in the 35 mm dishes. The hydrogels, still in the 35 mm dishes, were cut to 21 mm diameter cylinders with a custom-made cutter, and the perimeter material was discarded. The rheometer was initialized for zero height between its plates and then was fully opened. The dishes containing 21 mm diameter hydrogel cylinders were placed on the bottom plate of the rheometer, and the top plate was brought into contact with the gel and kept there by a pneumatic positioning system. A small force (0.2 N) was applied to the gel to ensure good contact between the gel-plate systems (top plate, 20 mm diameter). For a range of frequencies, from 0.1 to 10 Hz, the shear modulus of the hydrogel was measured at a 2% strain and a constant temperature of 37 °C.

3.1.6 Osmotic Swelling Behavior of Hydrogels

The osmotic swelling pressure of polymeric hydrogels was determined by the macroscopic swelling/de-swelling technique [88-90]. This technique is based on the principle that the swelling pressure of a hydrogel becomes equal to the known osmotic pressure exerted by the surrounding macromolecular polymer solution at equilibrium. Three sets of experiments were performed to determine the swelling/de-swelling of hydrogels using this technique.

In the first experiment, 17 hydrogels of 11 different formulations, designed previously using RSM [77], were swollen in a 1X PBS bathing solution and kept in a humidified chamber at 37 °C until they reached equilibrium. In the second experiment, the 17 hydrogel samples were investigated when immersed in poly (vinylpyrrolidone) (dissolved in 1X PBS) (PVP, 29 kDa) [91] solution at 3 kPa osmotic pressure. In the third experiment, the two optimized hydrogel formulations, 0.9G_12CoP and 1.5G_10CoP (n=5 each), were swelled/de-swelled in poly(ethylene glycol) solutions (dissolved in 1X PBS) (PEG, 20kDa) [92] at different osmotic pressures. The polymer volume fraction of the gel at equilibrium with the surrounding solution was measured and normalized to the initial polymer volume fraction, to obtain the volume ratio of polymer injected into the cavity to that of the vitreous removed.

In all the experiments, three mL of each polymeric solution at 48 °C was injected into the dialysis cassettes with semi-permeable membranes having a molecular weight cut off (MWCO) of 10 kDa, gelled, and swelled in 1X PBS at 37 °C till it reached equilibrium. At equilibrium, there was no more change in the weight of the hydrogel. Each swollen gel was then immersed in a macromolecular solution of known osmotic pressure at 25 °C till it reached equilibrium. The dialysis membrane selectively prevented the entry of external polymeric macromolecules into the hydrogel. The change in weight of the hydrogels before and after the immersion in external

solution was recorded. The degree of swelling/de-swelling of the hydrogel was normalized to the DoS of the initially formed gel, as given in Equation (2):

$$\text{Normalized DoS} = \frac{\left(\frac{W_s - W_d}{W_d}\right)}{\left(\frac{W_i - W_d}{W_d}\right)} = \left(\frac{W_s - W_d}{W_i - W_d}\right),$$

[Equation 2]

where W_s is the final swollen weight of the hydrogel in equilibrium with the surrounding solution, W_d is the dry weight of the hydrogel, and W_i is the initial weight of the fully formed hydrogel. According to Equation (2), hydrogels that neither swell nor de-swell have a value equivalent to 1. Swollen gels have a value > 1 , in contrast to de-swollen gels, which have a value < 1 .

3.1.7 Optical and Physical Properties of Hydrogels

Refractive Index

The refractive indexes of the hydrogel samples were determined at 552 nm in an Abbe refractometer (ATAGO Abbe Refractometer NAR-1T, Kirkland, WA) kept at 37 °C.

Optical Transmittance

A UV/VIS spectrophotometer (DU800; Beckman Coulter Inc., Brea, CA) was used to measure the transmittance of light (280–800 nm) at 25 °C.

Density

The mass of 100 μL of the hydrogel at 25 °C was determined. The mass of 100 μL of water and its density at 25 °C were used as references to find the relative density of the hydrogel.

3.1.8 Oxygen Transport Studies

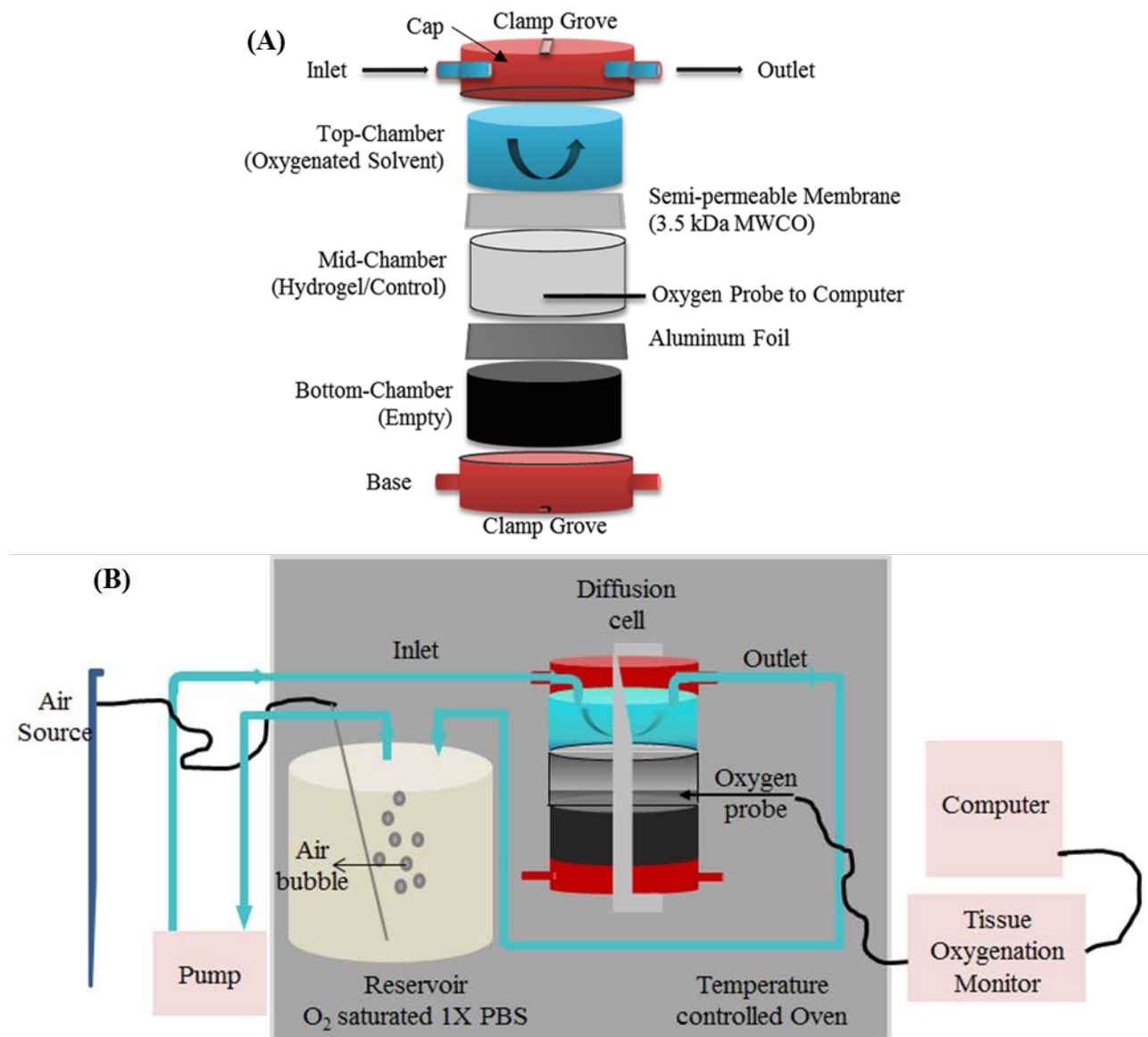


Figure 3.2: Experimental set-up of the 1D-diffusion chamber. (A) Three-chamber diffusion cell. (B) Schematic diagram of overall set-up (not drawn to scale). In a three chamber diffusion cell set-up, the top-chamber is filled with a flow of aerated solvent (1X PBS) via the inlet and outlet at 10 mL/min. The mid-chamber is filled with the hydrogel sample/controls, and the bottom chamber remains empty. The top- and the mid-chambers are separated by a semi-permeable membrane with a MWCO of 3.5 kDa, whereas the bottom chamber is blocked by an aluminum sheet instead of a semi-permeable membrane. At 10 mm from the top of the mid-chamber, there is a 1mm hole, through which a 21G 1 ½" needle containing the oxygen measuring probe (OxyLab pO₂ E-Series Sensor) is inserted. The oxygen probe is connected to a computer interface that records the measured partial pressure data in real time.

A three-segment diffusion chamber was designed, as shown in Figure 3.2. Each chamber is made of acrylic and measures 14 mm high, 25 mm in outer diameter, and 19 mm in inner diameter. The experimental method is first validated by measuring the diffusion of oxygen in water at 23 °C and 38 °C. Upon confirming the validity of the method, the mid-chamber is filled with either 0.9G_12CoP or 1.5G_10CoP hydrogel, or with a control: balanced salt solution (BSS), or silicone oil (SO).

To fill the mid-chamber with hydrogel, first the conical bottom was cut off a 50 mL plastic centrifuge tube with its cap attached, forming an upside-down dish. Then, the dish was inverted, the mid-chamber was slide in through the open bottom, and was filled by pipette with polymer solution at 50 °C. The dish and mid-chamber together were placed in a humidified chamber, where over the course of \approx one week, the vitreous substitute oxidized from a physically crosslinked gel (-SH) to a chemical crosslinked (S-S) gel. The mid-chamber containing the hydrogel sample was then gently removed from the dish. To remove free oxygen from the hydrogel sample prior to diffusion studies, the gel-filled mid-chamber was placed in a sealed 1X PBS bath that was continuously bubbled with nitrogen for at least 2 hours. After de-oxygenation was confirmed by probe measurement, the mid-chamber was removed from the 1X PBS bath, and assembled with the other segments just prior to diffusion studies. For the controls, the oxygen was removed directly by purging nitrogen gas through the control solution placed in a sealed glass tube (5 mL). The oxygen-deficient control solution was then injected into the assembled mid-chamber (procedure discussed below) via needle slowly, without inducing air bubbles.

The three chambers were assembled as shown in Figure 3.2. The top-chamber is filled with a circulating aerated solvent (1X PBS) via the inlet and outlet. The solvent reservoir was

continuously purged with air, and the oxygen saturated solvent concentration was confirmed by probe measurement. As shown in Figure 3.2A, the top- and the mid-chambers are separated by a semi-permeable membrane with MWCO 3.5 kDa. The semi-permeable membrane was checked for its flatness, without any bulging. The mid-chamber contains the hydrogel sample. The bottom chamber remains empty, blocked by an aluminum sheet. Rubber O-rings at the outer faces of the top and bottom chambers prevent leaks when clamped. At 10 mm from the top of the mid-chamber, there is a 1 mm hole, through which a 21G 1½" needle containing the oxygen measuring probe (OxyLab pO₂ E-Series Sensor, Oxford Optronix Ltd., Oxford, U.K.) is inserted. For the control experiments, the de-oxygenated control solutions were injected via the same hole into the mid-chamber prior to oxygen probe insertion. Care was taken to make sure that the diffusing medium was fully-filled without entrapping any air bubbles. The entire set-up, comprising the three-chamber diffusion cell, solvent reservoir, and the oxygen probe, were placed inside an oven to maintain a constant temperature. The temperature of the oven was continuously monitored throughout the experiment. The constant temperature was also confirmed for a few experiments, by using the oxygen probe with a temperature sensor. The oxygen probe injected into the sample chamber was connected to a computer interface (OxyLab – Tissue oxygenation monitor) via LabView® software that records the measured oxygen partial pressure (pO₂) in real time.

Measurements were taken from a fixed displacement point within the diffusion chamber and exported from the software interface into Microsoft Excel or a text file. To yield a value for the diffusion constant, the data was subsequently fitted to the analytical solution obtained after solving the diffusion equation [93] derived in the next section.

Derivation of Diffusion Equation

The Fick's second law is given as

$$\frac{\partial C}{\partial t} = D \nabla^2 C + R.$$

[Equation 3]

The assumptions are (1) $R = 0$, because there is no mass generation, (2) the oxygen diffuses in one dimension, (3) The rigid acrylate diffusion cell is impermeable to gas, imposing no flux at the cell edges. Based on the assumptions, the equation (3) is simplified to one dimension

$$\frac{\partial C}{\partial t} = D \frac{\partial^2 C}{\partial x^2}.$$

[Equation 4]

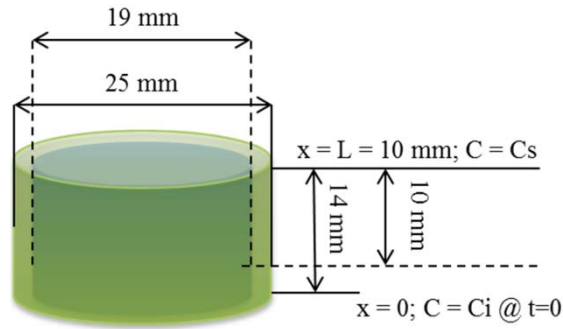


Figure 3.3: Boundary conditions for oxygen transport through the hydrogels

The boundary conditions (Figure 3.3) are as follow:

At $x = 0$, the flux, $\frac{\partial C}{\partial x} = 0$.

At $x = L$, the solvent is continuously aerated and the solvent is oxygen saturated, hence $C = C_s(x)$.

At $t = 0$, a specified initial concentration profile is assumed to be $C = C_i(x)$.

Converting the variables to dimensionless form yields

$$\frac{\partial \phi}{\partial \tau} = \frac{\partial^2 \phi}{\partial \eta^2},$$

[Equation 5]

where the dimensionless concentration $\phi = \frac{C-C_s}{C_i-C_s}$; C_s is the saturation concentration, which is assumed to be the maximum concentration; and C_i is the initial oxygen concentration, which is assumed as the minimum concentration in the experimental data. The dimensionless time is given as $\tau = \frac{t}{t_{ref}} = \frac{tD}{L^2}$, and the dimensionless distance $\eta = \frac{x}{L}$.

The boundary conditions for the dimensionless form are as follow:

At $\eta = 0$, the flux, $\frac{\partial \phi}{\partial \eta} = 0$.

At $\eta = 1$, solvent is oxygen saturated and hence, $\phi = 0$.

At $t = 0$, $\phi = 1$, which is a uniform starting profile.

The general solution to Equation 4 via separation of variables is of the form

$$\phi = \exp(-\lambda_n^2 \tau) F_n(\eta),$$

[Equation 6]

where λ_n is a constant. Substituting the general solution for ϕ in equation 4, we require

$$\frac{\partial^2 F_n}{\partial \eta^2} + \lambda_n^2 F_n = 0.$$

[Equation 7]

The general solution is

$$F_n = A_n \cos(\lambda_n \eta) + B_n \sin(\lambda_n \eta),$$

[Equation 8]

where A_n and B_n are integration constants. Now, applying the boundary conditions to the above general solution, we get the following:

At $\eta = 0$, $B_n=0$, hence $F_n = A_n \cos(\lambda_n \eta)$.

At $\eta = 1$, $A_n \cos(\lambda_n \eta) = 0$.

$A_n \neq 0$, because the solution will be trivial if $A_n = 0$. Therefore,

$$\lambda_n = \left(n + \frac{1}{2} \right) \pi ,$$

where $n= 0,1,2,3,\dots$ F_n is a eigenfunction. A series solution that incorporates all the values of n is given below:

$$\phi(\eta, \tau) = \sum_{n=0}^{\infty} A_n \exp(-\lambda_n^2 \tau) \cos(\lambda_n \eta).$$

Using the initial condition, at $\tau = 0 \longrightarrow \phi = 1$, we have

$$\phi(\eta, \tau) = \sum_{n=0}^{\infty} A_n \cos(\lambda_n \eta) .$$

[Equation 9]

To find A_n , we use the orthogonal property of the F function, which is stated as

$$\int_0^1 \mathbf{F}_n(\boldsymbol{\eta}) \mathbf{F}_m(\boldsymbol{\eta}) d\boldsymbol{\eta} = \mathbf{0} \text{ if } \mathbf{n} \neq \mathbf{m}.$$

Expanding Equation 9 gives

$$\phi_i(\eta) = A_0 \cos(\lambda_0 \eta) + A_1 \cos(\lambda_1 \eta) + A_2 \cos(\lambda_2 \eta) + A_3 \cos(\lambda_3 \eta) + \dots.$$

Multiplying both sides by $\cos(\lambda_1 \eta)$, we get

$$\begin{aligned} \phi_i(\eta) \cos(\lambda_1 \eta) &= A_0 \cos(\lambda_0 \eta) \cos(\lambda_1 \eta) + A_1 \cos^2(\lambda_1 \eta) + A_2 \cos(\lambda_2 \eta) \cos(\lambda_1 \eta) \\ &+ A_3 \cos(\lambda_3 \eta) \cos(\lambda_1 \eta) + \dots. \end{aligned}$$

Integrating from 0 to 1 with respect to η , only the A_1 term remains on the RHS, and upon rearranging, we get A_1 as

$$A_1 = \frac{\int_0^1 \phi_i(\eta) \cos(\lambda_1 \eta) d\eta}{\int_0^1 \cos^2(\lambda_1 \eta) d\eta}$$

By numerical integration, A_1 can be computed for any prescribed initial conditions. The general solution for A_n is given by

$$A_n = \frac{\int_0^1 \phi_i(\eta) \cos(\lambda_n \eta) d\eta}{\int_0^1 \cos^2(\lambda_n \eta) d\eta}.$$

Applying a constant initial concentration $\phi_i = 1$, the series coefficients are

$$A_n = \frac{2(-1)^n}{\left(n + \frac{1}{2}\right) \pi}.$$

For oxygen transport through a short length $x = 0.01$ m, just one term may be sufficient for a reasonable estimate of the concentration profile. Therefore, using a term approximation of

$$A_0 = \frac{2(-1)^0}{\left(0 + \frac{1}{2}\right) \pi} = \frac{4}{\pi},$$

the concentration is given as

$$\phi(\eta, \tau) = A_0 \exp(-\lambda_0^2 \tau) \cos(\lambda_0 \eta)$$

$$\lambda_0 = \frac{\pi}{2}$$

$$\phi(0, \tau) = \frac{4}{\pi} \exp\left(-\left(\frac{\pi}{2}\right)^2 \tau\right).$$

[Equation 10]

Taking \log_e on both sides, we get

$$\ln(\phi) = \ln\left(\frac{4}{\pi}\right) - \left(\frac{\pi}{2}\right)^2 \tau = \ln\left(\frac{4}{\pi}\right) - \left[\left(\frac{\pi}{2}\right)^2 \times \frac{tD}{L^2}\right].$$

[Equation 11]

The measured oxygen partial pressure was converted into a dimensionless concentration, and transformed to the logarithmic domain to obtain $\ln(\phi)$. $\ln(\phi)$ was then plotted against time (t). The data was smoothed in SigmaPlot® (version 14, Systat software, Inc., San Jose, CA), using a local smoothing technique that employs a negative exponential regression. The sampling proportion was 0.1, and the outliers were rejected. The slope of the smoothed plot was calculated, by linear curve fitting for Equation 11 with the constant intercept. The slope of the plot is equivalent to $\left(\frac{\pi}{2}\right)^2 \times \frac{D}{L^2}$, from which the diffusion coefficient is calculated.

3.1.9 Statistical Analysis

Results of hydrogel characterizations and surface model fittings designed from RSM were statistically analyzed in Stat-Ease, using analysis of variance (ANOVA) with 95% confidence limits. All oxygen tension results are reported as mean \pm SE (standard error) (n = 3-5), where the error bars denote $\frac{SD}{\sqrt{n}}$. To compare the experimental groups to the control, an F-test was performed to analyze the variance between the groups, followed by a two-tailed t-test (assuming equal or unequal variances, based on the result from the F-test). A p-value < 0.05 was considered to be statistically significant.

3.2 Results and Discussion

RSM is a statistical tool to determine the effects of variables by performing a minimum number of experiments. It can also be used to optimize responses that are usually influenced by a number of important variables. In the D-optimal design algorithm, design points are optimally selected in the domain of interest that can deliver the maximum amount of information. In this study, the concentrations of each component were varied at five different levels, and their

influence on the physical, optical, mechanical, swelling, and temperature transition properties of the hydrogel was measured.

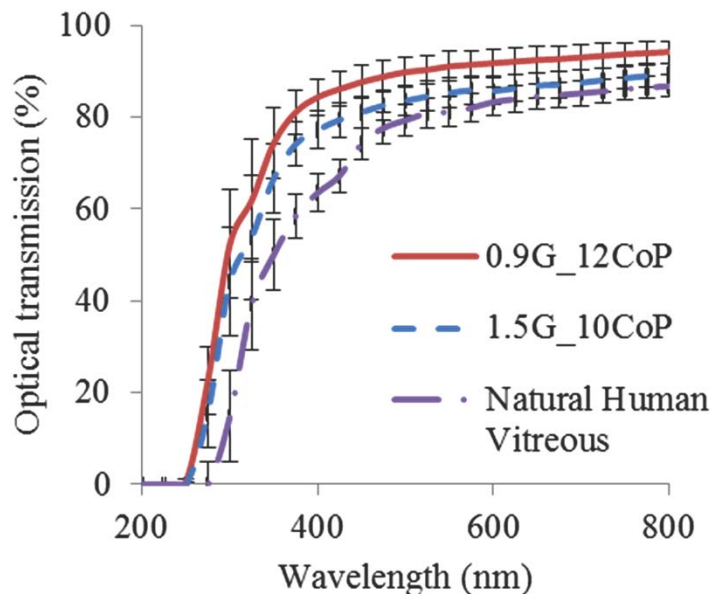


Figure 3.4: Optical transmittance (%) of natural vitreous and two-component hydrogels for wavelength from 200 to 800 nm. The hydrogels are either of formulation 1.5 mg/mL of thiolated gellan and 10 mg/mL of copolymer (1.5G_10CoP), or 0.9 mg/mL of thiolated gellan and 12 mg/mL of copolymer (0.9G_12CoP). Error bars are the standard deviation of three replicates of each sample.

The physical and optical properties of the 17 hydrogels did not vary drastically with varying formulations. Refractive index measurements ranged from 1.334-1.338, densities ranged from 1.002-1.009, and the optical transmittances were greater than 85% in the visible wavelength. The optical transmittance in the ultraviolet range dropped drastically and was zero below 275 nm, similar to that of the natural vitreous (Figure 3.4). In contrast, the sol-gel transition temperatures, storage and loss moduli, and the degree of swelling varied with varying formulations of hydrogel, as shown in Table 3.1. The upcoming sections discuss the effect of concentration of each component on their properties.

Table 3.1: Sol-gel transition temperature, storage and loss moduli, and percentage swelling for 17 hydrogels designed using RSM

Run Number, Number of Replicates in Brackets	Gellan Conc. [mg/mL]	CoP Conc. [mg/mL]	Sol-gel Transition Temp. [°C]	Storage Modulus @ 1 Hz [Pa] Swollen	Loss Modulus @ 1 Hz [Pa] Swollen	N. Degree of Swelling in 1X PBS	Weight % of Dried Polymer in Equb. Swollen Hydrogel [%]
1	0.75	12.5	37	51.3	3.12	1.37	1.28
2	1	10	41.5	106	4.55	1.55	0.9
3	1.5	15	42.5	358	50.3	1.54	1.36
4	1.5	10	41.5	178	7.48	1.41	1.01
5	1.5	5	39.5	151	12	1.38	0.58
6 (3)	1.5	15	41.8	199	10.2	1.68	1.29
7 (2)	1	10	40.8	115	13.9	1.12	1.04
8 (5)	1.5	5	40	138	3.82	1.25	0.62
9	1	7.5	41.8	67.7	4.47	1.35	0.79
10	0.5	10	36.8	35.1	4.45	1.43	0.95
11	0.5	5	35.5	3.05	1.18	1.29	0.54
12	0.5	15	40.5	113	38.8	1.48	1.26
13	1	15	42.5	143	7.7	1.54	1.29
14	1.25	12.5	43	173	8.52	1.60	1.15
15 (2)	1	10	41.5	91.8	5.02	1.60	0.94
16 (11)	0.5	5	36	21.1	3.35	1.23	0.55
17 (12)	0.5	15	38.8	120	28.7	1.52	1.27

3.2.1 Sol-Gel Transition Temperature Characteristics of Hydrogels

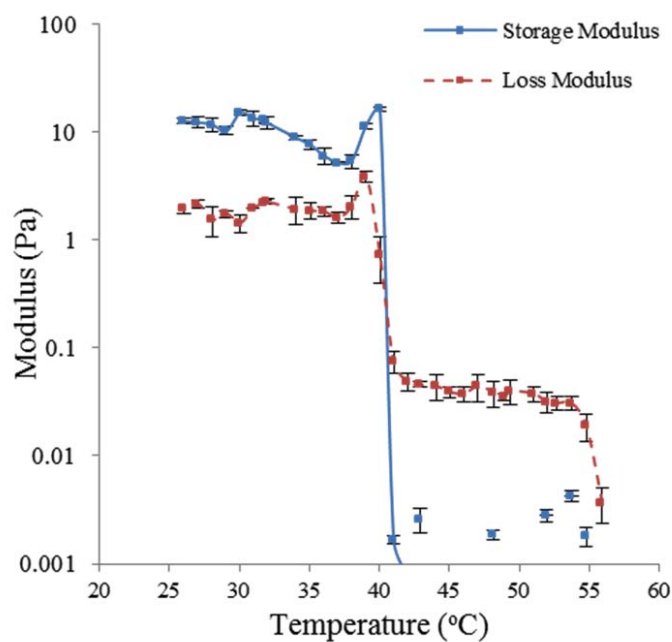


Figure 3.5: Temperature scans for a mixture of 0.9 mg/mL thiolated gellan and 12 mg/mL poly(MAM-co-MAA-co-BMAC).

The two-component hydrogels undergo rapid sol-gel transition upon cooling below their sol-gel transition temperature (T_{gel}). As seen in Figure 3.5, a polymeric solution of 0.9 mg/mL thiolated gellan (G) and 12 mg/mL poly(MAM-co-MAA-co-BMAC) (CoP), represented as 0.9G_12CoP, transitions to a gel at 40 °C upon cooling from 55 °C. At a temperature above this transition temperature, the viscosity (loss moduli) of the material is larger than its elasticity (storage moduli), indicating that the solution phase is dominant over the gel phase. Vice-versa, at a temperature below T_{gel} , the reverse is true, indicating the solid-like behavior of the material. Furthermore, the elastic physical gel, when oxidized with chemical crosslinks, is thermally irreversible and does not transition to a solution upon heating to a higher temperature.

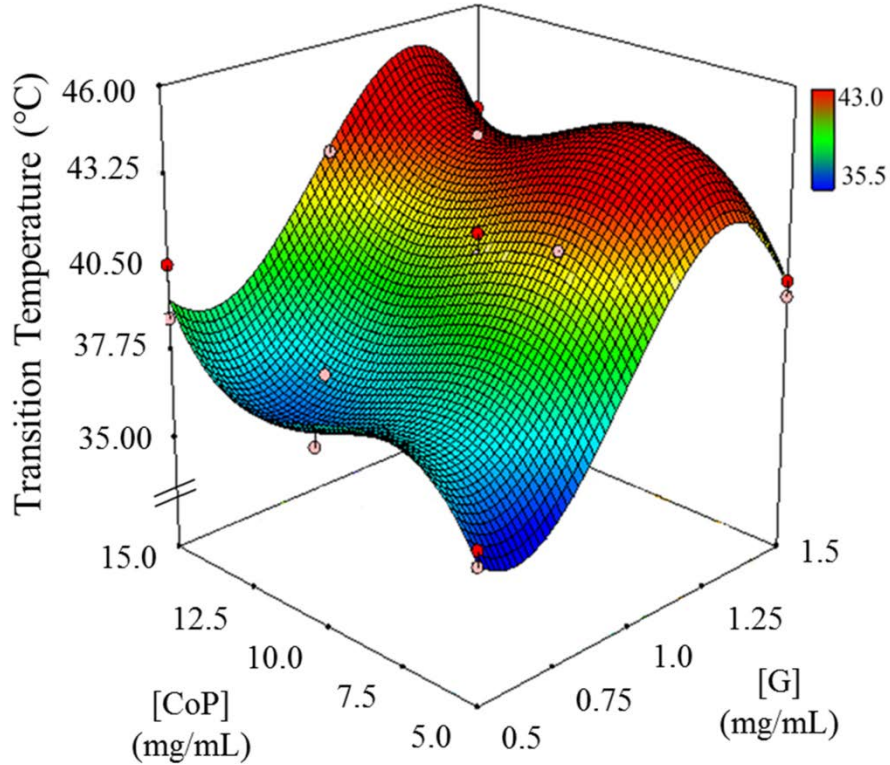


Figure 3.6: A modelled cubic surface plot of sol-gel transition temperature against the concentration of thiolated gellan and copolymer in mg/mL.  represents increasing transition temperature from 35.5 to 43 °C.

As Table 3.1 shows, the mixtures used in our work transition in the range of 35.5 to 42.5 °C, depending on their formulation. The experimental data for the hydrogels (Table 1) fits a cubic model (Figure 3.6). According to the ANOVA, the cubic surface fits the experimental data with a p-value of <0.0001 and a determination coefficient R^2 of 0.965. Based on the surface, the equation to predict the transition temperature is given below:

$$\text{Transition temperature} = 37.40 - 109.40 \times [G] + 8.93 \times [\text{CoP}] - 0.15 \times [G] \times [\text{CoP}] + 133.80 \times [G]^2 - 0.93 \times [\text{CoP}]^2 - 47.12 \times [G]^3 + 0.03 \times [\text{CoP}]^3 \quad [\text{Equation 12}]$$

where 37.4 is the intercept of the data, [G] is the concentration of thiolated gellan in mg/mL, and [CoP] is the concentration of copolymer in mg/mL.

The concentrations of both the components were statistically significant in governing the transition temperature of the hydrogel. Of the two, the concentration of thiolated gellan ($p < 0.001$) was considerably more significant than that of the copolymer ($p = 0.036$) in the range of concentrations that were investigated. Thiolated gellan is essential for the temperature-triggered instantaneous physical gelation of the hydrogel, and varying the concentration of the copolymer helps in tuning to achieve the desired T_{gel} . For instance, the T_{gel} increases as the concentration of copolymer increases (Figure 3.7).

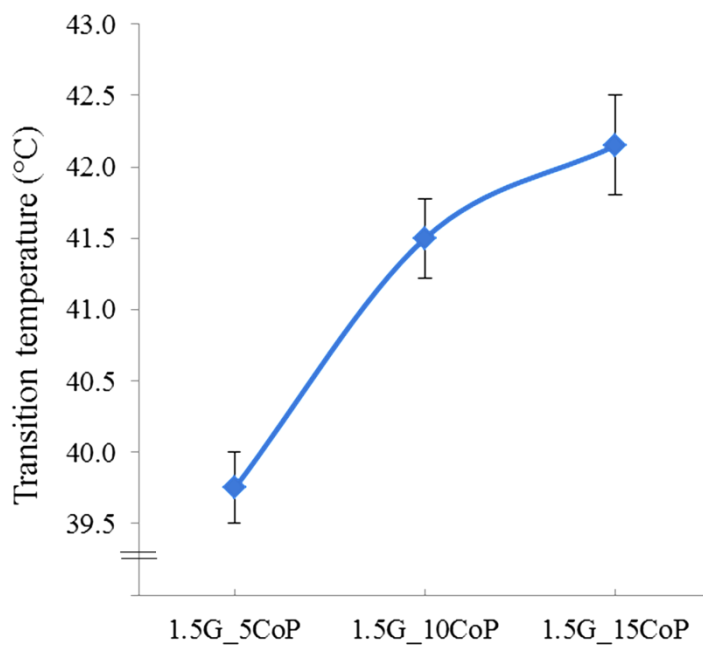


Figure 3.7: Variation in transition temperature of two-component hydrogels made of 1.5 mg/mL gellan combined with increasing concentrations of copolymer, from 5 mg/mL (1.5G_5CoP) to 15 mg/mL (1.5G_15CoP).

3.2.2 Rheological Characteristics of Hydrogels

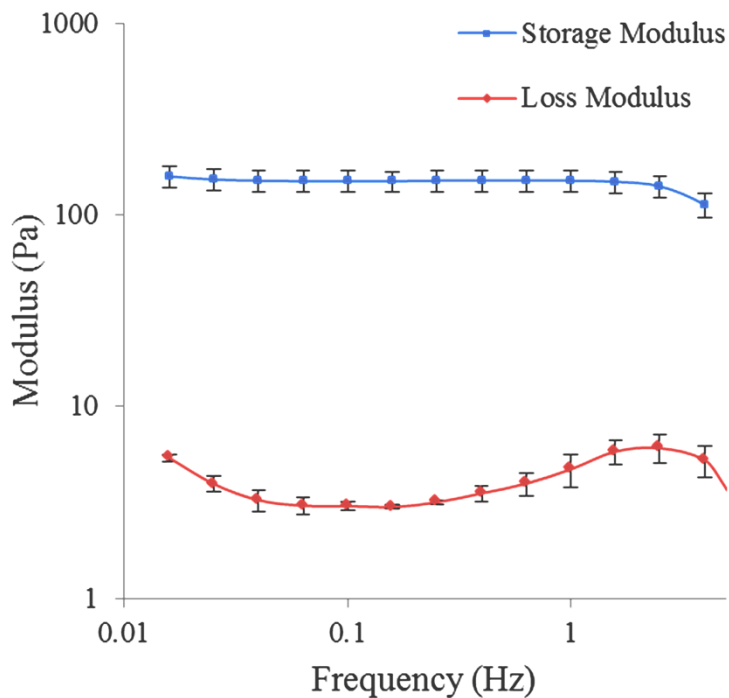


Figure 3.8: Storage and loss moduli of a two-component hydrogel 0.9 mg/mL thiolated gellan and 12 mg/mL poly(MAM-co-MAA-co-BMAC). The storage moduli were greater than loss moduli at all frequencies from 0.01-10 Hz, indicating a gel-like behavior.

The mechanical properties of the hydrogel, measured in terms of the storage modulus (G' ; elastic or solid component) and the loss modulus (G'' ; viscous or liquid component) from the frequency sweep, depends on the concentrations of the components of the hydrogel. The storage moduli were greater than the loss moduli at all frequencies from 0.01 to 10 Hz for all formulations of hydrogel, indicating a gel-like behavior. For instance, Figure 3.8 illustrates the storage and loss moduli characteristics of the 0.9G_12CoP hydrogel.

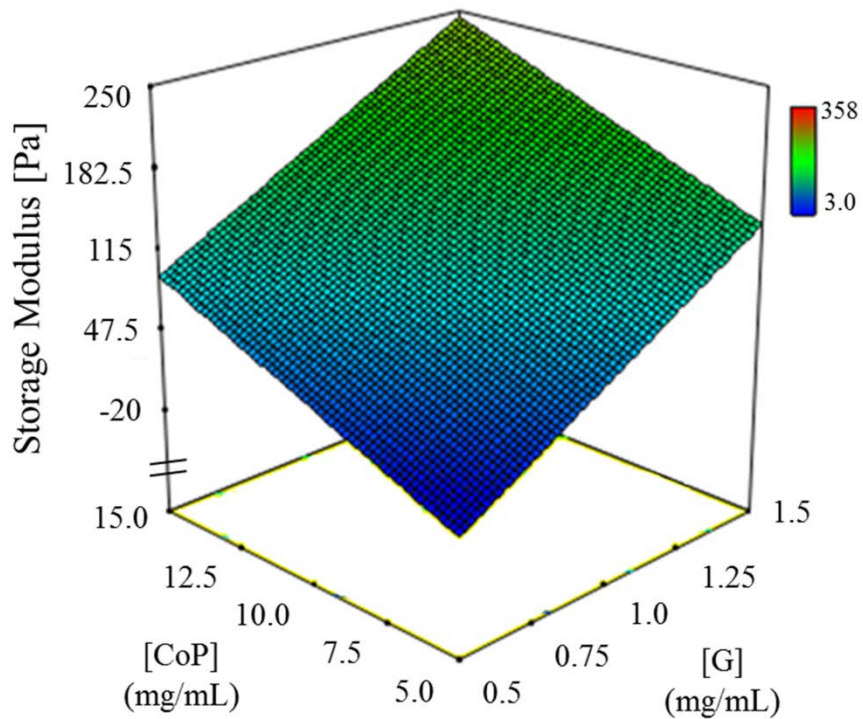


Figure 3.9: A modelled surface plot of storage modulus in Pa at 1 Hz against change in concentration of thiolated gellan and copolymer (CoP) in mg/mL. The storage moduli results from 17 two-component hydrogels were analyzed and fitted to the modelled surface with a p-value of <0.001 obtained from ANOVA.  represents the increasing storage modulus from 3 to 358 Pa.

The storage modulus of the swollen hydrogels ranged from 3.05 to 358 Pa, while the loss modulus was 1.18 to 50.3 Pa at a frequency of 1 Hz (Table 1). A linear regression model fits the experimental data for G' (Table 3.1) with a p-value of <0.001 and R^2 of 0.80. A planar surface was used to represent the variation of storage moduli with differing concentrations of thiolated gellan and copolymer (Figure 3.9). The storage moduli can be predicted using the polynomial equation for this linear fit, which is given by

$$\text{Storage Moduli} = -141.60 + 150.97 \times [G] + 10.73 \times [CoP], \quad [\text{Equation 13}]$$

where -141.60 is the intercept of the model. The negative value of the constant (intercept) has no practical application, because the model is not predicted at zero concentration of thiolated gellan and copolymer. The real value of this linear regression model is to understand how the storage moduli changes with a change in the values of the variables ([G], from 0.5 to 1.5 mg/mL, and [CoP], from 5 to 15 mg/mL).

The concentrations of both the components were found to significantly influence the stiffness and rigidity of the two-component hydrogel. Of the two, thiolated gellan (p-value <0.0001) was found to be a more significant factor than the copolymer (p-value 0.001). The storage modulus of copolymer component without thiolated gellan was ≈ 1.5 Pa at 9 mg/mL [76]. However, with the addition of thiolated gellan, the storage modulus of a two-component hydrogel of 10 mg/mL copolymer and 0.5 mg/mL thiolated gellan (Run #10, Table 1) was 35 Pa. Also, for a two-component hydrogel of 10 mg/mL copolymer and increasing concentrations of thiolated gellan (from 0.5 to 1.5 mg/mL), the G' increases from 35 Pa to 178 Pa. The thiolated gellan component contributes to the stiffness and rigidity of the hydrogel network.

3.2.3 Osmotic Swelling Characteristics of Hydrogels

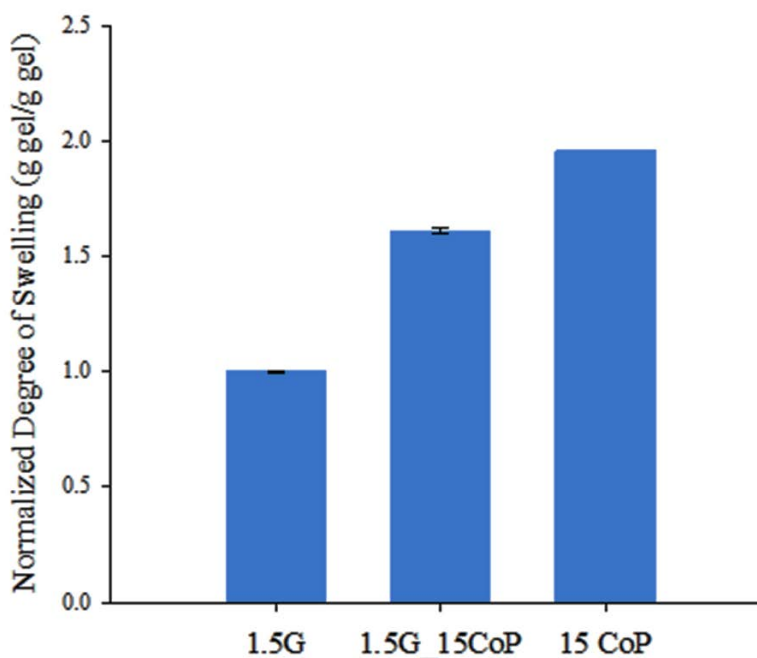


Figure 3.10: Normalized degree of swelling (DoS) of the two-component hydrogel, 1.5G_15CoP, compared to that of each of its component, thiolated gellan (1.5G) and CoP (15CoP), in 1X PBS.

Thiolated gellan hydrogels exhibited negligible swelling in 1X PBS, with a normalized DoS nearly equivalent to 1. In contrast, the poly(MAM-co-MAA-co-BMAC), due to its added charge density, were highly swellable (Figure 3.10) in 1X PBS. The swelling capacity of this copolymer increases with an increase in MAA content, or its concentration [87]. The 20 % (mol) MAA content in our copolymer offers the maximum possible swelling. On the other hand, the two-component hydrogels swelled in 1X PBS, and had a normalized DoS lower than that of the copolymer, CoP, and higher than that of the thiolated gellan, G (Figure 3.10). This intermediate degree of swelling demonstrates that in a two-component hydrogel, the copolymer's swelling capacity is restricted by the minimally swellable thiolated gellan fibrils, resulting in a swelling

behavior referred to as “controlled swelling behavior” in this work. This behavior results in a tightly swollen network with the capacity to produce a significant Donnan swelling pressure.

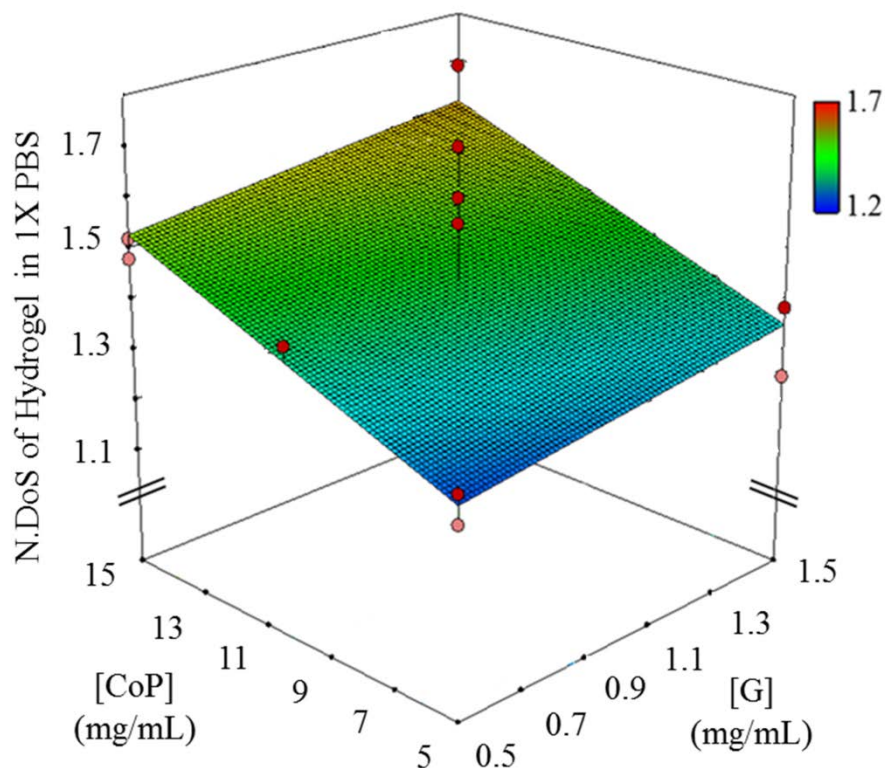


Figure 3.11: Surface model fit for normalized DoS of 17 hydrogels, designed using RSM, in 1X PBS for varying [G] and [CoP]. The color gradient represents increasing normalized DoS, from 1.2 to 1.7. The experimental results fit the modelled surface with a p-value of <0.001.

The degree to which the two-component hydrogel swells in the presence of water or physiological fluid depends on the hydrogel's composition. The normalized DoS of the two-component hydrogels range from 1.24 to 1.69. A linear regression model fits the experimental swelling data, tabulated in Table 3.1, with a p-value of 0.0008 and R^2 of 0.66 (Figure 3.11). The polynomial equation given in Equation 14 predicts the normalized degree of swelling.

$$\text{Normalized DoS} = 1.10 + 0.08 \times [G] + 0.03 \times [CoP], \quad \text{[Equation 14]}$$

where 1.101 is the intercept in the design space for [G], ranging from 0.5 to 1.5 mg/mL, and [CoP], ranging from 5 to 15 mg/mL. Therefore, normalized DoS was not interpreted at [G] = [CoP] = 0. The overall contribution of [CoP] was significant ($p < 0.01$) for hydrogel swelling in this defined concentration range.

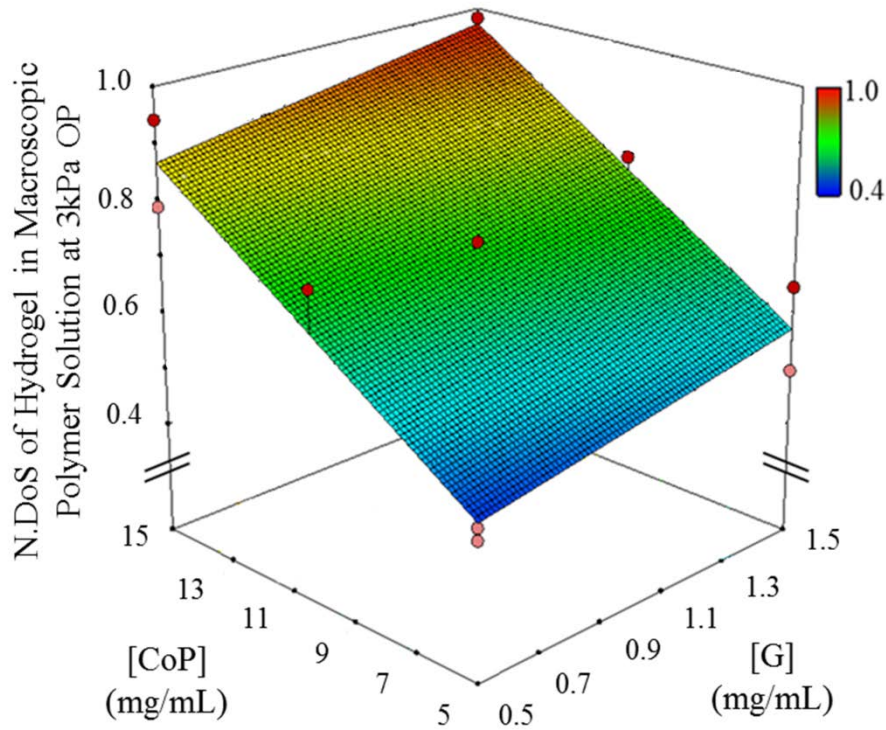


Figure 3.12: Surface model fit for normalized DoS of 17 hydrogels in macroscopic polymer solution at 3 kPa osmotic pressure. The color gradient represents increasing normalized DoS, from 0.4 to 1.0.

In contrast to swelling in PBS, the hydrogels get iso-tropically compressed when immersed in polymer solutions of known osmotic pressures. The vitreous replacements were assumed to be subjected to a maximum compression at 3 kPa [94]. The two-component hydrogel de-swelled with normalized DoS < 1 when immersed in PVP solutions at 3 kPa osmotic pressure (Figure 3.12). In the presence of an external compressive load, the hydrogels de-swells when their internal swelling pressure was less than the external compressive load. From the

statistical design of experiments, the concentrations of both the poly(MAM-co-MAA-co-BMAC) ($p < 0.01$), and the fibrillary thiolated gellan ($p < 0.05$) were significant in controlling the degree of de-swelling of the two-component hydrogels. Equation 15 predicts the normalized DoS of the hydrogels in polymeric solutions at 3kPa osmotic pressure.

$$\textit{Normalized DoS} = 0.22 + 0.10 \times [G] + 0.04 \times [CoP], \quad [\text{Equation 15}]$$

where 0.223 is the intercept for the defined concentration ranges of [G] and [CoP]. To conclude, both components offer compressive resistance against an external load and potentially mimic the physiological functions of the native vitreous, such as dampening ocular motion and protecting the eye against injury.

3.2.4 Osmotic Swelling Characteristics of the Native Vitreous

The role of the vitreous in generating osmotic swelling pressure remains poorly understood. Experimental techniques to predict the swelling pressure lack due to the fragile biopolymer network of the native vitreous. In light of our findings on the behavior of biomimetic vitreous substitutes, we feel it is reasonable to predict the swelling behavior of the native vitreous. We propose that the native vitreous exhibits controlled Donnan swelling behavior, similar to the biomimetic substitute. The native vitreous, due to its hydrophilic composition and ionic HA, swells in the presence of physiological fluids [3, 27]. The swelling force of HA is counter-balanced by the rigid elastic collagen fibers, resulting in a tightly swollen vitreous gel.

According to the Flory-Rehner theory [95], the pressure generated by the swelling HA (π_{HA}) is the summation of three main components: (1) Osmotic pressure due to the biopolymer-solvent mixing in the vitreous gel (π_{os}), (2) Elastic pressure due to deformation of network chains

into an elongated state during swelling (π_{el}), and (3) Ionic pressure induced by non-uniform distribution of mobile ions between the vitreous gel and the external solution (π_{ion}).

$$\pi_{HA} = \pi_{os, HA} + \pi_{el, HA} + \pi_{ion, HA} \quad [\text{Equation 16}]$$

The ionic pressure generated due to Gibbs-Donnan effect is positive and favors swelling. The osmotic pressure for a polyelectrolyte gel-like HA is also positive and depends on the polymer volume fraction and the polymer-solvent interaction parameter. In contrast, the elastic pressure is negative in magnitude and restricts swelling. Due to the dominating positive force that favors swelling, HA has a high swelling capacity. This is congruous with our observations on the ionic thiolated poly[methacrylamide-co-(methacrylic acid)] where its degree of swelling was high (normalized DoS ≈ 2 ; Figure 3.10).

On the other hand, collagen forms a minimally-swellaable network in physiological fluids. Lloyd et al. showed that fresh collagen fibrils from ox-hides swell minimally, retaining their constant dimensions, in solutions (HCl/ NaOH) with pH ranging between 5.5 to 9.0 [96]. Therefore, in physiological solutions of neutral pH, the net swelling pressure produced by the collagen fibrils are most likely a minimal positive value; a negative swelling pressure would be indicated by shrinkage in the volume of collagen fibrils. This observation is in agreement with our findings on gellan, where the degrees of swelling of thiolated gellan fibrils at neutral pH were minimal (normalized DoS ≈ 1 , Figure 3.10) and not negative.

The native vitreous comprises of the swelling HA and the rigid minimally-swellaable collagen fibrils. The net swelling pressure produced by the vitreous is perhaps given by,

$$\pi_{vitreous} = \pi_{HA} + \pi_{COL} \quad [\text{Equation 17}]$$

$$\pi_{swell, vitreous} = \pi_{os, COL} + \pi_{os, HA} + \pi_{el, COL} + \pi_{el, HA} + \pi_{ion, COL} + \pi_{ion, HA} \quad [\text{Equation 18}]$$

Here, the swelling force is due to the net ($\pi_{os} + \pi_{ion}$), which is counter-balanced by the restraining/compressive force primarily contributed by the π_{el} of collagen fibrils, resulting in a tightly swollen vitreous gel. Furthermore, the swelling pressure (π_{swell}) produced by the vitreous gel may play a central role in (1) Stimulating the growth and development of the eye and (2) Securing the retina in position. The vitreous swelling hypothesis is also consistent with observations of other investigators. Halfter et al. [28] disrupted the vitreous body and the inner limiting membrane (ILM) of chick embryos with collagenase and observed an enlargement (predominantly axial) in the eye size. They also speculated that the cortical vitreous body and ILM of the retina provided the mechanical strength to withstand the pressure emanating from the core or the central vitreous that is relatively rich in hyaluronic acid, during scleral development. The pressure within the vitreous cavity may originate from the Donnan swelling pressure ($\pi_{vitreous}$), as given in Equation (18). When collagen is disrupted, the restraining elastic pressure of collagen ($\pi_{el,COL}$) approaches zero, and $\pi_{swell, vitreous}$ increases due to the high $\pi_{ionic, HA}$. The ionic HA in the vitreous forms a highly swellable network that increases the weight of the vitreous body and the size of the eye-orbit. Excess or inadequate swelling pressure of the vitreous in infants may alter the development of the eye, resulting in myopia or hyperopia, respectively. However, as the eye reaches adult size, we believe that the vitreous continues to exert a non-zero osmotic Donnan swelling pressure, which is capable of holding the retina against the posterior wall of the eye but may not affect the growth of the eye. This hypothesis is congruous with the suggestion of Nickerson et al. [27] that the hydrostatic force exerted by the swelling HA approaches equilibrium against the tension from the collagen fibrils. Furthermore, the interplay between a rigid component (collagen) and a semi-flexible component (HA) in

vitreous swelling seems universal in biological hydrogels, for example, articular cartilage [97, 98], the nucleus pulposus [88], and the corneal stroma [99].

3.2.5 Optimization of Hydrogels

Design-expert software was used to numerically optimize the hydrogel formulations for a transition temperature between 38 to 41 °C and storage moduli between 100 to 200 Pa. A transition temperature slightly above the physiological temperature enables the injection as a polymeric solution, without causing heat-related trauma to the eye.

The mechanical properties of the vitreous have been investigated by various groups, as reviewed in detail by Swindle et al. [25]. The storage modulus of porcine vitreous is 10 ± 1.9 Pa, and that of bovine vitreous is 32 ± 12 Pa [100]. However, the architecture of the natural vitreous changes when removed from the vitreous cavity, which suggests that these values are lower than those found *in vivo*. Furthermore, according to Zimberlin et al. [24], the G' of bovine vitreous *ex vivo* with an intact membrane is 120 Pa. The G' of the hydrogel is critical in withstanding the saccadic movements of the eye; a quick movement of both eyes can vary from a small amplitude with a frequency of 10 °/s to a large amplitude with a frequency of 300 °/s [101]. Measuring the G' at high frequency mimics rapid eye movements. The G' of soft hydrogels, such as 0.5G_5CoP or 0.5G_10CoP, drops to 0 Pa at frequencies above 6.33 Hz, which implies that the polymeric material behaves like a liquid at high frequency, possibly causing a slippage between the retinal cells and the polymer. Hence, to avoid damage from impact and act as a shock absorber, storage moduli higher than 100 Pa are desirable in a vitreous substitute.

Consequently, three optimal formulations of two-component hydrogel for specified T_{gel} and swollen storage moduli were chosen for further study. The formulations were 1.5G_5CoP, 0.9G_12 CoP, and 1.5G_10CoP. Table 3.2 summarizes the sol-gel transition temperature,

rheology, and physical characteristics of the optimal formulations. All of the hydrogels were transparent to visible light, with densities and refractive indexes similar to those of the natural vitreous. These formulations were further tested for *in vitro* biocompatibility and cell proliferation assay (Chapter 4). Of the three formulations, hydrogels with [CoP] \geq 10 mg/mL produced considerable degree of swelling (DoS > 1.4). Hence, two hydrogels – 0.9G_12CoP and 1.5G_10CoP – were chosen for further evaluations, such as osmotic pressure produced by the hydrogels, oxygen transport through them, and their biocompatibility in rabbit eyes.

Table 3.2: Rheological and physical properties of three RSM optimized formulations of the two-component hydrogel.

Formulation	G Conc. [mg/mL]	CoP Conc. [mg/mL]	Sol-gel Transn. Temp. [°C]	Swollen Storage Modulus at 1 Hz [Pa]	Swollen Loss Modulus at 1 Hz [Pa]	Norm. Degree of Swelling in 1XPBS	Refrac. Index	Density	Average Light Transm. (%)
1.5G_5CoP	1.5	5	39.75	144.5	7.91	1.32	1.3351	1.009	93.6
0.9G_12CoP	0.9	12	40.2	151	4.73	1.53	1.3355	1.003	94
1.5G_10CoP	1.5	10	41.5	178	7.48	1.52	1.3372	1.006	87.6

3.2.5 Osmotic Swelling Pressure Produced by the Two Optimized Hydrogels

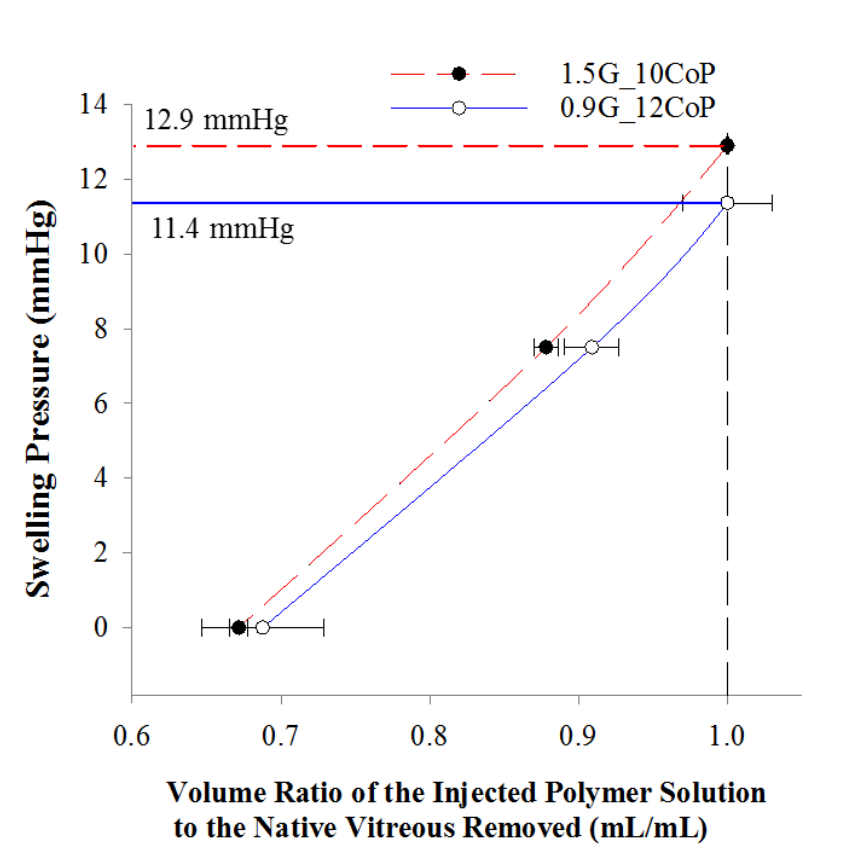


Figure 3.13: Swelling pressure produced by two optimized hydrogel formulations ($n = 5$ each) for varying ratios of injected polymer solution volume vs. volume of the native vitreous removed from the eye.

The osmotic swelling pressure produced by the hydrogel is the driving mechanism for retinal tamponade. Furthermore, the swelling pressure produced by the hydrogel was found to vary by tailoring the volumetric ratio of the polymer solution injected into the vitreous cavity to the volume native vitreous removed. For a constant hydrogel composition, the volumetric ratio is directly related to the final polymer concentration of the hydrogel, which decreases upon swelling in contact with a physiological solution. At a volumetric ratio equivalent to 1, the two hydrogels, 0.9G_12CoP, and 1.5G_10CoP, produced swelling pressures of 1.61 and 1.77 kPa (12.1 and 13.3 mmHg) respectively. When the volumetric ratio was less than 1, the *in situ*-

formed hydrogel swelled, decreasing the final polymer concentration of the gel and consequently decreasing the swelling pressure (Figure 3.13). This relationship provides the precise volume of injected vitreous substitute needed to produce appropriate osmotic swelling pressure for treating retinal detachments in people of diverse age groups.

3.2.6 Oxygen Transport through the Two Optimized Hydrogels

The partial pressure of oxygen (pO_2) in the de-oxygenated medium was measured over time at a fixed displacement from the saturation concentration (Figure 3.2), using the fiber optic oxygen sensor. The experimental variables that may affect the measured pO_2 results are (1) Temperature, (2) Dissolved oxygen concentration in the solvent, (3) Diffusing medium, (4) Displacement of the measuring point from the oxygen saturated solvent, and (5) Permeability of the semi-permeable membrane. The entire diffusion cell set-up, the solvent reservoir, and the oxygen probe were placed in a temperature-controlled oven to minimize the temperature fluctuation in the diffusing medium (Figure 3.2). Also, an oxygen probe with a temperature sensor was used to monitor the temperature of the diffusing medium for a few experiments. During the initial set-up, the temperature of the diffusing medium was slightly lower than the desired temperature, which then equilibrated to the desired temperature within 30 mins. The average temperature fluctuations were in the range between 1.1-1.8 °C. The solvent reservoir was continuously bubbled with air throughout the experiment, and saturated with oxygen. The partial pressure of the solvent was measured using an oxygen probe to confirm the oxygen saturation. The sample medium was carefully placed in the mid-chamber or the sample chamber without an air-bubble, thereby minimizing variations in the diffusivity results. The oxygen probe was inserted at a fixed displacement of 0.01 m from the semi-permeable membrane that separated the top- and mid-chamber. The flatness of the semi-permeable membrane was also

checked for minimizing variations in displacement of the measuring point. Furthermore, the dialysis membrane was a thin, porous material, whose MWCO was nearly 1000 times greater than the MW of oxygen molecule. The membrane does offer resistance to diffusion of gas across them, however, was assumed to be negligible for our experiments. Dowse et al. [102] estimated the resistance to diffusion of oxygen across the semi-permeable membrane, and concluded that the material offers the path of least resistance and also, any capacitance can be safely ignored. By employing the above methods, the errors in the diffusivity results due to the change in the experimental variables were controlled.

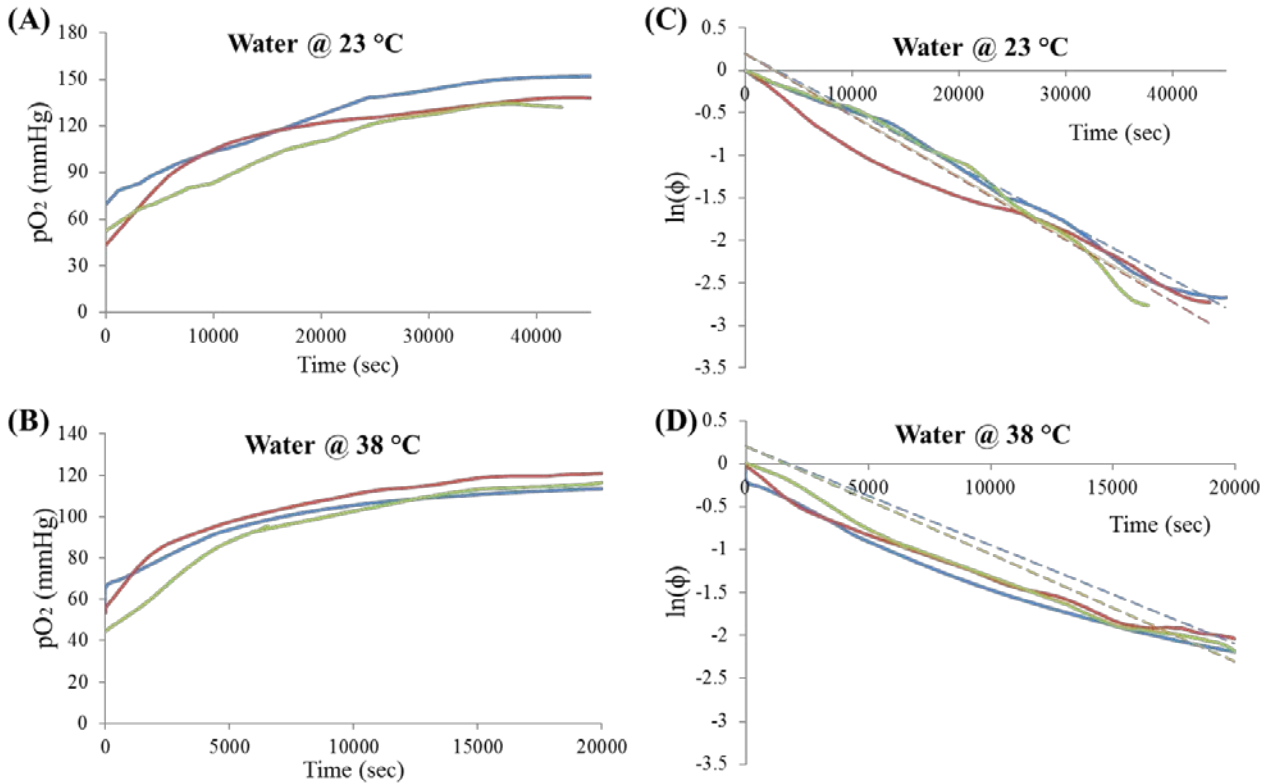


Figure 3.14: Oxygen level in water at 23 °C (A, C), and at 38 °C (B, D) over time. (A, B) represent the partial pressure of oxygen measured over time. (C, D) represent the logarithmic conversion of dimensionless oxygen concentration over time. In all the plots, the experimental data is given in solid line (different colors represent the replicates), and the linear fit in C, D is represented in dashed line.

The experimental data (pO_2) increases exponentially over time till it reaches saturation as shown in Figure 3.14A, C. The pO_2 is then converted to the logarithmic domain, and then fitted to the analytical solution for the Fick's second law to obtain the oxygen diffusivity values (Figure 3.14 C, D). Figure 3.14 shows the concentration of oxygen over time for water at 23 °C and 38 °C. The average goodness of the fit was 0.95 ± 0.04 for water at 23 °C, and 0.76 ± 0.03 at 38 °C. The diffusivity of oxygen in water was found to be $2.9 \pm 0.1 \text{ E-}09 \text{ m}^2/\text{s}$ at 23 °C and $4.7 \pm 0.2 \text{ E-}09 \text{ m}^2/\text{s}$ at 38 °C. The diffusivity values were slightly greater than the range of values estimated by various investigators, such as Bhunia et al. [103] ($2.2 \pm 0.1 \text{ E-}09 \text{ m}^2/\text{s}$ at 22 °C), Penicaud et al. [104] ($2.5 \pm 0.07 \text{ E-}09 \text{ m}^2/\text{s}$ at 20 °C), and Wise et al. [105] ($3.9 \text{ E-}09 \text{ m}^2/\text{s}$ at 40 °C); however, there was no significant difference between the experimental and literature values at both the temperatures.

As expected, the temperature had a pronounced influence on the oxygen diffusivity. The oxygen diffusion increased significantly ($p = 0.0012$) with an increase in temperature from 23 °C to 38 °C. Also, the partial pressure of oxygen at saturation decreased from $147 \pm 8 \text{ mmHg}$ to $125 \pm 4 \text{ mmHg}$, correspondingly the solubility of oxygen in water, calculated using Henry's law, decreased from $8.4 \pm 0.3 \text{ mg/L}$ to $5.4 \pm 0.2 \text{ mg/L}$ for an increase in temperature from 23 °C to 38 °C, respectively. This is because, with increase in temperature, the kinetic energy increases, consequently the motion of gas molecules increases, which results in breaking of intermolecular bonds, thereby letting the gas molecules to escape from the solution.

In a solid state diffusion, energy is required by an atom to jump to the next neighboring vacant position, and the energy required for migration is referred to as activation energy [106]. The activation energy for migration is usually produced by thermal vibrations. Similarly, in gas-

liquid diffusion, the energy required by the gas molecules to diffuse through the medium is given based on the Arrhenius-type equation, which is defined as:

$$D_{O_2} = D_0 \exp\left(\frac{-E_a}{RT}\right), \quad [\text{Equation 19}]$$

where D_0 is the pre-exponential factor, E_a is the activation energy for molecular diffusion, T is the absolute temperature (K), and R is the universal gas constant (8.314 J/ (mol.K)). The activation energy of diffusion of oxygen molecules in water was 23.6 ± 0.7 kJ/mol, which was slightly greater than those predicted by Bhunia et al. ($E_a = 21.4$ kJ/mol) [103]. Therefore, it is conclusive that the experimental method is applicable for obtaining the oxygen diffusivity in the current vitreous substitutes (BSS and SO; controls), and the two-component hydrogels (0.9G_12CoP and 1.5G_10CoP).

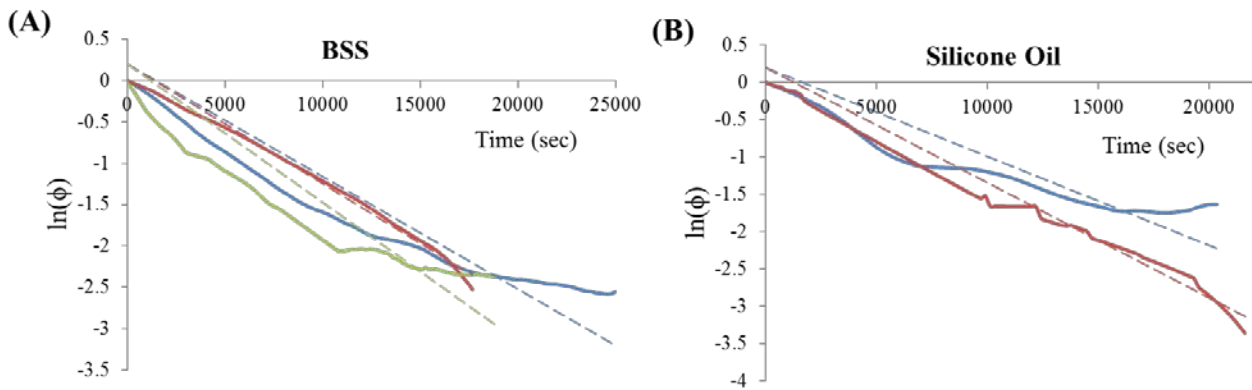


Figure 3.15: Oxygen concentration of the experimental controls over time. The logarithmic form of dimensionless oxygen concentration decreases linearly over time. Solid lines indicate the experimental data (different colors represent the number of replicates), and dashed lines represent the fit.

Both the controls (BSS and SO) and the experimental groups (0.9G_12CoP and 1.5G_10CoP) were measured at 38 °C. At a fixed displacement, the oxygen concentration (measured as pO_2) in the controls and the experimental groups increased exponentially over time

until it reached saturation. The oxygen concentration was then converted to its dimensionless form, which is calculated as $\phi = \frac{C - C_s}{C_i - C_s}$; C_s is the saturation concentration, which is assumed to be the maximum concentration; and C_i is the initial oxygen concentration, which is assumed as the minimum concentration in the experimental data. Because the saturation concentration is greater than the initial concentration, the dimensionless concentration decreases over time (Figure 3.15 and Figure 3.16).

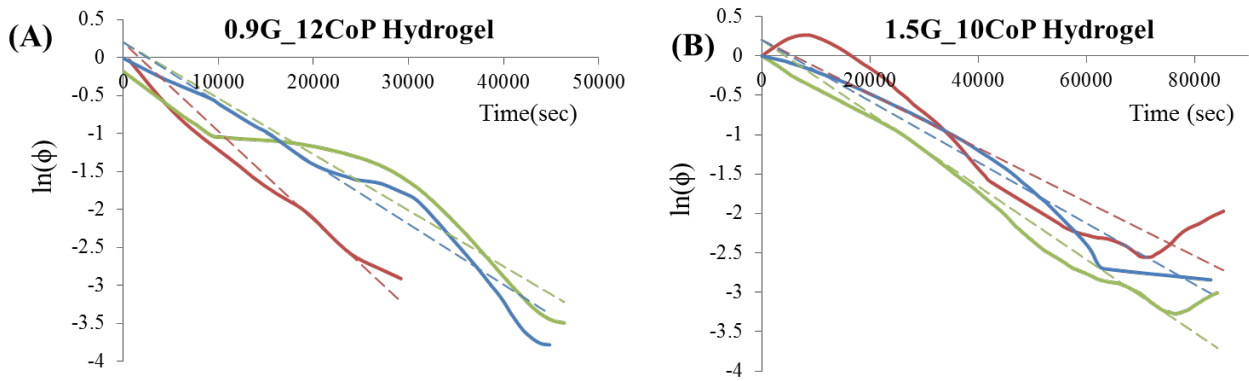


Figure 3.16: Logarithmic form of the dimensionless oxygen concentration of hydrogel samples over time. (A) 0.9G_12CoP hydrogel (B) 1.5G_10CoP hydrogel. Experimental data for different repeats are given in solid lines of different colors, and the linear curve fits are represented in dashed line.

The logarithmic conversion to the dimensionless oxygen concentration resulted in a linear plot over time. The number of repeats for each medium was 3; except silicone oil, where $n=2$. Due to some unknown reason, the oxygen probe broke during each measurement for silicone oil. Each plot fits the analytical solution for the Fick's second law, given in equation 11. The average goodness of fit was 0.84-0.86 for controls, BSS and SO, and 0.92-0.95 for hydrogels. The medium's oxygen diffusion coefficient was calculated from the slope of the fit.

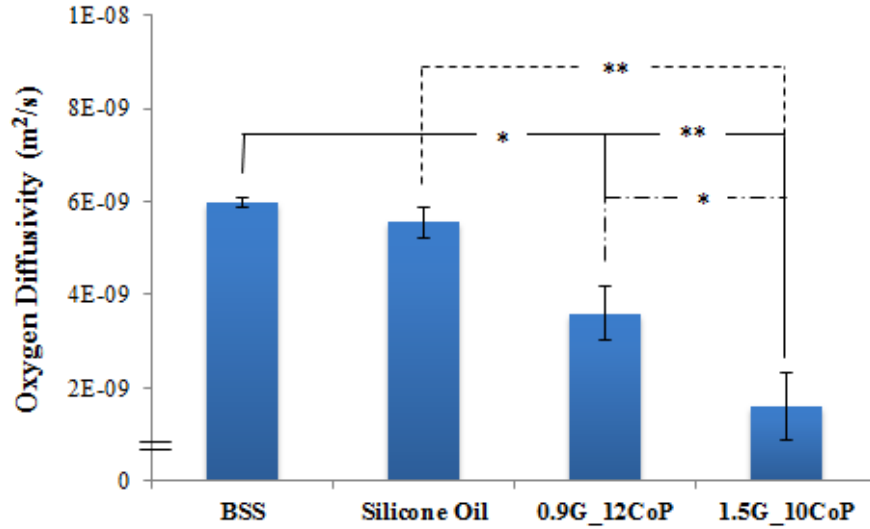


Figure 3.17: Oxygen diffusion coefficient in controls and hydrogels. All the other mediums are measured at 38 °C. Data represent Mean diffusivity, and error bars indicate the standard deviation. The significant difference between the values, with $p < 0.05$ is represented as (*) and $p < 0.01$ as (**).

Figure 3.17 shows the oxygen diffusion coefficient (D_{O_2}) of the controls and the experimental groups. There is no significant difference ($p=0.60$) in D_{O_2} between each of the controls (current vitreous substitutes) – BSS and Silicone oil. When the de-oxygenated BSS is separated from the oxygen saturated PBS (isotonic), there exists an oxygen concentration gradient across the chambers, and therefore the oxygen from higher concentration zone diffuses towards the lower concentration zone until it reaches equilibrium. Evans et al. reported the D_{O_2} of physiological saline to be $2.1E-09 \text{ m}^2/\text{s}$ at 22 °C. According to the Stokes-Einstein's equation, the diffusivity depends on viscosity and temperature as given below:

$$\frac{D_1 \eta_1}{T_1} = \frac{D_2 \eta_2}{T_2}, \quad \text{[Equation 20]}$$

where η is dynamic viscosity, and T is the temperature. Applying the temperature conversion for the diffusivity reported by Evans et al., the D_{O_2} of physiological saline is estimated to be $5.8E-09 \text{ m}^2/\text{s}$ at 38 °C. This literature value is comparable to our experimental diffusivity value (6.0 ± 0.5

E-09 m²/s). On the other hand, silicone oil is a uniform hydrophobic medium. The diffusion of lipid-soluble molecule, like oxygen, in silicone oil is primarily governed by its solubility in the medium. Poncelet et al. [107] showed that the oxygen solubility in silicone oil is approximately 20-fold higher than that of the oxygen solubility in water. Therefore, as expected, higher oxygen diffusivity in silicone oil than water was observed in our experiments.

The oxygen diffusivity in the hydrogels was significantly lower than both the controls (BSS and SO) (Figure 3.17). The oxygen diffusion coefficients in hydrogels of formulations 0.9G_12CoP and 1.5G_10CoP were approximately 2 and 4 times respectively lower than the controls, indicating that the oxygen diffuses at a slower rate in the hydrogels. This is because, unlike the controls that have a uniform liquid phase, hydrogels form a heterogeneous porous medium. The polymeric chains make the medium structurally rigid. The oxygen diffuses through a tortuous path created by polymeric chains, thereby slowing down the effective diffusion process. Furthermore, among the two hydrogels, oxygen diffusivity in 1.5G_10CoP was twice lower than the 0.9G_12CoP. Compan et al. [108] demonstrated that the diffusivity of oxygen through a methacrylate-based hydrogel increases with an increase in water content (swelling), which in turn depends on the composition of the polymeric gel. Their observations are congruous with our experimental results, where the 0.9G_12CoP has a higher D_{O_2} than 1.5G_10CoP, because of its slightly higher degree of swelling in 0.9G_12CoP than that of the 1.5G_10CoP.

Several theories, such as free volume theory, hydrodynamic theory, obstruction theory, and combined hydrodynamic and obstruction effects, have been proposed to understand the diffusion process through the hydrogels. Amsden et al. [109] neatly summarized the solute diffusion with hydrogels. Of all the theories, obstruction theory is applicable to our gels

because it assumes that the path length for solute diffusion through the medium increases in the presence of impenetrable polymer chains. Ogston et al. [110] took a phenomenological approach to predict the oxygen diffusivity through the hydrogel. They considered hydrogel as a crosslinked polymer made of a random network of straight, long fibers of negligible width, and considered solute to be a hard sphere. The solute was assumed to diffuse through a succession of random unit steps in hydrogel. The diffusion does not occur if the solute encounters a polymer chain. They expressed the diffusion coefficient in the gel compared to water as given below:

$$\frac{D_{O2g}}{D_{O2w}} = \exp \left[-\sqrt{\phi} \frac{r_f + r_s}{r_f} \right] \quad \text{[Equation 21]}$$

where ϕ is the polymer volume fraction within the gel, r_f is the radius of the fiber, and r_s is the solute hydrodynamic radius; D_{O2w} is the oxygen diffusivity in water at 38 °C, which is assumed to be 4E-9 m²/s. Although conceptually appealing, the Ogston model is applicable only for a dilute or semi-dilute system of small molecules. The D_{O2} of our two-component hydrogels, 0.9G_12CoP and 1.5G_10CoP, predicted using this model was 3.65E-9 and 3.67E-9 m²/s, respectively. The model was in good agreement with the experimental diffusivity value for 0.9G_12CoP hydrogel; however, had >50% deviation from the experimental determined 1.5G_10CoP hydrogel. This is because most of the theories, including hydrodynamic, obstruction, and combinations, assumes polymer chains as rigid chains, and fail to account for the diffusion in composite systems. The two-component hydrogels have unique variation in structural composition, which comprises of a rigid-rod like fibrils interspersed with semi-flexible copolymer network. To understand the effect of structural variations in polymeric chains on the diffusivity of solutes through them, more experiments with different formulations of the two-component hydrogels are needed.

3.3 Conclusions

Biocompatible hydrogels with tailored biomimetic properties and functions of the native vitreous are an ideal vitreous substitute. Inspired by the native vitreous, we developed a two-component hydrogel with a fibrillary thiolated gellan and a semi-flexible poly(MAM-co-MAA-co-BMAC). The optical transparencies, refractive indexes, and densities of the two-component hydrogels are close to those of the native vitreous. In addition, the hydrogels have the ability to undergo temperature-triggered physical gelation instantaneously near physiological temperature. The physical gelation, combined with chemical gelation (thiol cross-linking) endows the hydrogels with the *in situ*-forming ability. The hydrogels were viscoelastic solid, and swells in a physiological fluid, producing an osmotic swelling pressure. The mechanical property, transition temperature, and extent of swelling of the two-component hydrogels can be adjusted by changing the concentration of each component. Although both the components are significant in controlling the properties, the concentration of the thiolated gellan is statistically more significant than that of the copolymer in controlling the storage modulus and transition temperature, while the concentration of copolymer is critical in governing the extent of swelling in physiological solution. In the light of findings on the swelling behavior of the bio-mimetic hydrogel, we propose that the native vitreous exhibits controlled swelling behavior. The swelling force exerted by the ionic HA is perhaps counterbalanced by the stiff collagen scaffold, resulting in a tightly swollen vitreous gel that produces osmotic swelling pressure. Two hydrogels formulations – 0.9G_12 CoP and 1.5G_10CoP – that most closely match the properties of the native vitreous were further evaluated. The hydrogels 0.9G_12CoP and 1.5G_10CoP produced swelling pressures of 11.4 and 12.9 mmHg respectively when injected into the vitreous cavity. The oxygen diffusivity through the hydrogels was significantly lower

than current substitutes, such as BSS and Silicone oil, as expected. The two hydrogels are recommended for further biocompatibility evaluations in animal models.

Chapter 4: Biocompatibility of the Two-Component Hydrogels

We evaluated the biocompatibility of the individual components of the two-component hydrogel at different concentrations, and optimized three formulations of *in-situ* forming hydrogels, 1.5G_5CoP, 0.9G_12CoP, and 1.5G_10CoP. These are all potentially biocompatible, have sol-gel transitions near physiological temperature, and have optical, physical, and mechanical properties close to those of the native vitreous. This chapter describes the biocompatibility and degradation assessments performed on these hydrogels in contact with various cell lines. The two best performing hydrogels, 0.9G_12CoP and 1.5G_10CoP, were further investigated for their biocompatibility in rabbit models. Part of the work described in the chapter uses materials from the reference [77] and the manuscript submitted to the Journal of Biomaterials [111].

4.1 Materials and Methods

4.1.1 Materials

Dulbecco's modified Eagles' medium/Nutrient Mixture F-12 Ham was purchased from Thermo Fisher Scientific (Great Island, NY). Glycine (tissue culture grade) and ethylenediaminetetraacetic acid disodium salt (EDTA, electrophoresis grade) were purchased from Fisher Scientific (Pittsburg, PA). Gentamicin and amphotericin were purchased from Sigma Aldrich Co. (St. Louis, MO). Human retinal pigment epithelial cells (ARPE-19) and fibroblast cells (3T3/NIH) cell lines were purchased from American Type Culture Collection (Manassas, VA). Rat retinal Müller cells (rMC-1), an immortalized cell line established by Vijay et al. [112], were graciously given to us by Dr. Rithwick Rajagopal, Department of

Ophthalmology and Visual Sciences at the Washington University School of Medicine. Dutch-Belted male rabbits were purchased from Myrtle's Rabbitry/Covance Research Products Inc. (Denver, PA) and silicone oil 5000 (SO) was from Bausch and Lomb Incorporated (Rochester, NY). The drugs and supplies for animal surgery were purchased from the Division of Comparative Medicine Pharmacy, Washington University School of Medicine (St. Louis, MO).

4.1.2 Isolation of Primary Porcine Retinal Pigment Epithelial Cells

The procedures for extraction and passaging of primary porcine retinal pigment epithelial (ppRPE) cells were similar to the protocol described by Toops et al. [113], with few modifications. The procured disinfected eye cups of pig eyes, after removal of the vitreous and retina, were incubated with 2 mL of 2X Trypsin with 5.3 mM EDTA in Hank's Balanced Salt Solution (HBSS) without Ca^{2+} and Mg^{2+} for 90 minutes. Cells were collected as per the Toops protocol and plated at a density between 3000 to 4000 cells/cm². ppRPE cells were used at the first or second passage for biocompatibility assessments.

4.1.3 Growth of Cell Lines

The growth rate of cells was studied using a real-time, label-free, impedance-based method—Electric Cell-substrate Impedance Sensing (ECIS®) (Applied BioPhysics, Troy, NY). The gold electrodes of the ECIS 96-well plate were pre-treated by incubating each well with 100 µL of 10 mM sterile cysteine for 15 mins. The wells were then rinsed twice with 150 µL sterile double-distilled water. To coat proteins on the gold electrodes, Dulbecco's modified Eagles' medium/Nutrient Mixture F-12 Ham with 10% fetal calf serum (FCS), 1X penicillin/streptomycin 1X gentamicin, and 0.1X amphotericin (DMEM/F12) was added to the wells and the resistance across the electrodes was recorded. About 150 µL of the ppRPE cells

(n=8 each) in DMEM/F12 media were plated on the ECIS 96-well plate at increasing cell densities from 2,000 cells/well to 40,000 cells/well. rMC-1 cells (n=8) from 1,000 to 20,000 cells/well. The cells were left undisturbed at room temperature for 30 minutes to allow cells to adhere to the bottom of the wells, avoiding convection currents and uneven cell distribution. Next, the 96-well plate was connected to the ECIS, and the resistance offered by the cells during their growth and subsequent attachment to the plate was continuously measured at different frequencies from 400 Hz to 64,000 Hz against time. DMEM/F12 medium was changed every 3 days to maintain consistent growth. The experiment was terminated when the cells reached confluence and the measured resistance saturated.

4.1.4 Hydrogel Preparation

Thiolated gellan (synthesized as described in chapter 2) was dissolved at 2X the concentrations of the final formulations (0.5 mg/mL, 1.0 mg/mL, and 1.5 mg/mL) in sterile nitrogen (N₂) bubbled water, and the pH of the solution was adjusted to 7.4. The thiolated gellan solution and sterile 2X DMEM/F12 media were then heated separately at 45 °C for 15 minutes and mixed immediately prior to being cast over ARPE-19 cells and ppRPE cells.

To make composite hydrogels, thiolated gellan was dissolved in sterile nitrogen (N₂) bubbled water, and poly(MAM-co-MAA-co-BMAC) (synthesized as described in chapter 1) was dissolved in sterile 2X DMEM/F12 media. Both components were dissolved at 2X the concentration of the desired final formulations and the pH of both solutions was adjusted to 7.4. The thiolated gellan and poly(MAM-co-MAA-co-BMAC) solutions were then heated separately at 45 °C for 15 minutes and mixed immediately prior to application to the cells.

4.1.5 *In Vitro* Biocompatibility Tests

Biocompatibility Evaluations using ECIS

The biocompatibility of the thiolated gellan hydrogels was tested using an ECIS. ARPE-19 and ppRPE cells were plated at densities of 20,000 and 40,000 cells/well, respectively. A day later, after the cells had attached to the electrodes, the thiolated gellan solution was cast over the cells. The resistance across the electrodes was measured continuously over time at 4000 Hz. The cytotoxicity was interpreted as the decrease in resistance with respect to the control, cells without hydrogel. The DMEM/F-12 medium was exchanged on day 3, and the experiment was terminated on day 6, after the initial addition of polymer solution.

To evaluate the biocompatibility of the two-component hydrogels, two sets of experiments were performed. First, to determine the biocompatibility of a confluent layer of cells in contact with hydrogel, the cells were plated at high densities: 40,000 cells/well for ppRPE, 20,000 cells/well for ARPE-19, and 10,000 cells/well for rMC-1 and 3T3/NIH cells. Prior to addition of two-component polymer solution, ppRPE, ARPE-19, and rMC-1 cells were kept in culture for seven, seven, and three days respectively to allow complete formation of tight junctions, while the 3T3/NIH fibroblasts were cultured for one day. Due to the lack of contact inhibition in 3T3 cells, confluency was not reached until the end of the experiment. Cytotoxicity was interpreted as the decrease in resistance with respect to the control and the effects on tight cell junctions were shown by changes in barrier resistance. These two characteristics were observed at an optimal frequency of 4,000 Hz for six days after addition of polymer solution to ARPE-19, ppRPE, and 3T3/NIH cells, and for three days in the case of the rMC-1 cell line. In the second assay, the cells were plated at low densities (ppRPE at 10,000 cells/well, ARPE-19 at 5,000 cells/well, and 3T3/NIH at 4,000 cells /well), and the polymer solution was added the

following day to investigate the proliferation of cells in the presence of gel. Simultaneously, the cell morphology was imaged using bright-field microscopy on the 4th, 7th, and 11th days after the addition of polymer solution. Note that the cell plating densities and the experimental timing were same as for the ECIS biocompatibility experiment.

Biocompatibility Evaluations using MTT

MTT assay was performed to evaluate the biocompatibility of the hydrogels in contact with rMC-1 cells. Simultaneous to the ECIS experiment, the rMC-1 of 10,000 cells/well (n=4) was plated in a 96-well plate for MTT assay. The cell plating densities and the experimental timing were same as for the ECIS biocompatibility experiment. After 72 and 120 hours of hydrogel addition at confluence conditions, the cells were incubated with 100 μ L 3-(4,5-Dimethylthiazol-2-Yl)-2,5-Diphenyltetrazolium Bromide (MTT) of concentration 1mg/mL for 5 hours. The media with the hydrogel was then removed, and the MTT dye on the cell layer was dissolved with Dimethyl sulfoxide (DMSO). The absorbance of the samples was measured at 540 nm in a UV-Vis spectrophotometer.

Cell Count Analysis

To evaluate the final number of cells, the rMC-1 in 96 well-plate (n=3) was lifted by incubation in 100 μ L of trypsin for 10 mins followed by the addition of 100 μ L of fresh media. The media with cells were centrifuged at 750 rpm for 5 mins. The supernatant was discarded, and the sediment cells were re-diluted with 500 μ L media. About 10 μ L of cell sample was mixed with 10 μ L of trypan-blue, and the number of cells in 10 μ L of final solution was counted using a hemocytometer under the microscope.

4.1.6 Degradation Studies

Two degradation studies of the hydrogel were carried out *in vitro* by incubating the gel in 1X PBS containing either (i) 10,000 U/mL of lysozyme or (ii) 1,000 U/mL of trypsin, at 37°C for 4 weeks. Two mL of either lysozyme or trypsin solution was added to pre-weighed 35 mm dishes containing hydrogel formulations of (a) 0.9G_12CoP and (b) 1.5G_10CoP. At predetermined time intervals, the gel was patted dry and weighed. The percent degradation was determined by

$$\text{Percent Mass Loss} = \left(\frac{W_0 - W_t}{W_0} \right) * 100 \quad \text{[Equation 22]}$$

where W_0 is the initial weight of the hydrogel, and W_t is the weight of the gel at time t (days).

We also tested the 1.5G_10CoP hydrogel in contact with primary porcine retinal pigment epithelial (ppRPE) cells for 30 days. The ppRPE cells were grown on the apical side of microporous collagen-coated millicell-CM insert membranes (0.4 μ M). Two mL of the polymer solution was pipetted into each cell of a six-well tissue culture tray, incubated at 37 °C for three days to fully gel, then allowed to swell in DMEM/F12 medium for seven days. The insert membranes containing the ppRPE cells were then placed over the hydrogel and incubated in DMEM/F12 medium for 30 days. Every 3-4 days, media from the apical side of the cultured cells on the membrane was transferred to the basolateral side containing the gel, to allow any enzymes on the apical side of the epithelial cells to come into contact with the hydrogel. The goal was to accurately represent the enzymes that the hydrogel may come in contact with inside the eye. Hydrogels that were not in contact with cells were the controls. The rheology of the composite hydrogel (n=3) after 30 days in contact with cells was measured using a plate-plate shear rheometer, as described in chapter 3. The cells were fixed using 4% formaldehyde, stained

for nucleus and actin fibers using (4', 6-diamidino-2-phenylindole dihydrochloride) (DAPI) and phalloidin, and imaged using confocal microscopy.

4.1.7 Animal Preparation and Study Protocol

All studies were performed in accordance with the Association for Research in Vision and Ophthalmology (ARVO) resolution on the use of animals in vision and ophthalmic research. Thirty two Dutch-Belted male rabbits, 5-6 months of age, were used in this experiment. Eleven rabbits (n=11) were investigated for each formulation of hydrogel, 0.9G_12CoP and 1.5G_10CoP, and 10 rabbits with silicone oil 5000 (n=10) (SO) served as the vitreous substitute control. Vitrectomy followed by replacement was performed on the right eye of each animal, while the left eye was the non-surgical eye – referred as a non-surgical control in this paper. We performed detailed ophthalmic examinations by slit lamp and measured intra-ocular pressure (IOP) prior to surgery, and on days 1, 4, 7, and 30 post-operation. Prior to surgery and 30 days after, electroretinogram (ERG) tests were performed on a subset of study rabbits (six were injected with SO, six with 0.9G_12CoP, and eight with 1.5G_10CoP hydrogel). Ocular coherence tomography (OCT) and fundus examinations were performed on a subset of rabbits (n=4 for each experimental group) 30 days after surgery. All rabbits were euthanized after the final examinations, and the eyeballs were removed for histology.

4.1.8 Vitrectomy and Injection of Vitreous Substitute

Dr. Ying-Bo Shui, an experienced vitreoretinal surgeon, performed all surgical procedures. The surgeries were performed under general anesthesia using isoflurane and ketamine. Rabbits were prepped and draped in a standard surgical manner, and their eyes were

dilated and prepped with an antibiotic. While anesthetized, the rabbits underwent a complete ophthalmic examination.

After establishing baseline ocular conditions, a partial two-port pars plana vitrectomy was performed on the right eye of the rabbit. Approximately 0.5 to 0.6 mL of vitreous from the temporal side of the vitreous cavity was removed using a 23 gauge vitrector (Pro Care Plus Vitrectomy System, Vision Care Devices, Redding, CA), followed by a fluid-air exchange, and injection of approximately the same volume of the vitreous substitute as the removed vitreous. Due to the relatively large volume of the lens in the rabbit eye, only a partial vitrectomy could be performed, to avoid touching the lens and forming a cataract. The rabbit vitreous is known for its tight adherence to the retina, rendering complete hyaloid removal unlikely.

4.1.9 Rabbit Pre- and Post-operative Examinations

Slit Lamp

Slit-lamp examinations were performed before surgery and 1, 4, 7, and 30 days post-operation.

Intraocular Pressure

Rabbit eyes were anesthetized with topical 0.5% proparacaine hydrochloride (Alcaine, Alcon-Couvreur, Belgium). IOP was measured using a tonometer (Tono-Pen XL, Nicosia, Cyprus) on the days mentioned in the study protocol.

Funduscopy and Ocular Coherence Tomography

Rabbits were anesthetized by intramuscular administration of 15-20 mg kg⁻¹ ketamine with 2-5 mg kg⁻¹ xylazine and maintained with IV ketamine (5-10 mg kg⁻¹) as needed during the procedure. The rabbit fundus was visualized and imaged with an endoscope camera, and OCT

was performed on both eyes using Leica's Envisu R2210 Spectral domain ophthalmic imaging system (Buffalo Grove, Illinois) to obtain the cross-sectional images (B Scan) of the retina.

Oxygen Tension Measurements

Prior to surgery and 30 days post-surgery, the oxygen tension in the vitreous and the vitreous substitute respectively was measured using an oxygen measuring probe (OxyLab pO₂ E-Series Sensor, Oxford Optronix Ltd., Oxford, U.K.) (Figure 4.1B). The oxyprobe was connected to the OxyLab – Tissue oxygenation monitor, and the computer interface via the LabView® software. The partial pressure of oxygen were measured at the (a) Vitrectomy site, the site where vitrectomy was performed, and the vitreous was replaced with the substitute, and the (b) Intra-vitreous site, the site where vitrectomy was not performed and the vitreous remains intact (Figure 4.1A). Controls were the measurements obtained in the vitreous of the non-surgical eye (left eye).

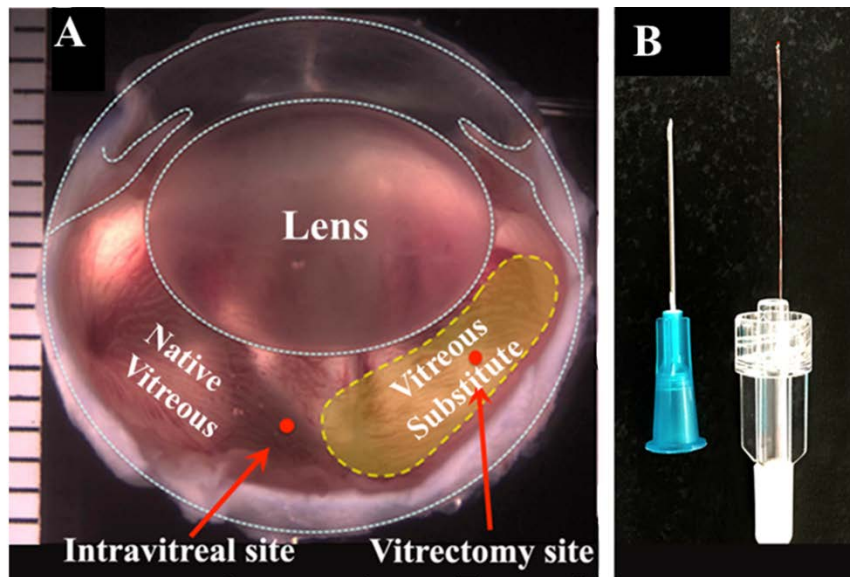


Figure 4.1: (A) Anatomy of the rabbit eye with the sites where the partial pressure of oxygen was measured. (B) Image of the oxygen measuring probe. The probe (extending from the white head) is very thin compared to the 25G needle represented in blue for reference.

Electroretinogram

At least 7 days prior to surgery and 30 days post-surgery, electroretinogram examinations were performed on the study rabbits (n = 6 each for SO and 0.9G_12CoP hydrogel, and n =8 for 1.5G_10CoP hydrogel). Briefly, rabbits were sedated by intramuscular administration of 15-20 mg kg⁻¹ ketamine with 2-5 mg kg⁻¹ xylazine and maintained with IV ketamine (5-10 mg kg⁻¹) as needed during the procedure. Rabbits were maintained at a constant physiologically appropriate body temperature, and vital signs were monitored while the rabbits were sedated. A human ERG-Jet corneal contact lens electrode (Universo SA, La Chaux-de-Fonds, Switzerland) was placed on each eye with 2.5% hypromellose (“Gonak”, Akorn Inc., Lake Forest, IL). A reference needle electrode (The Electrode Store, Inc., Buckley, WA) was placed under the skin between the ears at the vertex of the skull, and a ground electrode was placed subcutaneously on the left flank. The rabbit was positioned with its head inside the Ganzfeld dome of an LKC E3000 Electro-diagnostic system (LKC Technologies, Gaithersburg, MD), and ERG testing was performed in five steps on both eyes.

The rabbit was adapted to a background light intensity of 2.30 log cd m⁻² for 10 minutes and then tested using photopic flash ERG (Step 1). The average response from five flash stimuli of 2.53 cd s m⁻² intensity was obtained. The photopic flicker ERG (Step 2) consisted of an average response from 10 flickering stimuli of the same intensity at 30 Hz, at the same background light level. Next, the rabbit was dark adapted for 20 minutes before scotopic flash ERG was performed (Step 3). The average response from 6 flash stimuli (0.0101 cd s m⁻²) was obtained. After 2 additional minutes of dark adaptation, a mesopic flash ERG (Step 4) was measured from an average of five 2.53 cd s m⁻² flash stimuli presented at intervals of 30.3 ms, and finally (Step 5) oscillatory potentials were averaged from responses of three 2.53 cd s m⁻² flash stimuli. If needed, Yobine® was administered after ERG to assist in the recovery of the

rabbits. In the electroretinography, the a-wave amplitude was measured from the baseline to the trough of the a-wave, and the b-wave amplitude was measured from the bottom of the a-wave to the peak of the b-wave. The analyzed data were used to compare the treated right eye retinal responses post-surgery with their respective pre-surgical activity.

Histology

After 30 days, the rabbits were euthanized, and the eyeballs were excised and fixed in 4% formalin, pH 7.3, in 0.1 M Sørensen's phosphate buffer for 1 hour. The specimens were then washed with 1X PBS twice, sectioned at 12 μ m on a cryostat, and every tenth slide was stained with hematoxylin and eosin (H&E) according to standard procedures. The histopathologic evaluation was conducted by an experienced pathologist from Seventh Wave Laboratories LLC (St. Louis, MO). Tissues were scored from 0 (null) to 4 (severe) for five histopathological criteria: (1) Needle track or suture line through the ora ciliaris (2) Mononuclear cell inflammation in the vitreous (3) Focal rupture of the posterior lens capsule (4) Displacement of the nuclei rods and cones into the inner or outer segment of the photoreceptor layer, and (5) Hemorrhage. Furthermore, representative specimens from each of the study cohorts were additionally reviewed by our university's ophthalmic pathologist, Dr. George J. Harocopos. Bright-field images were captured with a charge-coupled camera attached to a microscope (Olympus BX51, Olympus America, Inc., Melville, NY). The artifacts in the images are due to a delay in the fixation process.

4.1.10 Statistical Analysis

All results are reported as the mean \pm SE (standard error), where error bars denote the SE. The standard error is the standard deviation divided by the square root of the number of repeats for each experimental group. For the ECIS and degradation studies, the F-test was performed to

analyze the variance between the experimental group and the control, followed by a one-tailed t-test (assuming equal or unequal variances, based on the result from the F-test) with an alternative hypothesis of $\text{Mean}(\text{control}) > \text{Mean}(\text{experimental group})$. The experimental group is considered to be toxic to the cells if the t-test is true. For rabbit studies, the experimental groups were the hydrogel formulations 0.9G_12CoP and 1.5G_10CoP, while SO and the non-surgical left eye were controls. The F-test, followed by a two-tailed t-test (assuming equal or unequal variances, based on the result from the F-test) was performed to analyze the variance. A p-value < 0.05 was considered to be statistically significant for all studies.

4.2 Results and Discussion

4.2.1 Growth Curves of Different Cell Lines

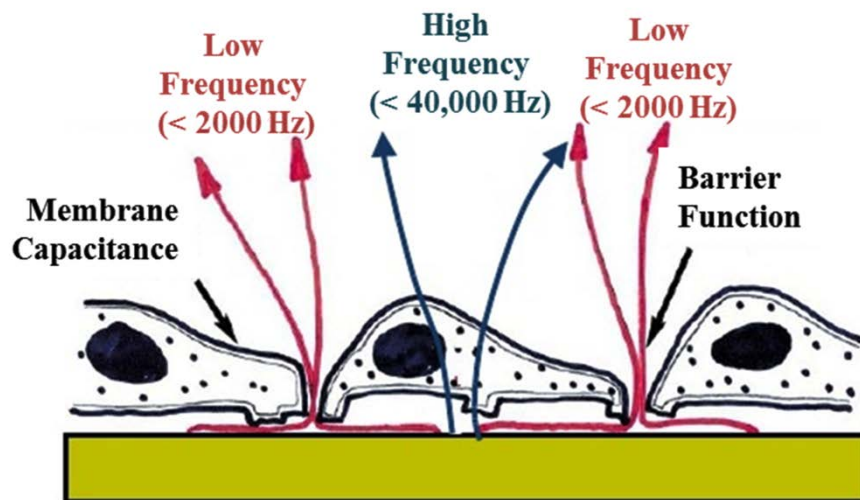


Figure 4.2: Path of current flow through monolayer of cells plated over gold electrode at different frequencies in ECIS. (Figure reproduced from Applied Biophysics)

The growth characteristics of different cell lines established in tissue culture were evaluated using ECIS. ECIS non-invasively measures the impedance across gold electrodes in the bottom of tissue culture wells at frequencies from 400 to 64,000 Hz [114-116] as a function of time. During cell growth, with changes in cell morphology and attachment to the electrodes in

the bottom of the wells, there is an accompanying change in impedance measured across the electrodes. At low frequencies (< 2000 Hz), current flows around the cells, and hence the measured impedance represents the layer's cell-to-cell barrier function (Figure 4.2) [114]. At higher frequencies ($> 40,000$ Hz), current flows directly across cell membrane, and hence the measured impedance depends on the cell coverage. In this study, spectroscopic impedance data were analyzed at two different frequencies. First, the resistance values were measured at 4,000 Hz, because at this frequency, the resistance values reflects a combination of intercellular (establishment of cell–cell junctions) and sub-cellular (cell–substrate adhesion) alterations [115]. Second, the capacitive portion of the impedance was studied at a high frequency – 64,000 Hz. These measurements essentially report only the fraction of the electrode covered with cells, and so they mimic data obtained with normal microscopy.

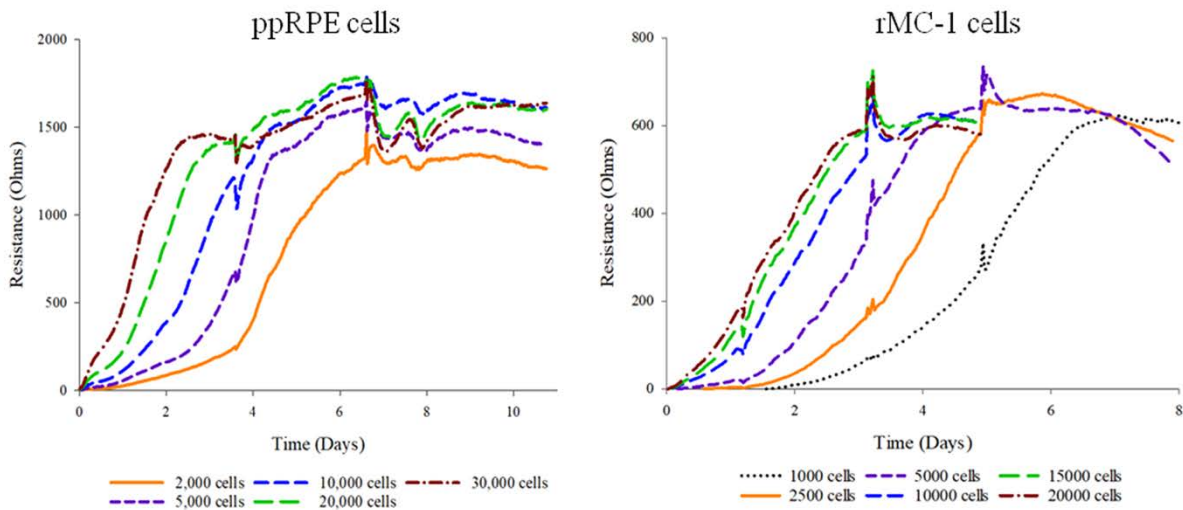


Figure 4.3: The measured resistance of (A) ppRPE and (B) rMC-1 cells seeded at different cell densities over time. The resistances were measured at 4000 Hz.

The ocular cell lines, ppRPE and rMC-1, exhibited an exponential growth till it reached confluency (Figure 4.3). The resistances of the cells increase as it attaches to the electrodes in the bottom of the wells (cell-substrate adhesion) and as the adjacent cells establish its barrier

(intracellular, barrier resistance). The resistance of the cells increases during the exponential growth and saturates at confluency. Cells seeded at different densities reach a constant saturation resistance. The growth of ARPE-19 cells and fibroblasts 3T3/NIH cells were previously studied by my colleagues in Ravi laboratory, and hence the cell seeding densities for cyto-toxicity assays were decided based on the literature values [87]. ARPE-19 cells have a growth characteristic similar to ppRPE. Unlike epithelial cells (ppRPE and ARPE-19), the fibroblasts (3T3/NIH) cells grow exponentially till they reach a peak, after which they start to decay. This is because the 3T3/NIH cells lack the property of contact inhibition.

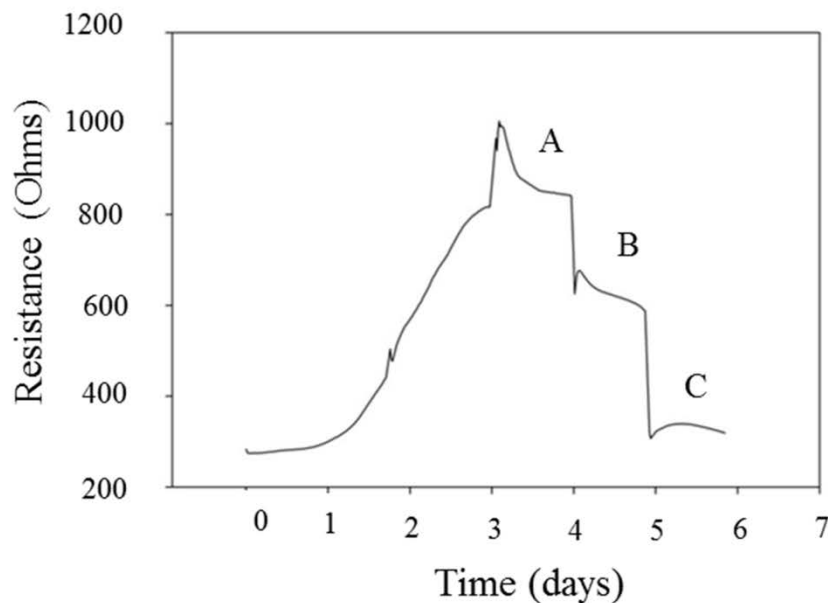


Figure 4.4: The growth behavior of the retinal muler cells (rMC-1) after reaching confluency. (1) Bright-field images of cells at different time periods. (A) At confluency, (B) 2 days after confluency, and (C) 3 days after confluency. (2) Measured resistance at 4000 Hz over time corresponding to the time periods A, B, and C. Note that media was added/exchanged on days 2, 3, 4, and 5.

The rMC-1 cells displayed a different behavior after reaching confluence compared to those of the epithelial cells (ARPE-19, and ppRPE). Unlike the epithelial cells that maintained a stable attachment to the ECIS electrode surface, the rMC-1 cells lifted up and curled, even with the slightest disturbance that occurred during medium exchange (Figure 4.4). We also observed a corresponding decrease in resistance with change in cell morphology and attachment (Figure 4.4). The reason behind this behavior is not yet elucidated; we speculate the lack of contact inhibition and vertical growth characteristic of the Müller cells may be the causes. To the best of our knowledge, we are the first ones to investigate the growth of rMC-1 in ECIS, and to observe this behavior as well.

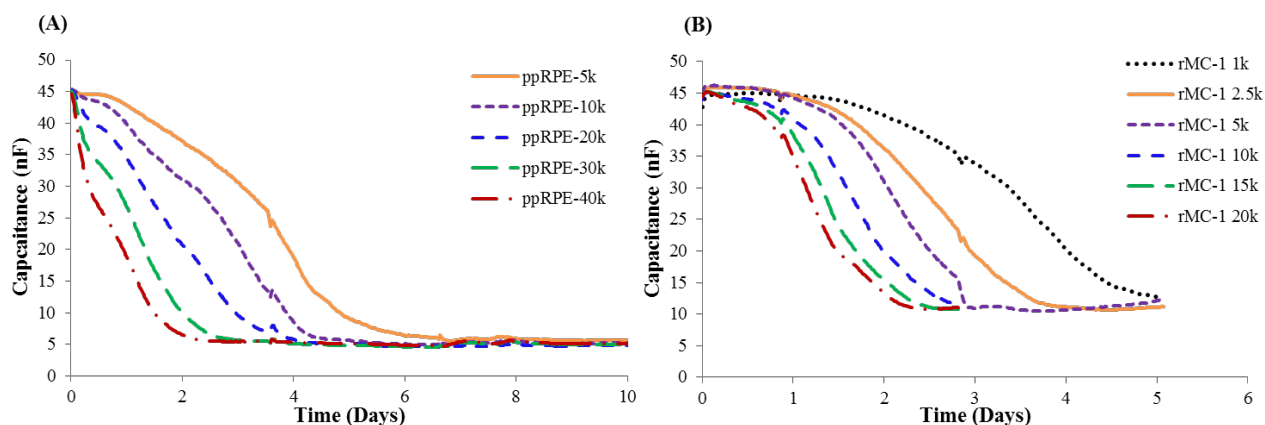


Figure 4.5: Capacitance of the cells measured at 64,000 Hz as a function of time. (A) ppRPE cells (B) rMC-1 cells. The slope of the experimental data, are fitted with linear regression models.

The doubling time of each cell line (ppRPE and rMC-1) was calculated from the capacitance vs time plot at 64,000 Hz frequency (Figure 4.5). The slope of the capacitance curve over time for cells of different seeding cell densities were fitted to a linear regression model. The goodness of fit was between 0.97-0.99. The doubling time of the cells corresponds to the time required to achieve half the value of maximum measured capacitance (the mid-point of the capacitance slope) [115]. The doubling time for ppRPE and rMC-1 cell lines at different cell

densities were determined and represented in Figure 4.6. The experimental parameters, seeding cell density and time periods, to test the biocompatibility of hydrogels on confluent layer of cells and on proliferating cells were decided based on their cell-growth characteristics and are given in section 4.1.5.

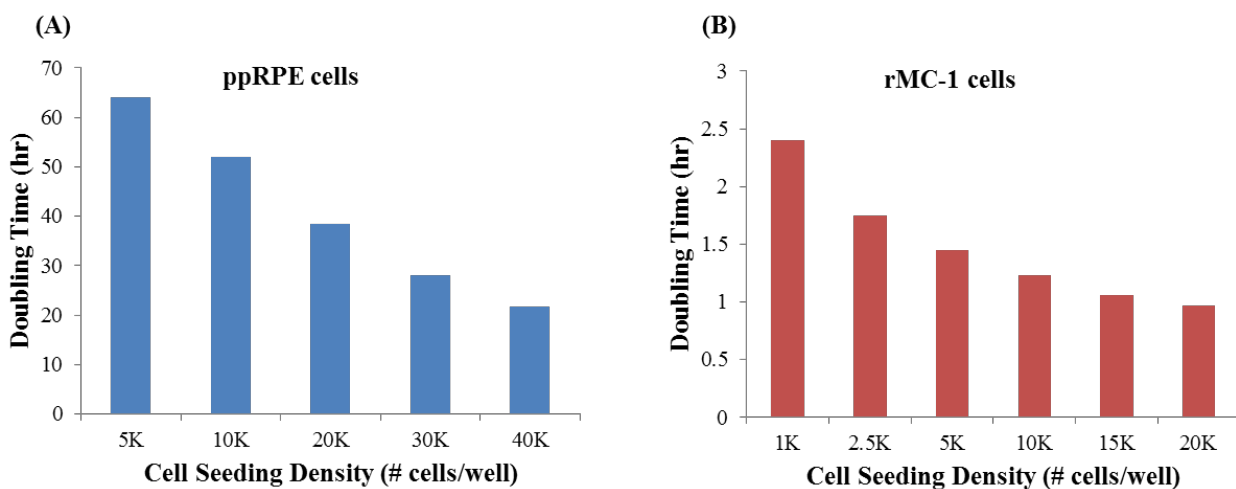


Figure 4.6: Doubling times of cells seeded at different cell densities (# of cells/well).

4.2.2 *In Vitro* Biocompatibility and Proliferation Tests for Hydrogels

The biocompatibility of the hydrogel was analyzed using ECIS. Adding a layer of polymeric gel onto the cells that are attached to the electrodes of the ECIS 96-well plate further complicates the impedance of the system. Therefore, in this study, the resistance of the cell-gel system was monitored over time at 4,000 Hz, because at this frequency the contribution of resistance from cells (inter-cellular and sub-cellular) dominates the resistance contributions from hydrogel and media.

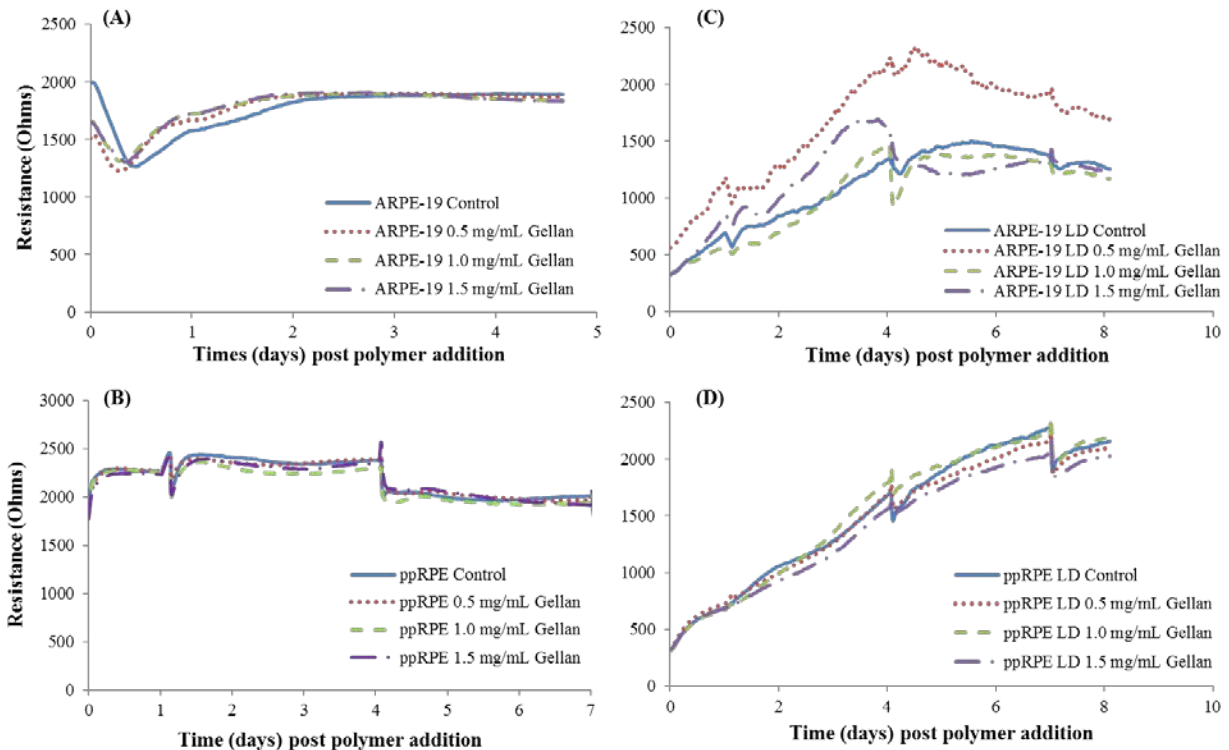


Figure 4.7: The measured resistance of ARPE-19 and ppRPE cells in contact with three different thiolated gellan hydrogel formulations over time. Controls are cells without hydrogel. All measurements were at the 4000 Hz, the optimal frequency for measuring the biocompatibility of the cells in either high density (non-proliferative, A–C) or low density (proliferative, D–F) conditions. The resistance spikes on days 1, 4, and 7 represent the exchange of cell medium.

The ARPE-19 and ppRPE cells were biocompatible with all three concentrations (0.5 mg/mL, 1.0 mg/mL, and 1.5 mg/mL) of thiolated gellan hydrogels (Figure 4.7). At confluence (Figure 4.7A, B), the resistances of both the cell lines after the addition of polymer solution are comparable to those of the control cells without gels. ARPE-19 cells exhibit a slight reduction in resistance immediately after the addition of polymer solution; however, recovers quickly within a few hours. For both cell types, the spikes on day 1, 4, and 7 indicates the exchange of DMEM/F-12 medium to maintain cell growth. The gellan hydrogels of all three concentrations were also biocompatible over a proliferating layer of ARPE-19 and ppRPE cells (Figure 4.7C, D). The proliferating cells maintained their growth rate comparable to those of the control. Mild

concentrations of gellan (0.5 mg/mL) demonstrated a resistance profile higher than those of the control, indicating that mild concentrations of gellan promote the growth of the ARPE-19 cells.

The biocompatibility of poly(MAM-co-MAA-co-BMAC) gel was determined by my colleagues, Liang et al. [87], who found that copolymer gels with concentrations less than 12.5 mg/mL were biocompatible with ARPE-19, ppRPE, and 3T3/NIH cells. All three cell lines revealed a significant decrease in resistance at 15 mg/mL copolymer concentration. Moreover, the growth curve of ARPE-19 cells plated at low density showed a more pronounced effect from the copolymers than did cells plated at high density. Therefore, we optimized three hydrogel formulations, 1.5G_5CoP, 0.9G_12CoP, and 1.5G_10CoP, which are potentially biocompatible in addition to their bio-mimetic vitreous properties. These hydrogels were further evaluated for their biocompatibility using ECIS.

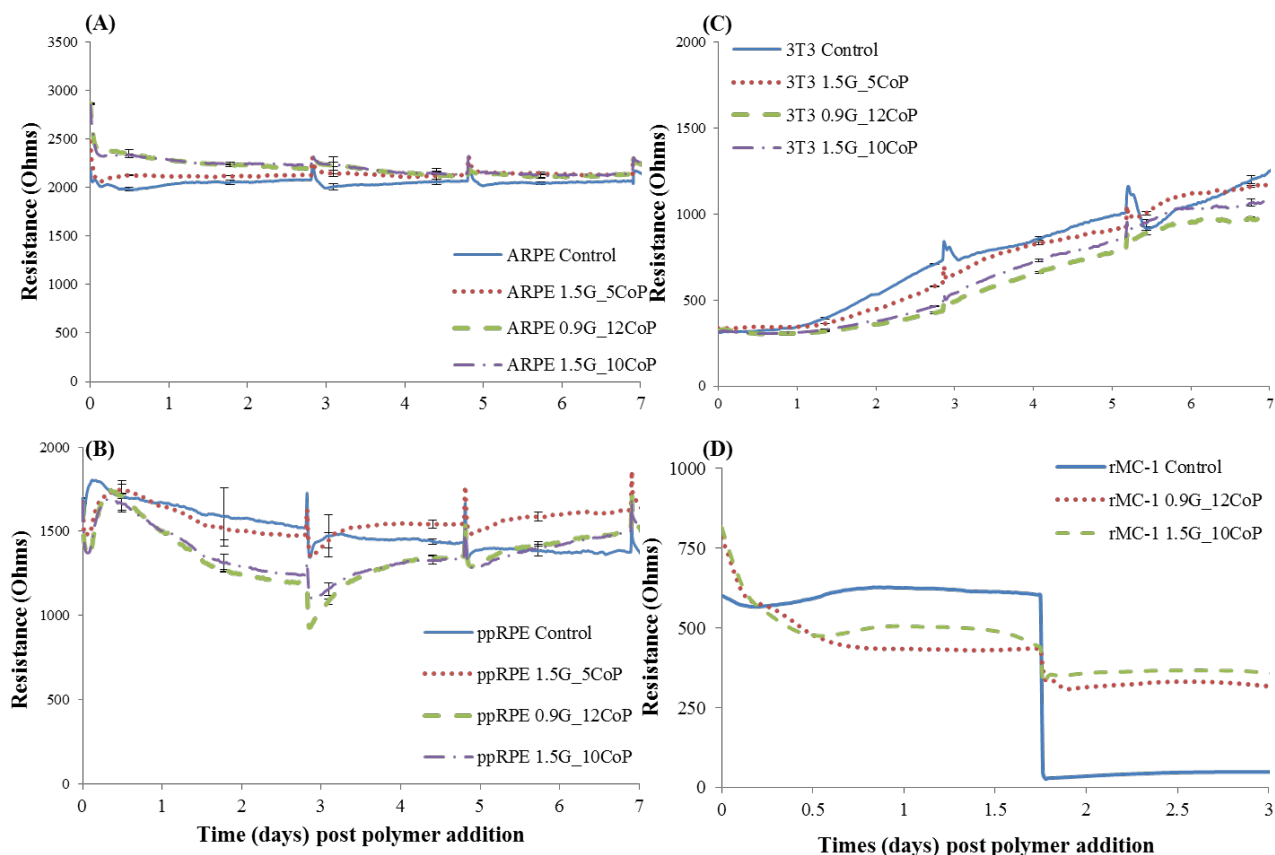


Figure 4.8: The measured resistance of cells after addition of hydrogels of different formulations. Control is cells without hydrogel. All measurements were at the 4000 Hz, the optimal frequency for measuring the biocompatibility of the hydrogels in contact with a confluent layer of cells. (A) ARPE-19 cells, (B) ppRPE cells, (C) 3T3/NIH cells, and (D) rMC-1 cells. Note that the resistance measurements were represented from the time after the addition of polymer solution to the cells. Data represents the Mean (n=4) \pm SE.

The epithelial (ARPE-19 and ppRPE) and fibroblastic (3T3/NIH) cell lines are biocompatible with the optimized formulations of the hydrogels (Figure 4.8). In the presence of the three hydrogels for six days, ARPE-19 cells revealed no significant change in resistance or toxicity (failed t-test) compared to control cells (Figure 4.8A). The control is the resistance of cells without the addition of any gel. The resistance peaks on the third and fifth day are due to the addition or change of the growth medium, which allowed the diffusion of nutrients through the hydrogel to reach the confluent layer of cells and mimic the natural eye conditions. The 3T3/NIH fibroblast cells show no significant toxicity ($p > 0.05$) similar to the ARPE-19 cells

(Figure 4.8C). The ppRPE cells show no significant toxicity with the 1.5G_5CoP hydrogel formulation (Figure 4.8B). However, the ppRPE cells in contact with the other two formulations show a 30% decrease in resistance for the first three days (Figure 4.8B). The cells do recover within the next two days and achieve the same resistance as the control by the end of six days. The initial decrease in resistance may correspond to the presence of thiol groups in the physically crosslinked gel in contact with the cells. In the first three days, the thiol groups completely oxidize to form disulfide linkages in the hydrogel [76], while the cells compete with the thiol groups for dissolved oxygen. Upon addition of fresh media on the third day, the cells recover quickly. In addition, the t-tests on the ppRPE cells in contact with the hydrogels on day 6 failed statistically, showing that the cells are biocompatible with all three hydrogels.

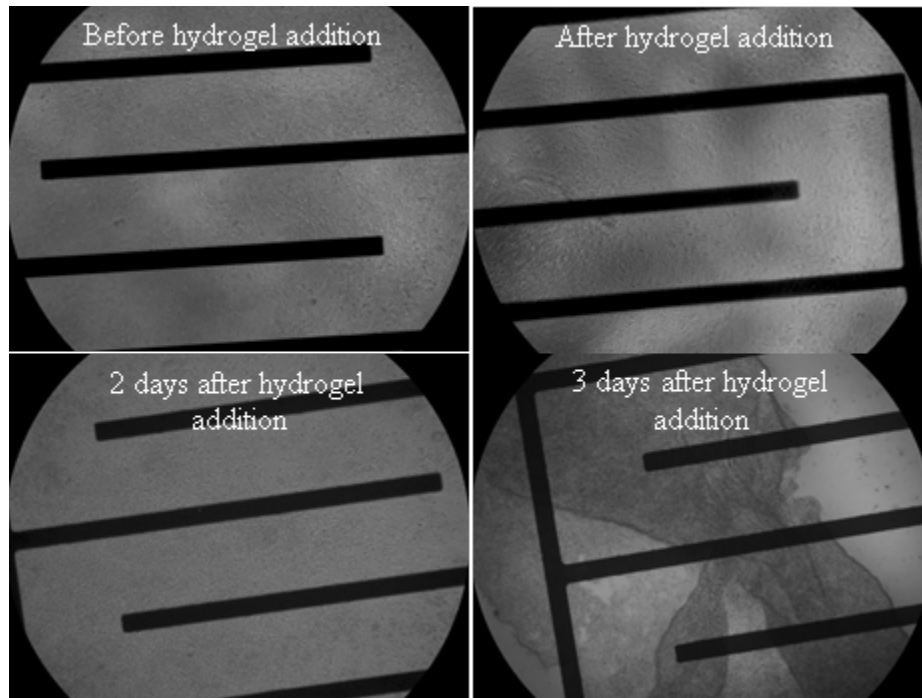


Figure 4.9: Morphology of rMC-1 at different time periods. The hydrogels were added over a confluent layer of the RMCs and were found to be biocompatible without any drastic change in the morphology. The cell densities of rMC-1 increase with each day and curl up after 2 days of confluency due to excessive growth.

The *in situ*-forming hydrogel were also biocompatible with a confluent layer of retinal Müller cells (rMC-1). At 4000 Hz, resistances of the cells in contact with the hydrogels over ≈ 2

days after hydrogel addition were comparable to those of control cells (without hydrogel) in ECIS (Figure 4.8D). The resistances of the cells (including the control) dropped after the exchange of medium at the beginning of day 3. The drop in resistance for all experimental groups is consistent with the curling of the cells as shown in Figure 4.9, and with the observations of rMC-1 growth described in section 4.2.1.

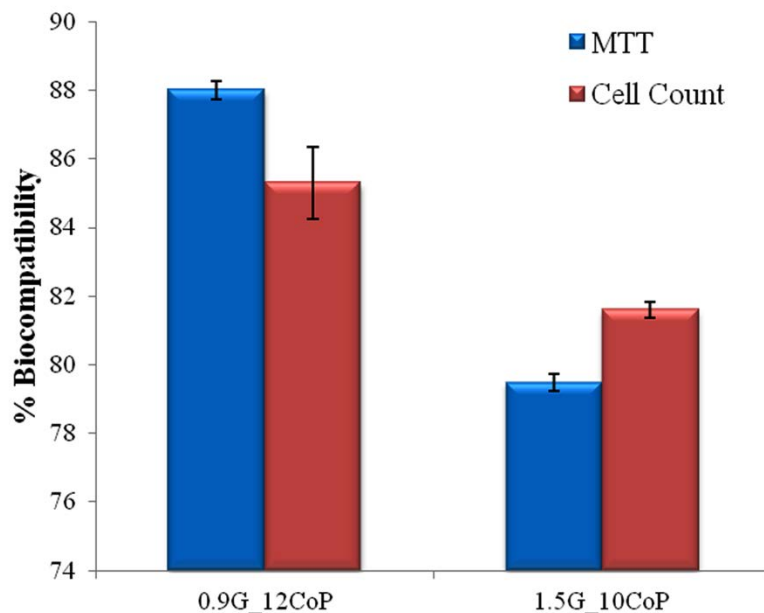


Figure 4.10: The % biocompatibility of hydrogels from MTT, and Cell count analysis. The biocompatibility of the control (cells without the hydrogel) was fixed at 100%. Data represents the Mean (n=4) \pm SE.

To confirm the biocompatibility results with rMC-1 cells, we investigated the biocompatibility of hydrogels using MTT assay and simultaneously counted the number of cells. MTT and cell count analysis at 3 days after the hydrogel addition confirmed that both the hydrogels were biocompatible with the cells. The hydrogel biocompatibility percentage was greater than 80% compared to the control, which was fixed at 100% (Figure 4.10).

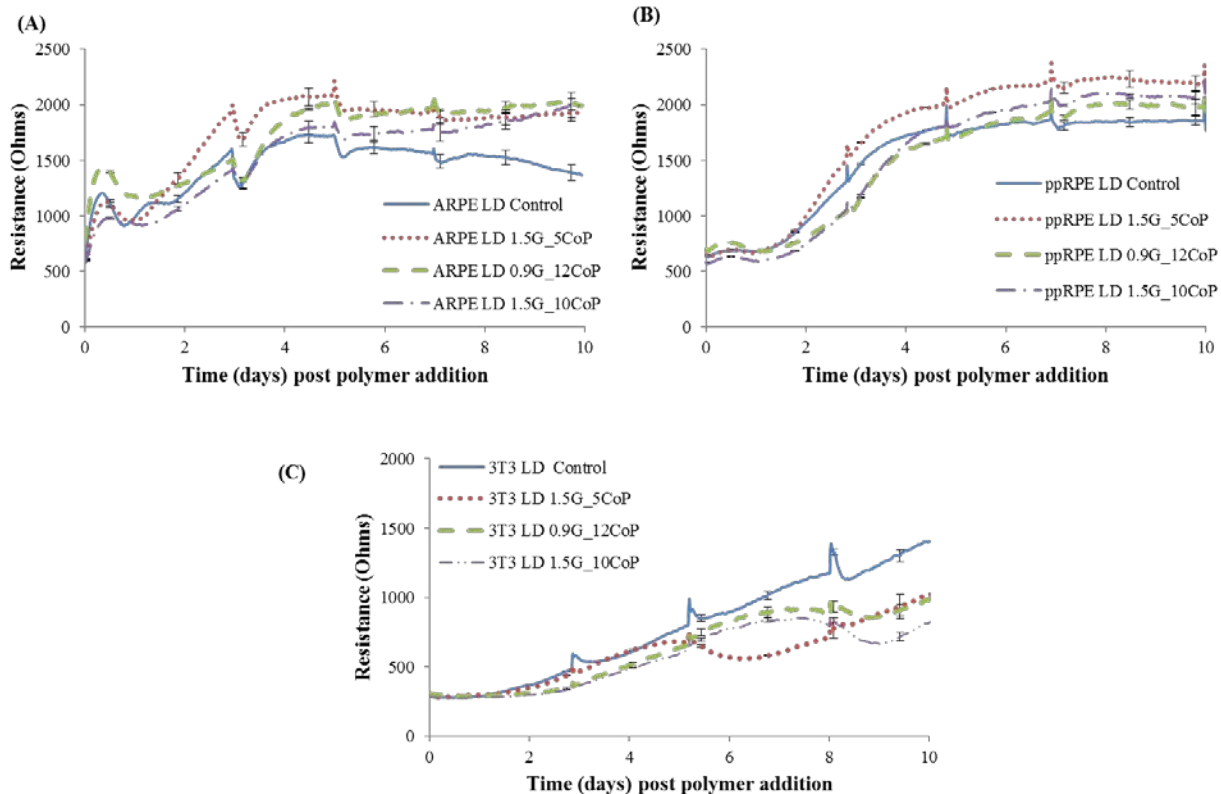


Figure 4.11: Measured resistance of proliferating layer of cells in contact with three hydrogel formulations over time. Control is the cells without hydrogel. The resistances were measured at 4000 Hz frequency. Each data point in the hydrogels and control represents the average of 15 wells and 3 respectively. Data represents the Mean ($n=4$) \pm SE.

In addition to demonstrating biocompatibility at confluence, cells of all three types in growth phase or in proliferation were also biocompatible with the hydrogels (Figure 4.11A, B & C). The resistance peaks at various times indicate the exchange of medium. Both the ARPE-19 and ppRPE cells proliferated well in the presence of all the three optimized formulations of hydrogel (Figure 4.11A & B). The resistance of these cells after 10 days in contact with gel was significantly higher compared to the control cells without the gel (p -value <0.01 , failed t -test). With the ppRPE cells there is a slight initial drop in resistance, which did not affect their growth (Figure 4.11B).

The cell morphology was also monitored after addition of the polymer solution. As an example, Figure 4.12 shows cells in contact with the 0.9G_12CoP hydrogel observed under

bright field illumination at 10X magnification on days 4, 7, and 11 after the addition of polymer solution. The morphology of the retinal cells was not affected by any formulation, and the images show that the number of cells increased with time (Figure 4.12). These findings indicate (1) the three formulations are biocompatible with the ppRPE and ARPE-19 cell lines and (2) the studies of hydrogel obtained from ECIS are consistent with changes in cell morphology.

3T3/NIH cells also proliferated in the presence of the three hydrogel formulations (Figure 4.11C). The cells in contact with the 1.5G_5CoP hydrogel statistically failed the t-test on day 5 and failed with the other two hydrogels on day 6. However, after day 7, cell growth and activity was lower than that of the control cells. Bright-field microscopic images of 3T3/NIH cells indicated a possible slight slowing of cell growth in contact with 0.9G_12CoP hydrogel by day 11 (Figure 4.12). However, the morphology of the 3T3/NIH cells still appears to be relatively normal.

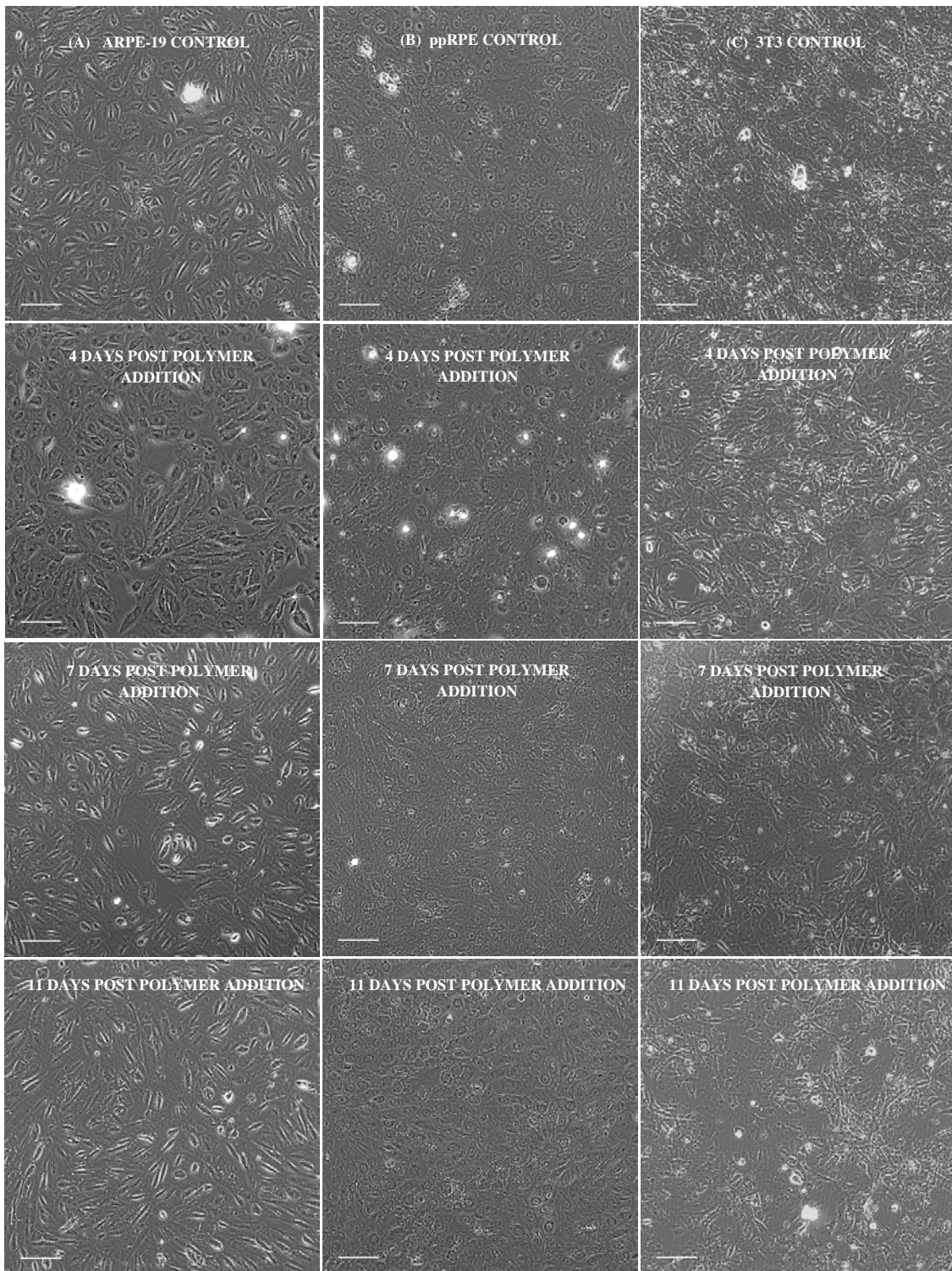


Figure 4.12: Bright-field images of (A) ARPE-19, (B) ppRPE, and (C) 3T3/NIH cells alone (control on 11th day) and in contact with composite hydrogel 0.9G_12CoP on the 4th, 7th and 11th day post polymer addition (Scale bar – 100 μ m).

To check if the hydrogel affects the integrity of the cell junctions, the barrier resistance (R_b) of the three cell lines was analyzed by ECIS modelling software, which separated out the different components of cell-layer resistance. The barrier resistances of ARPE-19 and 3T3/NIH cells were not affected by the three hydrogels, and they followed a similar pattern as the resistances measured in Figure 4.8A, C. Figure 4.13 shows the R_b from the time of the plating of the ppRPE cells. After tight junctions form completely, the R_b is around 3.25 – 3.75 times the resistance of the empty well. The control ppRPE cell barrier functions start to deteriorate from day 7 on. After the addition of polymer, the barrier resistance for ppRPE cells was lower than the controls from day 1 to 3, similar to the results observed at 4,000 Hz. However, with complete chemical crosslinking of the gel and a medium exchange, the R_b recovers significantly and also fails the t-test on day 12, confirming the reformation of tight cell junctions (Figure 4.13).

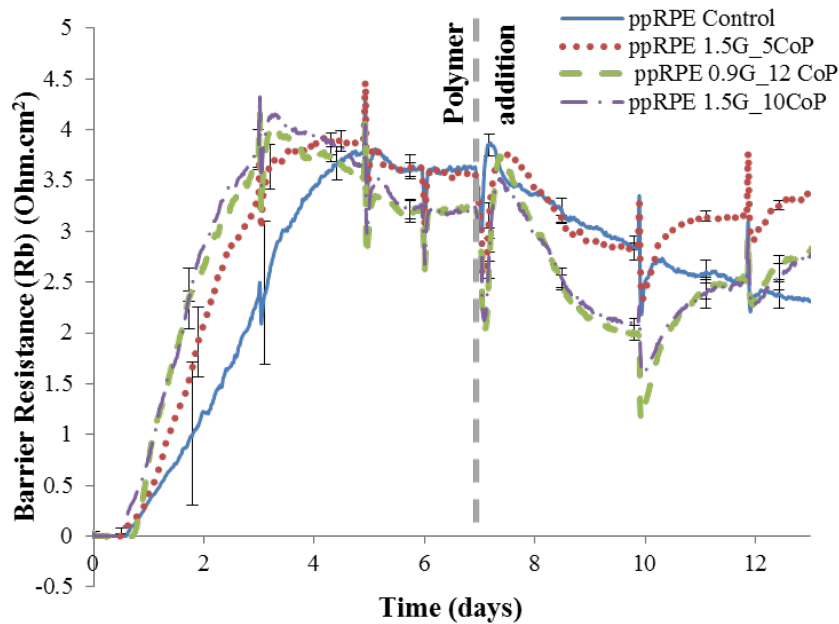


Figure 4.13: Barrier resistance measurements in Ohm.cm^2 over time (days) for ppRPE cells plated at high density (40,000 cells/well) for three different formulations of hydrogel. The spikes in resistances denote medium exchanges. Data represents the Mean ($n=4$) \pm SE.

4.2.3 *In Vitro* Degradation of Hydrogels

In four weeks, the hydrogels did not show significant loss in mass (p-value > 0.05) in the presence of lysozyme and trypsin. In fact, a slight increase in mass was observed, similar to the control (Figure 4.14A), which might have been due to swelling and protein absorption in the hydrogels in contact with the enzymatic solutions. After 0.9G_12CoP and 1.5G_10CoP hydrogels were incubated with enzymatic solutions for four weeks, their storage moduli showed similar pattern as the control (Figure 4.14B). We chose lysozyme and trypsin for our degradation studies because lysosomal enzymes are distributed widely in various ocular tissues and trypsin is a commonly used enzyme that hydrolyzes proteins. Van deemter et al [117] detected trypsin in the vitreous, and explored its function in the degradation of collagen fibrils. In our work, hydrogels did not degrade within 28 days due to the strong chemical cross-links (S-S linkages) in the hydrogel network.

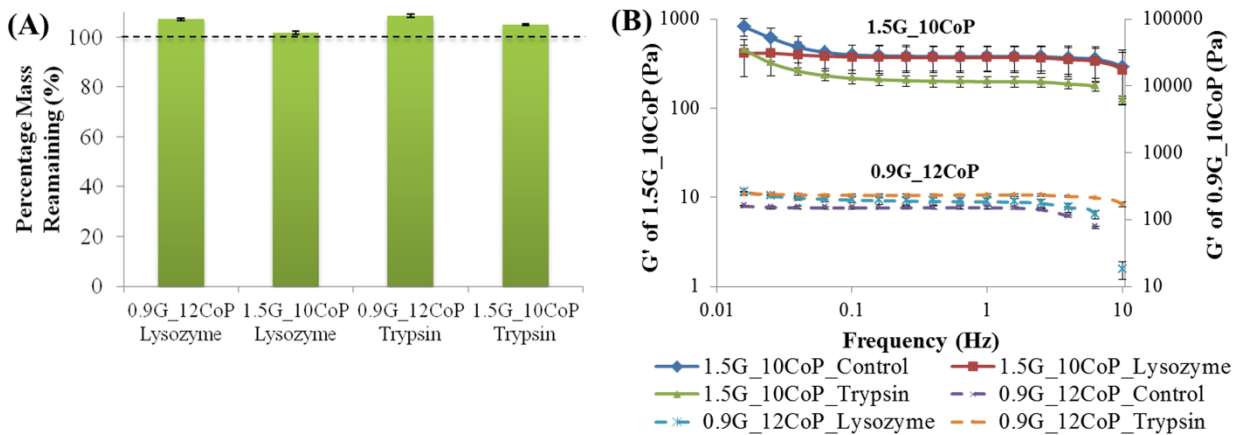


Figure 4.14: Degradation studies. (A) Percent of mass remaining in the 0.9G_12CoP and 1.5G_10CoP hydrogels after 4 weeks in the presence of lysozyme and trypsin. (B) Storage moduli of 1.5G_10CoP and 0.9G_12CoP at different frequencies. Control is the hydrogel in 1X PBS. Error bars are the standard deviations from three replicates of each sample.

Both the hydrogel were also evaluated for 30 days in contact with the insert membrane supporting ppRPE cells on its apical side, and was found to be stable and non-degradable. The

ppRPE cells stayed alive and maintained a monolayer in the presence of 1.5G_10CoP hydrogel, as they did in the control cells, the cells without hydrogel (Figure 4.15). Furthermore, the actin density, which is linked to the overall health of the cells [118], was not compromised in the presence of the hydrogels. Thus, there was no apparent toxic effect of the hydrogels on the ppRPE cells. Moreover, the storage moduli of the hydrogel were comparable to that of the hydrogel alone (control) at 1 Hz frequency, indicating that the hydrogel was still well-formed. The stability of the gel is most likely due to its strong physical and chemical cross-links (S-S linkages).

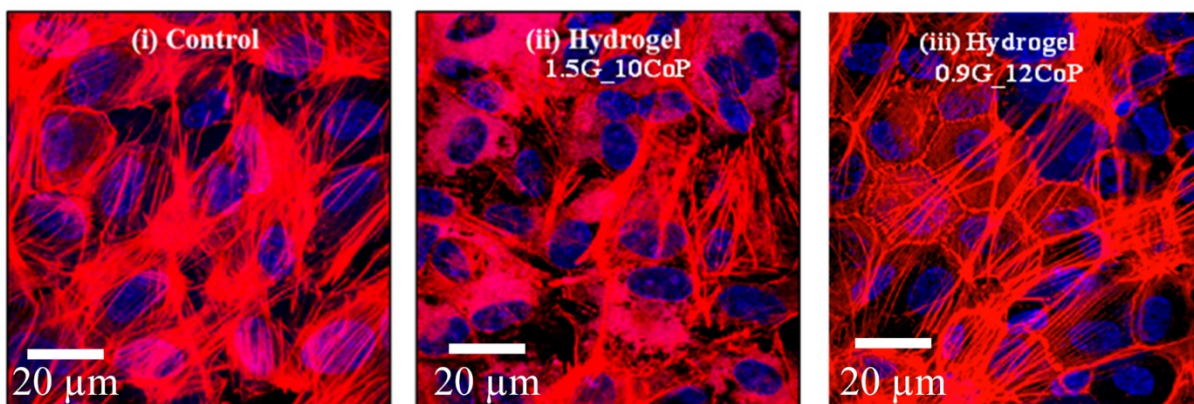


Figure 4.15: Degradation study on the hydrogel. Confocal images of the ppRPE cells. The image shows the monolayer of cells stained for nuclei (blue; DAPI) and cell matrix – actin fibers (red; phalloidin) in (i) Control medium (without hydrogel contact) and in contact with (ii) 1.5G_10CoP hydrogel and (iii) 0.9G_12CoP hydrogel. No toxic effect was observed.

4.2.4 Biocompatibility Evaluations of Hydrogels on Rabbits

The *in situ*-forming hydrogels, 0.9G_12CoP, and 1.5G_10CoP, were easily incorporated into standard vitrectomy procedures via injection. No significant inflammation in the anterior segment of the eye was observed in slit lamp examinations performed on days 1, 7, and 30 after surgery. The conjunctiva was mildly inflamed on day 1 post-operation, but this was significantly reduced on day 4, and the conjunctiva was clear and colorless by post-operative day 7. The lenses were clear, and the Y-suture was clearly visible in rabbits treated with the hydrogels.

However, six silicone-oil-treated (n=10), three 0.9G_12CoP-treated (n=11), and six 1.5G_10CoP-treated (n=11) rabbits had a slight posterior polar cataract at 30 days post-operation. In three of the six 1.5G_10CoP hydrogel-treated rabbits, the cataract was localized, which indicated that surgical trauma during vitrectomy was the cause. A global cataract would be expected with vitreous substitute toxicity. The retina and the optic nerve appeared normal. With one exception, funduscopy examinations on post-operative day 30 revealed no vitreous opacity, vitreous hemorrhage, membrane formation, or chorio-retinal lesions (Figure 4.16A). In one rabbit treated with 1.5G_10CoP hydrogel, vitreous hemorrhage occurred during surgery, and was still present on day 30.

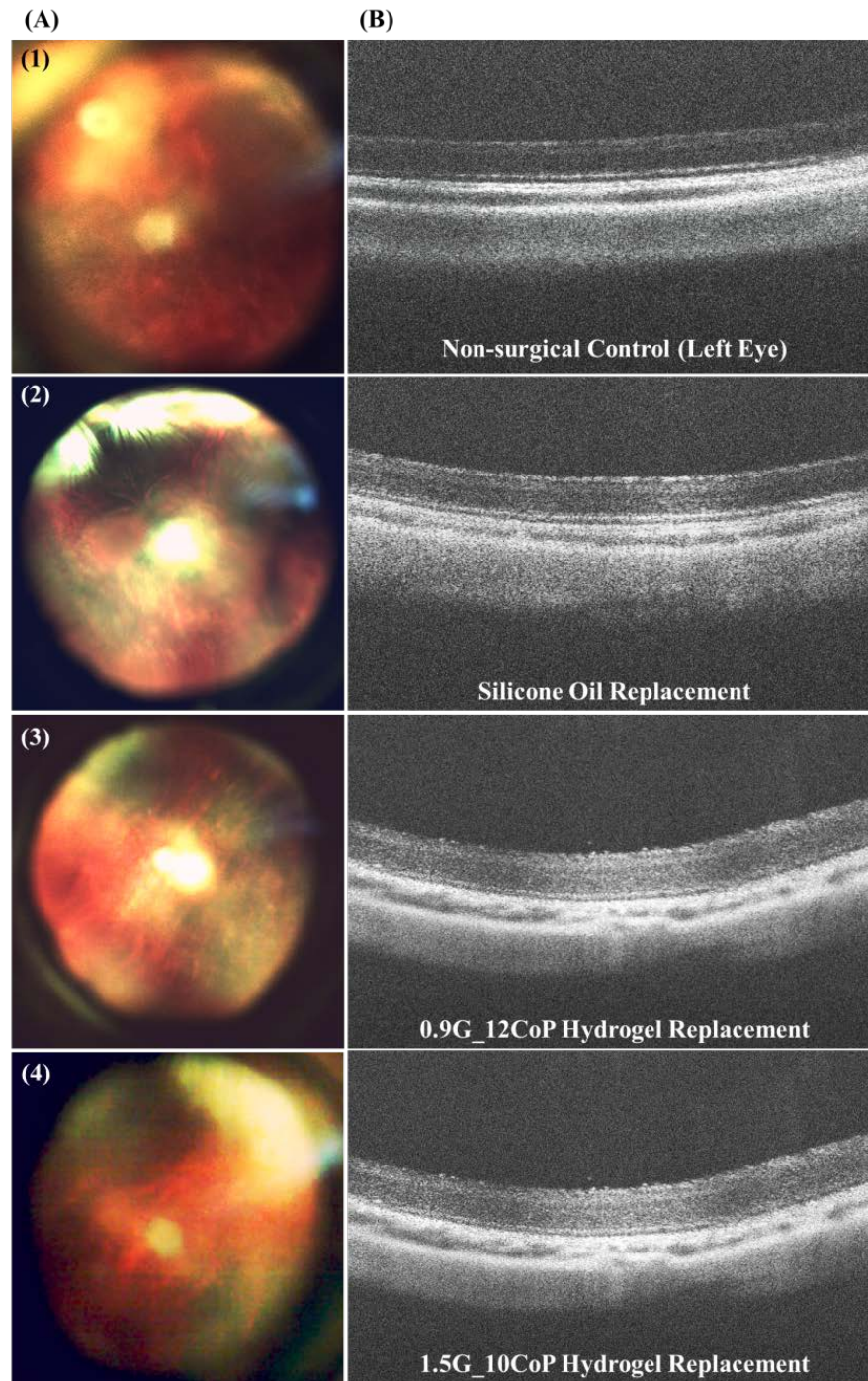


Figure 4.16: (A) Fundoscopic and (B) OCT images of rabbit vitreous cavities and retinas. (1) Non-surgical control (2) Silicone oil vitreous replacement (3) 0.9G_12CoP replacement, and (4) 1.5G_10CoP hydrogel replacement. No vitreous opacity, vitreous hemorrhage, membrane formation, chorio-retinal lesions, or atrophy in retinal layers is observed.

Optical coherence tomography was performed on four rabbits in each group and showed no retinal detachment 30 days post-operation. Column B in Figure 4.16 shows the OCT retinal

right-eye cross-section images of rabbits treated with 0.9G_12CoP, 1.5G_10CoP hydrogels, and SO, as well as an image of non-surgical control (left eye) at 30 days post-operation. The retinal thickness of the treated eye is comparable to that of the untreated-control eye. There was no atrophy in the retinal thickness of either the hydrogel-treated rabbits or the silicone oil-treated rabbits.

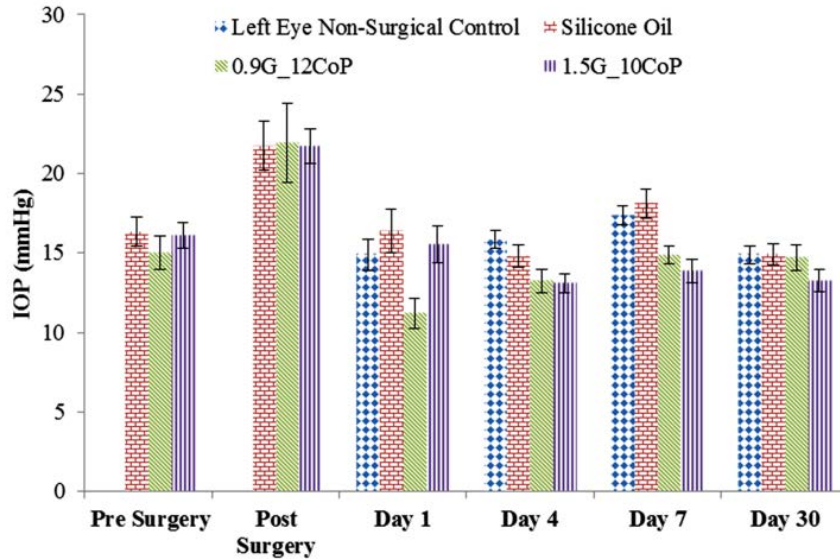


Figure 4.17: Pre-surgical and post-surgical IOP measurements in all experimental groups. Data represents the mean \pm SE. At 30 days post-operation, no significant difference was observed in IOPs of the hydrogel-treated rabbits (n=10 for 0.9G_12CoP and n=8 for 1.5G_10CoP gel) compared to the controls (n=10 for silicone oil and n=24 for non-surgical control).

Pre-surgical and post-surgical IOP measurements were comparable for all experimental groups (Figure 4.17). On post-operative day 1, 0.9G_12 CoP hydrogel showed a decrease in IOP, but this difference was recovered by day 4. The literature value for an average rabbit IOP is 15.44 ± 2.16 mmHg [119], with a range of 11-21 mmHg during the light phase of the diurnal cycle. All IOP measurements fell within the published rabbit IOP range [119], with the exception of immediate post-operation measurements in all experimental groups and the SO control, where the experimental values were slightly higher than the reported values in the literature. In addition, a two-tailed t-test showed no significant difference ($p > 0.10$) in the final

IOPs (day 30 post-operation) of the experimental groups compared to the silicone oil and the non-surgical control.

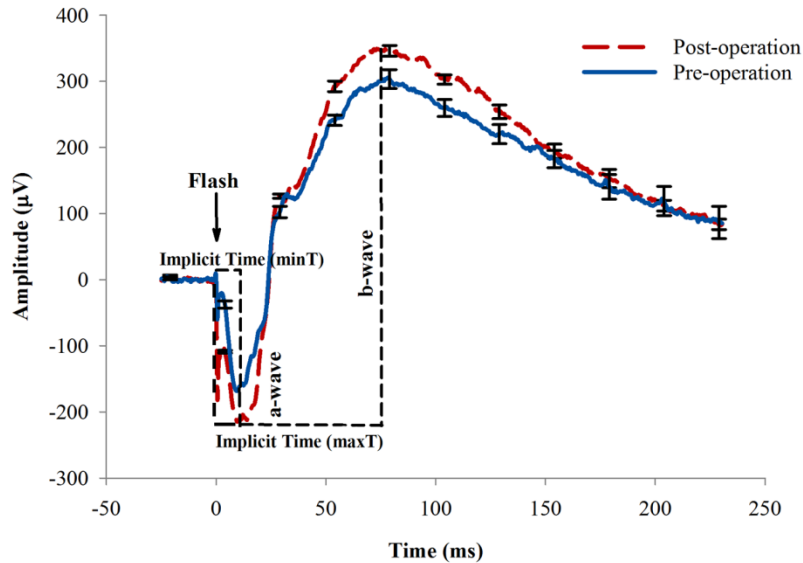


Figure 4.18: ERG response (n=5) of a rabbit retina elicited by light stimuli under mesopic conditions (moderate light conditions where both rods and cones are active). The ERG responses were obtained before and 30 days post-operation, where rabbit vitreous was partially replaced with a 0.9G₁₂CoP hydrogel. Data represent the mean amplitudes (n=5) \pm SE.

Electroretinogram analysis revealed normal retinal function in the rabbits treated with our hydrogels. The rabbits showed a characteristic ERG wave pattern in response to light stimuli, with a negative deflection (a-wave, due to hyper-polarization of the photoreceptor layer) followed by a positive amplitude peak (b-wave, due to de-polarization of the Müller cells) 7 days prior and 30 days post-operation (Figure 4.18). Table 4.1 summarizes the amplitudes and implicit times (time-to-peak from the onset of flash stimuli) of the characteristic waves in response to light stimuli under scotopic (dark-adapted), photopic (light-adapted), and standard mesopic (both scotopic and photopic) conditions. The data summarized are raw data without any processing, and hence are likely to have a considerable standard error. The amplitudes for SO treated-rabbits, including the deviations, were comparable to those found by Mackiewicz et al. [120].

Table 4.1: Amplitudes and implicit times of characteristic waves in response to standard mesopic, scotopic, and photopic light stimuli.

		Standard Mesopic Light Stimulus				Scotopic Stimulus		Photopic Stimulus	
		a-Wave	a-Wave	b-Wave	b-Wave	b-Wave	b-Wave	b-Wave	b-Wave
		Amplitude (μV)	Implicit time (ms)	Amplitude (μV)	Implicit time (ms)	Amplitude (μV)	Implicit time (ms)	Amplitude (μV)	Implicit time (ms)
Silicone oil	Pre	171.04 ± 3.75	11.75 ± 0.39	346.31 ± 21.63	76.33 ± 7.31	225.01 ± 30.55	48.04 ± 2.75	161.29 ± 8.10	56.50 ± 21.47
	Post	179.66 ± 10.38	11.08 ± 0.58	345.88 ± 33.44	73.42 ± 7.49	217.64 ± 29.22	59.86 ± 5.75	157.10 ± 8.68	29.58 ± 0.51
0.9G_12CoP	Pre	160.93 ± 8.00	11.08 ± 0.42	359.06 ± 28.48	70.33 ± 7.51	244.78 ± 27.79	61.85 ± 6.12	143.81 ± 15.06	28.50 ± 0.82
	Post	164.55 ± 9.32	10.08 ± 0.30	412.35 ± 38.04	60.50 ± 8.45	287.97 ± 24.43	87.73 ± 7.14	181.65 ± 11.81	28.25 ± 0.65
1.5G_10CoP	Pre	145.44 ± 11.17	11.19 ± 10.38	268.59 ± 30.54	59.25 ± 9.12	150.40 ± 19.58	64.68 ± 4.01	129.33 ± 14.99	50.19 ± 19.90
	Post	131.21 ± 4.35	13.50 ± 1.11	295.72 ± 19.82	69.19 ± 10.88	156.46 ± 31.97	50.40 ± 15.67	128.12 ± 18.44	30.44 ± 1.05

The ratio of the post-operative to the pre-operative ERG parameters was calculated. The ERG responses (amplitudes and implicit times) of the experimental groups (hydrogels) stimulated with a standard mesopic light flash were not significantly different ($p > 0.10$) from the

SO control (Figure 4.19A, 4.19B), except for the b-wave amplitude of 0.9G_12CoP ($p = 0.04$) hydrogel.

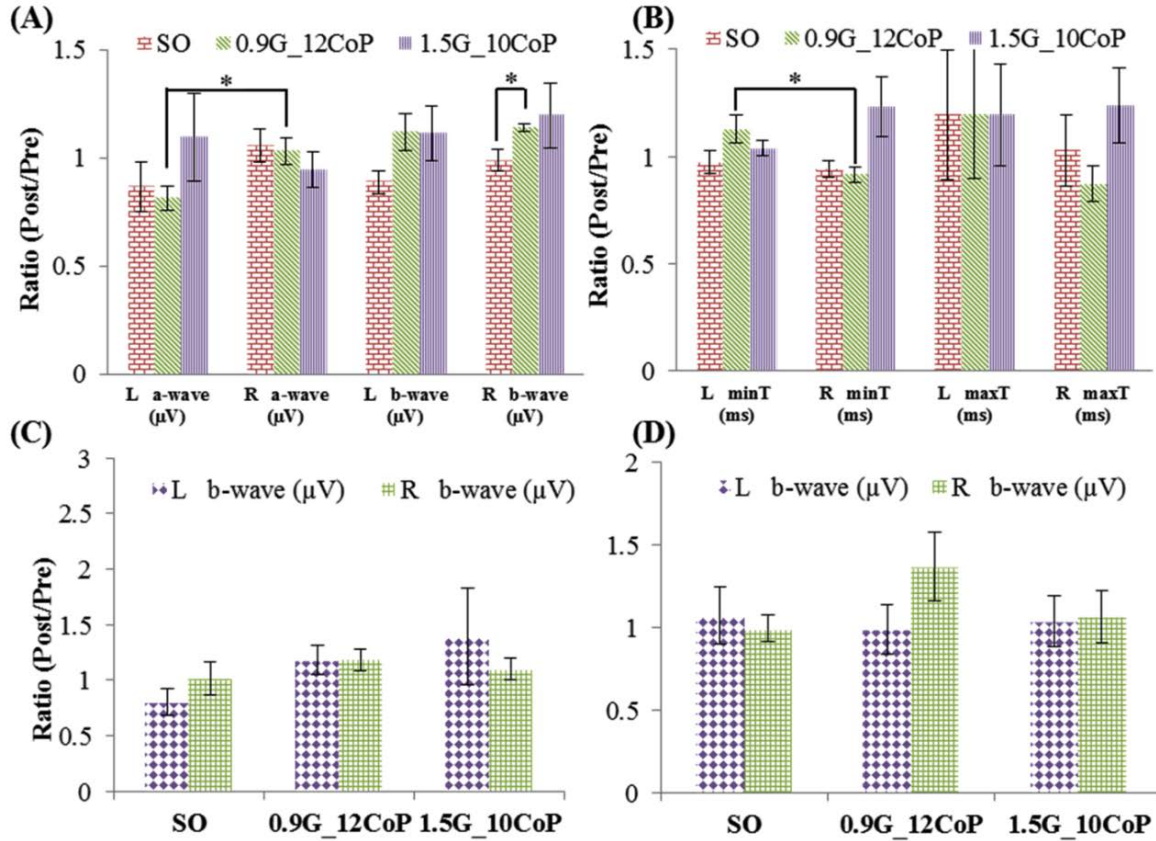


Figure 4.19: The characteristic ratios of post- to pre-operative a-wave and b-wave amplitudes (A, C, D), and corresponding implicit times (B) of the vitreous-substitute- treated (right, R) eye and the control (left, L) eye, when stimulated with standard mesopic ($2.526 \text{ cd}\cdot\text{s}\cdot\text{m}^{-2}$) light (A, B), scotopic light in dark adapted conditions (C), and photopic flash in light adapted conditions (D). (A) compares the amplitude between substitutes, and (B) compares the implicit times between substitutes. The photoreceptor activity was normal and functional with the hydrogels.

The b-wave amplitude of the 0.9G_12CoP treated eye is higher than the SO control, and is statistically comparable to the left eye control, suggesting normal photoreceptor activity. Furthermore, the amplitudes and implicit times of the treated (right eye) are comparable to those of the non-surgical control (left eye) in the experimental groups, except for the a-wave amplitude ($p = 0.04$) and the corresponding minimum implicit time (minT, $p = 0.03$) of 0.9G_12CoP hydrogel. The increase in the a-wave amplitude and the corresponding decrease in the implicit

time (minT) of the 0.9G_12CoP gel are both statistically significant in comparison to the non-surgical control, indicating that the photoreceptors have better functional activity than the control. Therefore, it was concluded that hydrogel-treated rabbits exhibited normal rod and cone activity. The exclusive activity of rods stimulated by $0.010 \text{ cd}\cdot\text{s}\cdot\text{m}^{-2}$ scotopic light flashes in the dark adapted rabbits was normal (Figure 4.19C). Furthermore, the activity of cones was confirmed to be normal through the photopic and flicker response in light adapted conditions. The b-wave amplitude ratio was nearly 1 in response to photopic flashes (Figure 4.19D). In addition, there was no absolute difference in flicker responses. Statistically, there was no significant difference between the ERG responses of the experimental groups when stimulated with different light flashes compared to the silicone oil and the non-surgical controls, indicating that the hydrogel-substitutes were biocompatible in the rabbit eyes and exhibited similar retinal activity to the controls.

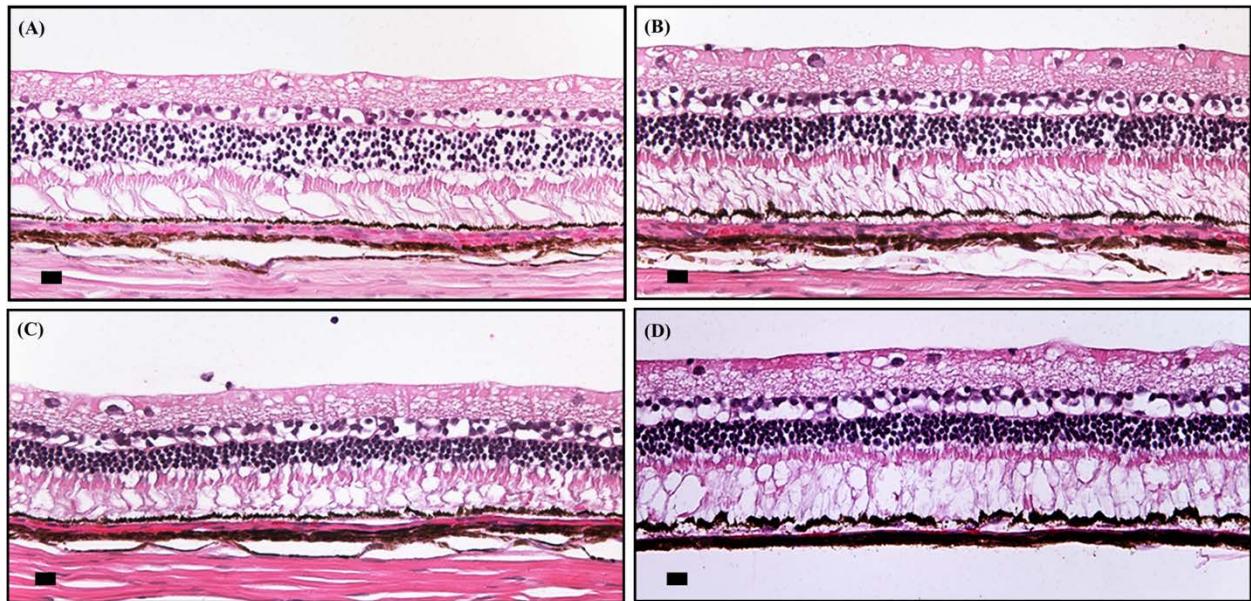


Figure 4.20: Bright-field microscopic image (H&E staining, Scale bar = $50\mu\text{m}$) of rabbit retinas. (A) Non-surgical control. (B) Silicone oil, (C) 0.9G_12CoP hydrogel, and (D) 1.5G_10CoP hydrogel. B, C, and D are retinas of rabbit eyes with partial vitreous replacements. All retinal layers were intact, without any retinal atrophy.

Histopathological examinations revealed that the retinal layers were intact in the rabbits treated with the hydrogels. Figure 4.20 shows the retinal structure of rabbit eyes treated with 0.9G_12 CoP and 1.5G_10CoP hydrogel, and with SO, at 30 days post-operation. The integrity of the retinal layers was preserved, and no significant pathological inflammation or deformation, such as retinal edema, epiretinal membranes, atrophic changes of the retinal layers, hemorrhage, or mononuclear cell inflammation were observed in the experimental group compared to the SO group (Figure 4.21). When qualitatively scored, the pathological changes in the retina of the experimental groups were found to be less than 1 (0 = no change and 4 = severe change). A minimal number of mononuclear inflammatory cells in the vitreous were common. The presence of mono-nuclear inflammatory cells is perhaps due to focal trauma to the posterior lens capsule, and to the presence of a suture line near the ora ciliaris that may have introduced foreign material. Both of these sources of inflammation are likely to occur during the surgical procedure, due to the anatomical huge lens of rabbits. The H&E-stained sections displayed a normal retinal morphology, without any degenerate changes in the retina.

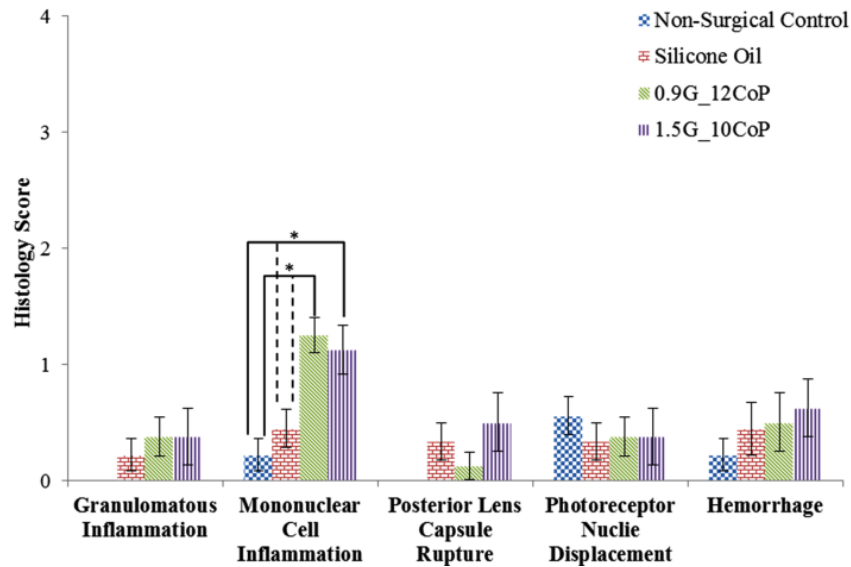


Figure 4.21: Histopathology scores for rabbit retinas with silicone oil (n=9), 0.9G_12CoP (n=8), and 1.5G_10CoP (n=8) hydrogel as vitreous replacements. Scores from 0 to 4 indicate severity, from null to severe.

Data represent the mean \pm SE. No significant difference was observed between the hydrogels and the controls, with the exception for the mononuclear cell inflammation, which was common, but minimal (score~1).

Our hydrogel may prevent retinal detachment and can function to keep the retina in position. Retinal tears accidentally occurred during surgery in two rabbits receiving hydrogel as a vitreous replacement. At 30 days post-operation, direct visual examination by our vitreo-retinal surgeon, as well as OCT and ERG examination, revealed that the retinal tear did not develop into a retinal detachment. The retinal thickness was similar to that of the controls when analyzed using OCT. In addition, the ERG analysis demonstrated no significant changes in the activity of rods and cones, compared to the silicone oil control.

4.2.5 *In Vivo* Oxygen Tension Evaluations for Vitreous Substitutes

The native vitreous gel maintains an oxygen gradient in the vitreous cavity, with the highest near retinal vasculature and the lowest near posterior lens [33, 121]. After vitrectomy, there is a drastic increase in oxygen levels in the vitreous cavity compared to pre-vitrectomy [31, 32, 121]. Holekamp et al. [31] revealed that the oxygen gradient maintained by the intact vitreous gel is lost after its removal in humans. Furthermore, Barbazetto et al. [121] showed that the rabbit eyes replaced with balanced salt solution (BSS) after vitrectomy, does not maintain the oxygen gradient that was observed in the native vitreous. They also reported that an increase in oxygen after vitrectomy leads to an increase in lenticular oxygen tension with the subsequent formation of a nuclear cataract. Therefore, there is a need to preserve the low oxygen environment near the lens before and after vitrectomy.

In this study, we measured the partial pressure of oxygen (oxygen tension) in rabbit's vitreous, which were replaced with either silicone oil (n=3) or 1.5G_10CoP hydrogels (n=9) after 30 days post-surgery. The non-surgical (left eye, n=8), and the silicone oil substituted eye (surgical, right eye) were the controls. The oxygen tension in the medium (vitreous/substitutes)

was measured at two sites: (1) Vitrectomy site, where the vitreous was replaced with the substitutes, either silicone oil or 1.5G_10CoP hydrogel, during the partial pars planar vitrectomy. (2) Intra-vitreous site, where the vitreous remained intact (Figure 4.1). The partial pressure of oxygen (pO_2) at the intra-vitreous site was comparable between the left eye (non-surgical control), silicone oil- and 1.5G_10CoP hydrogel-replaced rabbit eyes. The results indicate that the vitreous remains intact and maintains its oxygen levels at the intra-vitreous site after the partial pars planar vitrectomy (Figure 4.22).

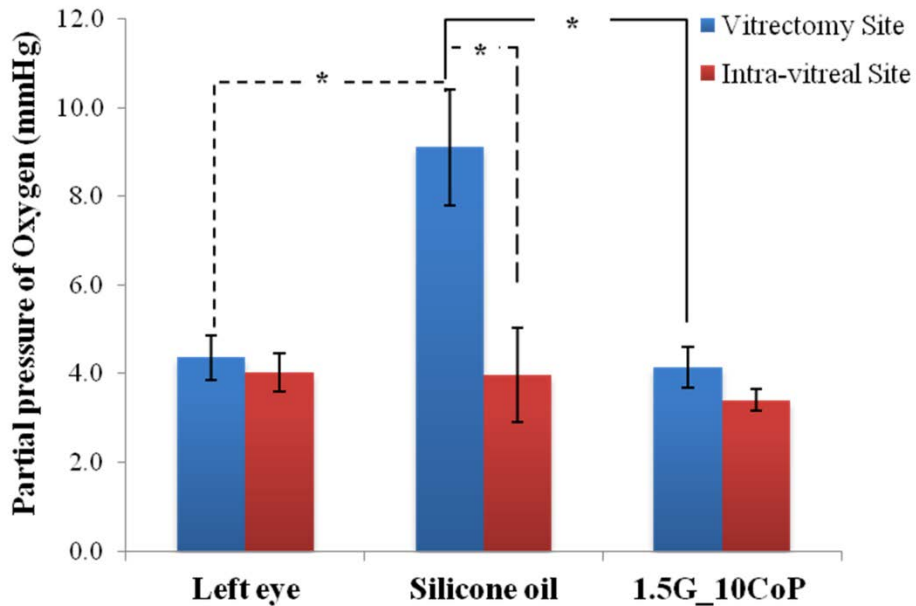


Figure 4.22: Oxygen tension (partial pressure of oxygen (pO_2) in mm Hg) values for different substitutes measured 30 days post-surgery. Data represents the Mean \pm SE. The number of repeats (animals) was 8, 3, and 9 for the left eye, silicone oil and the 1.5G_10CoP hydrogel respectively. At the vitrectomy site, there is a significant increase in pO_2 values for silicone oil compared to the left eye control and the 1.5G_10CoP hydrogel. A significant increase in pO_2 was also observed between the vitrectomy and the intra-vitreous site for rabbits replaced with silicone oil.

The oxygen tension measurements at the vitrectomy site revealed that there was a significant increase in the pO_2 values between the silicone oil and the non-surgical (left eye) control ($p = 0.002$) (Figure 4.22). There was also a significant increase in pO_2 values ($p = 0.04$) between the intra-vitreous and the vitrectomy site for silicone oil. The oxygen tension

measurements for silicone oil suggests that the silicone oil lack the ability to preserve the low oxygen levels compared to the native vitreous after vitrectomy. Due to the uniform medium of the silicone oil, the oxygen distribution is primarily governed by its oxygen solubility, which is 20 times higher than the water [107]. Furthermore, we also found that the oxygen diffusivity ($DO_2 = 4.45E-09 \text{ m}^2/\text{s}$) of silicone oil is higher than water at 38 °C (Refer to Chapter 3, section 3.2.6). The higher oxygen solubility and diffusivity in silicone oil have perhaps caused an increase in the oxygen levels in the rabbit's vitreous cavity. In addition, the reducing agents are usually hydrophilic and are almost insoluble in silicone oil.

The two-component hydrogel, 1.5G_10CoP, maintained the low oxygen level in the vitreous cavity, without any significant increase ($p = 0.75$), compared to the non-surgical control (Left eye). There were also no significant difference ($p = 0.19$) in the pO_2 values between the vitrectomy and the intra-vitreous site (Figure 4.22) for the hydrogel 30 days post-surgery. In the intact hydrogel, the oxygen distribution is primarily governed by diffusion of oxygen through the solvent through a tortuous path developed due to the cross-linked polymeric chains. The oxygen diffusivity in hydrogel ($DO_2 = 1.8E-09 \text{ m}^2/\text{s}$) is also lower than those of the silicone oil and BSS. Therefore, the results suggests the potential of 1.5G_10CoP hydrogel to preserve the low oxygen environment in the vitreous cavity after vitrectomy; however, further measurements after longer durations in fully vitrectomized animal eyes that are replaced with our hydrogels are needed.

4.3 Conclusions

The two-component hydrogels, 0.9G_12CoP and 1.5G_10CoP, that most closely matched the properties of the native vitreous were evaluated for its biocompatibility in contact with different ocular cell lines, and in rabbit eyes. Both the hydrogels were biocompatible *in vitro* with ppRPE, ARPE-19, retinal Müller (rMC-1) cells, and fibroblast 3T3/NIH cells. The

hydrogels did not impair tight junction formation or affect proliferation of the cells. Furthermore, both the hydrogels did not degrade *in vitro* for about four weeks in contact with enzymes and with ppRPE cells. The hydrogels were well tolerated by the rabbit's eye and were non-toxic to the retina for at least 30 days. In addition, both the hydrogels overcome the limitations of silicone oil and has comparable *in vivo* biocompatibility, hence proving to be superior to the clinically accepted current substitute. The hydrogel, 1.5G_10CoP, maintained the low oxygen environment in the rabbit's vitreous cavity for over 30 days, and their oxygen levels were comparable to that of the native vitreous. Both the hydrogel formulations, 0.9G_12CoP and 1.5G_10CoP, are recommended for a six-month evaluation as an artificial vitreous, preferably in mini-pigs.

Chapter 5: Conclusions and Recommendations

Current substitutes are not based on the physiological-properties of the vitreous, and consequently provide no insight into developing better and more physiologically similar prostheses. An ideal substitute would bio-mimic the properties of the native vitreous and performs its essential physiological functions. Inspired by the macromolecular design and composition of the native vitreous, we developed an injectable two-component hydrogel composed of fibrillary gellan (analogous to fibrillary collagen) and polyelectrolyte poly[methacrylamide-co-(methacrylic acid)] (analogous to HA), both endowed with thiol groups. Gellan, in the polymeric mixture, instantaneously transitions from a random coil to a helical structure upon cooling to physiological temperature, and physically traps the semi-flexible copolymer network. Within hours, the thiols in the physically-crosslinked gel oxidize to form mixed disulfide covalent bonds and establish a permanent hydrogel of two dissimilar networks.

Eleven different formulations of this hydrogel, with water contents ranging from 98.6 to 99.5% (vol), gelled instantaneously at low total concentrations of the two polymer components ranging from 5.5 mg/mL to 17.5 mg/mL. Similar to the native vitreous, these hydrogels were optically clear, with refractive indexes ranging from 1.334 to 1.338, densities from 1.002 to 1.009 g/cm³, and optical transmittance greater than 85%. The gels were also viscoelastic solids with mechanical characteristics similar to the vitreous. They swell in physiological fluid and produce osmotic swelling pressure, which is the driving force to re-attach the retina of the eye.

The phase-transition, mechanical, and osmotic swelling properties of this two-component polymeric system were a function of the degree of thiolation, and the concentration of each

component in the mixture. Although both the components are significant in controlling the properties, for a constant degree of thiolation, the sol-gel phase transition properties and the stiffness (the elastic component) of the hydrogels were governed primarily by the concentration of thiolated gellan, while the swelling capacity (the viscous element) was influenced by the concentration of the copolymer.

Interestingly, we found the two-component hydrogel exhibited controlled swelling in physiological solution, where the higher swelling capacity of the copolymer, due to its added charge density, was restricted by the minimally swellable fibrillary gellan network. The behavior resulted in a tightly swollen network with the capacity to produce a significant Donnan swelling pressure. The swelling pressure exerted by the hydrogel was initially regulated by varying the concentration of each component, and later by varying the volume ratio of the polymer solution injected into the vitreous cavity to the volume of the native vitreous removed. We believe the controllability of the swelling pressure produced by the hydrogel has greater clinical significance in retinal detachment treatment for people of diverse age groups.

In contrast to swelling in physiological solutions, the hydrogels de-swelled in polymer solutions of certain known osmotic pressures, isotropically compressed the gels. In the presence of an external compressive load, both the components of the hydrogel exerted a combined compressive resistance against the load, which potentially mimics the physiological functions of the native vitreous, such as dampening ocular motion and protecting the eye against injury.

Due to the biomimetic composition and properties of the native vitreous, the hydrogel provides additional insights into the physiology of the vitreous. In the light of our findings on the bio-mimetic hydrogel, we propose that the native vitreous exhibits controlled swelling behavior and produces Donnan swelling pressure, similar to the biomimetic substitute. The

swelling force exerted by the HA of the vitreous is counterbalanced by the restraining elastic pressure produced by the minimally swellable collagenous fibers. This tightly swollen vitreous gel exerts a Donnan swelling pressure that may play a central role in stimulating the growth and development of the eye, and securing the retina in position.

Finally, two hydrogel formulations, 0.9G_12CoP, and 1.5G_10CoP, whose properties most closely matched those of the native vitreous, were selected for further evaluations, such as oxygen transport through them, and biocompatibility on cells and rabbits. Judged against current vitreous substitutes, such as BSS and silicone oil, both the hydrogels had significantly lower oxygen diffusivity coefficients. The 1.5G_10CoP hydrogel had lower oxygen solubility and further delayed the diffusion of oxygen compared to 0.9G_12CoP hydrogel.

Both the hydrogels were biocompatible *in vitro* in contact with various ocular cell lines, such as ocular epithelial cells (ppRPE, ARPE-19), retinal Müller cells (rMC-1), and fibroblast cells (3T3/NIH). The hydrogels did not impair tight junction formation or affect proliferation of the cells. Furthermore, both the hydrogel did not degrade *in vitro* for about four weeks in contact with enzymatic solutions, and with ppRPE cells. Both the hydrogels were well tolerated by the rabbit's eye and were non-toxic to the retina for at least 30 days. The hydrogels preserved the low oxygen environment in the vitreous cavity for 30 days after vitrectomy. Furthermore, the hydrogels overcome the limitations of silicone oil and has comparable *in vivo* biocompatibility, hence proving to be superior to the clinically accepted current substitute.

Two hydrogel formulations are recommended for further evaluation as an artificial vitreous in a mini-pig model eye. Moreover, the formulations of the two-component hydrogel mimic the macromolecular components of soft tissues, and can be adjusted to approximate their

properties. The two-component hydrogels are suggested as a biomimetic replacement of other soft tissues, such as articular cartilage, the nucleus pulposus, and the corneal stroma.

References

- [1] B.P. Gloor The Vitreous, in: R.A. Moses , W.M. Hart (Eds.), Adler's Physiology of the Eye - Clinical Application, The CV Mosby Co., St. Louis, 1987, pp. 246-267.
- [2] W. Halfter, S.C. Dong, B. Schurer, C. Ring, G.J. Cole, A. Eller, Embryonic synthesis of the inner limiting membrane and vitreous body, *Investigative Ophthalmology & Visual Science* 46(6) (2005) 2202-2209.
- [3] P.N. Bishop, Structural macromolecules and supramolecular organisation of the vitreous gel, *Progress in Retinal and Eye Research* 19(3) (2000) 323-344.
- [4] J. Sebag, *Vitreous: In Health and Disease*, Springer 2014.
- [5] P.N. Bishop, M.V. Crossman, D. McLeod, S. Ayad, Extraction and characterization of the tissue forms of collagen types II and IX from bovine vitreous, *Biochemical Journal* 299(2) (1994) 497.
- [6] S.M. Smith, D.E. Birk, Focus on Molecules: Collagens V and XI, *Experimental Eye Research* 98(Supplement C) (2012) 105-106.
- [7] E. Balazs Functional anatomy of the vitreous, in: J.E. Duane TA, eds (Ed.), *Biomedical Foundations of Ophthalmology*, J.B. Lippincott Company, Philadelphia, 1987, pp. 1-16.
- [8] D.A. Theocharis, S.S. Skandalis, A.V. Noulas, N. Papageorgakopoulou, A.D. Theocharis, N.K. Karamanos, Hyaluronan and chondroitin sulfate proteoglycans in the supramolecular organization of the mammalian vitreous body, *Connective Tissue Research* 49(3-4) (2008) 124-128.
- [9] D.A. Swann, Chemistry and biology of the vitreous body, *International review of experimental pathology* 22 (1979) 1-64.
- [10] B. Lee, M. Litt, G. Buchsbaum, Rheology of the vitreous body. 1. Viscoelasticity of human vitreous, *Biorheology* 29(5-6) (1992) 521-533.
- [11] H. Weber, G. Landwehr, H. Kilp, H. Neubauer, The mechanical properties of the vitreous of pig and human donor eyes, *Ophthalmic research* 14(5) (1982) 335-343.
- [12] J. Sebag, Age-related changes in human vitreous structure, *Graefe's archive for clinical and experimental ophthalmology* 225(2) (1987) 89-93.
- [13] Y. Shui, N.M. Holekamp, B.C. Kramer, et al., The gel state of the vitreous and ascorbate-dependent oxygen consumption: Relationship to the etiology of nuclear cataracts, *Archives of Ophthalmology* 127(4) (2009) 475-482.

- [14] N.M. Holekamp, The Vitreous Gel: More than Meets the Eye, *American Journal of Ophthalmology* 149(1) 32-36.e1.
- [15] V.N. Reddy, Dynamics of transport systems in the eye. Friedenwald Lecture, *Investigative Ophthalmology & Visual Science* 18(10) (1979) 1000-1018.
- [16] F.A. Bettelheim, T.J.Y. Wang, DYNAMIC VISCOELASTIC PROPERTIES OF BOVINE VITREOUS, *Experimental Eye Research* 23(4) (1976) 435-441.
- [17] R.L. Zimmerman, In vivo measurements of the viscoelasticity of the human vitreous-humor, *Biophysical Journal* 29(3) (1980) 539-544.
- [18] M. Tokita, Y. Fujiya, K. Hikichi, Dynamic viscoelasticity of bovine vitreous body, *Biorheology* 21(6) (1984) 751-756.
- [19] B. Lee, M. Litt, G. Buchsbaum, Rheology of the vitreous body. 2. Viscoelasticity of bovine and porcine vitreous, *Biorheology* 31(4) (1994) 327-338.
- [20] B. Lee, M. Litt, G. Buchsbaum, Rheology of the vitreous body. 3. Concentration of electrolytes, collagen and hyaluronic-acid, *Biorheology* 31(4) (1994) 339-351.
- [21] C.S. Nickerson, H.L. Karageozian, J. Park, J.A. Kornfield, Internal tension: a novel hypothesis concerning the mechanical properties of the vitreous humor, 2005.
- [22] C.S. Nickerson, J. Park, J.A. Kornfield, H. Karageozian, Rheological properties of the vitreous and the role of hyaluronic acid, *J Biomech* 41 (2008) 1840-6.
- [23] K.E. Swindle, P.D. Hamilton, N. Ravi, In situ formation of hydrogels as vitreous substitutes: Viscoelastic comparison to porcine vitreous, *Journal of Biomedical Materials Research Part A* 87A(3) (2008) 656-665.
- [24] J.A. Zimmerlin, J.J. McManus, A.J. Crosby, Cavitation rheology of the vitreous: mechanical properties of biological tissue, *Soft Matter* 6(15) (2010) 3632-3635.
- [25] K. Swindle-Reilly, N. Ravi Designing hydrogels as vitreous substitutes in ophthalmic surgery. , in: T. Charila (Ed.), *Biomaterials and Regenerative Medicine in Ophthalmology*, Woodhead Publishing Ltd., CRC Press, 2010, pp. 339-373.
- [26] B.A. Filas, Q. Zhang, R.J. Okamoto, Y.-B. Shui, D.C. Beebe, Enzymatic Degradation Identifies Components Responsible for the Structural Properties of the Vitreous Body, *Investigative Ophthalmology & Visual Science* 55(1) (2014) 55-63.
- [27] C.S. Nickerson, J. Park, J.A. Kornfield, H. Karageozian, Rheological properties of the vitreous and the role of hyaluronic acid, *Journal of Biomechanics* 41(9) (2008) 1840-1846.
- [28] W. Halfter, U. Winzen, P.N. Bishop, A. Eller, Regulation of Eye Size by the Retinal Basement Membrane and Vitreous Body, *Investigative Ophthalmology & Visual Science* 47(8) (2006) 3586-3594.

- [29] D.C. Beebe, Y.B. Shui, C.J. Siegfried, N.M. Holekamp, F. Bai, Preserve the (intraocular) environment: the importance of maintaining normal oxygen gradients in the eye, *Japanese Journal of Ophthalmology* 58(3) (2014) 225-231.
- [30] R.A. Linsenmeier, R.D. Braun, M.A. McRipley, L.B. Padnick, J. Ahmed, D.L. Hatchell, D.S. McLeod, G.A. Luty, Retinal hypoxia in long-term diabetic cats, *Investigative Ophthalmology & Visual Science* 39(9) (1998) 1647-1657.
- [31] N.M. Holekamp, Y.B. Shui, D.C. Beebe, Vitrectomy surgery increases oxygen exposure to the lens: A possible mechanism for nuclear cataract formation, *American Journal of Ophthalmology* 139(2) (2005) 302-310.
- [32] B.A. Filas, Y.-B. Shui, D.C. Beebe, Computational Model for Oxygen Transport and Consumption in Human Vitreous, *Investigative Ophthalmology & Visual Science* 54(10) (2013) 6549-6559.
- [33] Y.B. Shui, J.J. Fu, C. Garcia, L.K. Dattilo, R. Rajagopal, S. McMillan, G. Mak, N.M. Holekamp, A. Lewis, D.C. Beebe, Oxygen distribution in the rabbit eye and oxygen consumption by the lens, *Investigative Ophthalmology & Visual Science* 47(4) (2006) 1571-1580.
- [34] K. Murali, D. Kang, H. Nazari, N. Scianmarello, E. Cadenas, Y.-C. Tai, A. Kashani, M. Humayun, Spatial Variations in Vitreous Oxygen Consumption, *PLoS ONE* 11(3) (2016) e0149961.
- [35] G.J. Harocopos, Y.B. Shui, M. McKinnon, N.M. Holekamp, M.O. Gordon, D.C. Beebe, Importance of vitreous liquefaction in age-related cataract, *Investigative Ophthalmology & Visual Science* 45(1) (2004) 77-85.
- [36] P. Mahdavi, P.E. Tornambe, Pars Plana Vitrectomy, in: E.D. Rosenberg, A.S. Nattis, R.J. Nattis (Eds.), *Operative Dictations in Ophthalmology*, Springer International Publishing, Cham, 2017, pp. 297-299.
- [37] T.T. Kleinberg, R.T. Tzekov, L. Stein, N. Ravi, S. Kaushal, Vitreous substitutes: a comprehensive review, *Surv Ophthalmol* 56(4) (2011) 300-23.
- [38] F. Baino, Towards an ideal biomaterial for vitreous replacement: Historical overview and future trends, *Acta Biomater* 7(3) (2011) 921-35.
- [39] J.C. Pastor, M.I. Lopez, M.A. Saornil, M.F. Refojo, Intravitreal silicone and fluorosilicone oils - pathological findings in rabbit eyes, *Acta Ophthalmologica* 70(5) (1992) 651-658.
- [40] J.C. Pastor Jimeno, E.R. de la Rua, I. Fernandez Martinez, M.J. del Nozal Nalda, J.B. Jonas, Lipophilic substances in intraocular silicone oil, *American journal of ophthalmology* 143(4) (2007) 707-9.
- [41] J.L. Federman, H.D. Schubert, Complications associated with the use of silicone oil in 150 eyes after retina-vitreous surgery, *Ophthalmology* 95(7) (1988) 870-876.

- [42] M. Nakagawa, M. Tanaka, T. Miyata, Evaluation of collagen gel and hyaluronic acid as vitreous substitutes, *Ophthalmic Research* 29(6) (1997) 409-420.
- [43] S. Suri, R. Banerjee, In vitro evaluation of in situ gels as short term vitreous substitutes, *J Biomed Mater Res A* 79(3) (2006) 650-64.
- [44] K.E. Swindle, N. Ravi, Recent advances in polymeric vitreous substitutes, *Expert Review of Ophthalmology* 2(2) (2007) 255-265.
- [45] J. Chang, Y. Tao, B. Wang, B.-h. Guo, H. Xu, Y.-r. Jiang, Y. Huang, An in situ-forming zwitterionic hydrogel as vitreous substitute, *Journal of Materials Chemistry B* 3(6) (2015) 1097-1105.
- [46] C. Jing, T. Yong, W. Bin, Y. Xiaotong, X. Hong, J. Yan-rong, G. Bao-hua, H. Yanbin, Evaluation of a redox-initiated in situ hydrogel as vitreous substitute, *Polymer* 55(18) (2014) 4627-33.
- [47] Y. Tao, X. Tong, Y. Zhang, J. Lai, Y. Huang, Y.R. Jiang, B.H. Guo, Evaluation of an in situ chemically crosslinked hydrogel as a long-term vitreous substitute material, *Acta Biomater* 9(2) (2013) 5022-30.
- [48] R.C. Pruett, C.L. Schepens, H. Freeman, Collagen vitreous substitute: Ii. preliminary clinical trials, *Archives of Ophthalmology* 91(1) (1974) 29-32.
- [49] C. Schramm, M.S. Spitzer, S. Henke-Fahle, G. Steinmetz, K. Januschowski, P. Heiduschka, J. Geis-Gerstorfer, T. Biedermann, K.U. Bartz-Schmidt, P. Szurman, The cross-linked biopolymer hyaluronic acid as an artificial vitreous substitute, *Invest Ophthalmol Vis Sci* 53 (2012) 613-21.
- [50] W.Y. Su, K.H. Chen, Y.C. Chen, Y.H. Lee, C.L. Tseng, F.H. Lin, An injectable oxidated hyaluronic acid/adipic acid dihydrazide hydrogel as a vitreous substitute, *J Biomater Sci Polym Ed* 22(13) (2011) 1777-97.
- [51] Y. Hong, T.V. Chirila, S. Vijayasekaran, W. Shen, X. Lou, P.D. Dalton, Biodegradation in vitro and retention in the rabbit eye of crosslinked poly(1-vinyl-2-pyrrolidinone) hydrogel as a vitreous substitute, *J Biomed Mater Res* 39(4) (1998) 650-9.
- [52] G. Leone, M. Consumi, M. Aggravi, A. Donati, S. Lamponi, A. Magnani, PVA/STMP based hydrogels as potential substitutes of human vitreous, *Journal of Materials Science-Materials in Medicine* 21(8) (2010) 2491-2500.
- [53] S. Lamponi, G. Leone, M. Consumi, G. Greco, A. Magnani, In Vitro Biocompatibility of New PVA-Based Hydrogels as Vitreous Body Substitutes, *Journal of Biomaterials Science, Polymer Edition* 23(1-4) (2012) 555-575.
- [54] W.J. Foster, H.A. Aliyar, P. Hamilton, N. Ravi, Internal osmotic pressure as a mechanism of retinal attachment in a vitreous substitute, *Journal of Bioactive and Compatible Polymers* 21(3) (2006) 221-235.

- [55] K.E. Swindle-Reilly, M. Shah, P.D. Hamilton, T.A. Eskin, S. Kaushal, N. Ravi, Rabbit study of an in situ forming hydrogel vitreous substitute, *Invest Ophthalmol Vis Sci* 50(10) (2009) 4840-6.
- [56] K.E. Swindle, P.D. Hamilton, N. Ravi, Advancements in the development of artificial vitreous humor utilizing polyacrylamide copolymers with disulfide crosslinkers, *Abstracts of Papers of the American Chemical Society* 231 (2006).
- [57] F. Baino, Towards an ideal biomaterial for vitreous replacement: Historical overview and future trends, *Acta Biomaterialia* 7(3) (2011) 921-935.
- [58] T.T. Kleinberg, R.T. Tzekov, L. Stein, N. Ravi, S. Kaushal, Vitreous Substitutes: A Comprehensive Review, *Survey of Ophthalmology* 56(4) (2011) 300-323.
- [59] X. Su, M.J. Tan, Z. Li, M. Wong, L. Rajamani, G. Lingam, X.J. Loh, Recent Progress in Using Biomaterials as Vitreous Substitutes, *Biomacromolecules* 16(10) (2015) 3093-3102.
- [60] S. Suri, C.E. Schmidt, Photopatterned collagen-hyaluronic acid interpenetrating polymer network hydrogels, *Acta Biomater* 5(7) (2009) 2385-97.
- [61] S. Suri, R. Banerjee, In vitro evaluation of in situ gels as short term vitreous substitutes, *Journal of Biomedical Materials Research Part A* 79A(3) (2006) 650-664.
- [62] K.E. Swindle-Reilly, M. Shah, P.D. Hamilton, T.A. Eskin, S. Kaushal, N. Ravi, Rabbit Study of an In Situ Forming Hydrogel Vitreous Substitute, *Investigative Ophthalmology & Visual Science* 50(10) (2009) 4840-4846.
- [63] M. Annaka, K. Mortensen, M.E. Vigild, T. Matsuura, S. Tsuji, T. Ueda, H. Tsujinaka, Design of an Injectable in Situ Gelation Biomaterials for Vitreous Substitute, *Biomacromolecules* 12(11) (2011) 4011-4021.
- [64] Y. Tao, X. Tong, Y. Zhang, J. Lai, Y. Huang, Y.-R. Jiang, B.-H. Guo, Evaluation of an in situ chemically crosslinked hydrogel as a long-term vitreous substitute material, *Acta Biomaterialia* 9(2) (2013) 5022-5030.
- [65] R.K. Balachandran, V.H. Barocas, Contribution of saccadic motion to intravitreal drug transport: theoretical analysis, *Pharm Res* 28(5) (2011) 1049-64.
- [66] M. Annaka, K. Mortensen, M.E. Vigild, T. Matsuura, S. Tsuji, T. Ueda, H. Tsujinaka, Design of an injectable in situ gelation biomaterials for vitreous substitute, *Biomacromolecules* 12 (2011) 4011-21.
- [67] H. Barth, S. Crafoord, S. Andréasson, F. Ghosh, A cross-linked hyaluronic acid hydrogel (Healaflo®) as a novel vitreous substitute, *Graefe's Archive for Clinical and Experimental Ophthalmology* 254(4) (2016) 697-703.

- [68] K. Hayashi, F. Okamoto, S. Hoshi, T. Katashima, D.C. Zujur, X. Li, M. Shibayama, E.P. Gilbert, U.-i. Chung, S. Ohba, T. Oshika, T. Sakai, Fast-forming hydrogel with ultralow polymeric content as an artificial vitreous body, *1* (2017) 0044.
- [69] J. Liang, J. Struckhoff, H. Du, P. Hamilton, N. Ravi, Synthesis and Characterization of In Situ Forming Anionic Hydrogel as Vitreous Substitute, *Journal of Biomedical Materials Research Part B: Applied Biomaterials* (2016).
- [70] Q. Gao, S. Mou, J. Ge, C.h. To, Y. Hui, A. Liu, Z. Wang, C. Long, J. Tan, A new strategy to replace the natural vitreous by a novel capsular artificial vitreous body with pressure-control valve, *Eye* 22(3) (2008) 461-468.
- [71] J. Chen, Q. Gao, Y. Liu, J. Ge, X. Cao, Y. Luo, D. Huang, G. Zhou, S. Lin, J. Lin, C.H. To, A.W. Siu, Evaluation of morphology and functions of a foldable capsular vitreous body in the rabbit eye, *Journal of Biomedical Materials Research Part B-Applied Biomaterials* 97B(2) (2011) 396-404.
- [72] P. Wang, Q. Gao, Z. Jiang, J. Lin, Y. Liu, J. Chen, L. Zhou, H. Li, Q. Yang, T. Wang, Biocompatibility and retinal support of a foldable capsular vitreous body injected with saline or silicone oil implanted in rabbit eyes, *Clinical & Experimental Ophthalmology* 40(1) (2012) e67-e75.
- [73] S. Feng, H. Chen, Y. Liu, Z. Huang, X. Sun, L. Zhou, X. Lu, Q. Gao, A novel vitreous substitute of using a foldable capsular vitreous body injected with polyvinylalcohol hydrogel, *Scientific reports* 3 (2013).
- [74] H. Chen, S. Feng, Y. Liu, Z. Huang, X. Sun, L. Zhou, X. Lu, Q. Gao, Functional evaluation of a novel vitreous substitute using polyethylene glycol sols injected into a foldable capsular vitreous body, *Journal of Biomedical Materials Research Part A* 101(9) (2013) 2538-2547.
- [75] A. Rozier, C. Mazuel, J. Grove, B. Plazonnet, Functionality testing of gellan gum, a polymeric excipient material for ophthalmic dosage forms, *International Journal of Pharmaceutics* 153(2) (1997) 191-198.
- [76] J. Liang, J. Struckhoff, H. Du, P. Hamilton, N. Ravi, Synthesis and Characterization of In Situ Forming Anionic Hydrogel as Vitreous Substitute, *Journal of Biomedical Materials Research Part B* (in press).
- [77] S. Santhanam, J. Liang, J. Struckhoff, P.D. Hamilton, N. Ravi, Biomimetic hydrogel with tunable mechanical properties for vitreous substitutes, *Acta Biomaterialia* 43 (2016) 327-337.
- [78] T.W. Thannhauser, Y. Konishi, H.A. Scheraga, Analysis for disulfide bonds in peptides and proteins, *Methods Enzymol* 143 (1987) 115-9.
- [79] G.L. Ellman, Tissue sulfhydryl groups, *Archives of Biochemistry and Biophysics* 82(1) (1959) 70-77.

- [80] S. Matsukawa, Z. Tang, T. Watanabe, Hydrogen-bonding behavior of gellan in solution during structural change observed by ¹H NMR and circular dichroism methods, *Physical Chemistry and Industrial Application of Gellan Gum* (1999) 15-24.
- [81] A.P. Gunning, A.R. Kirby, M.J. Ridout, G.J. Brownsey, V.J. Morris, Investigation of gellan networks and gels by atomic force microscopy, *Macromolecules* 29(21) (1996) 6791-6796.
- [82] D.F. Coutinho, S.V. Sant, H. Shin, J.T. Oliveira, M.E. Gomes, N.M. Neves, A. Khademhosseini, R.L. Reis, Modified Gellan Gum hydrogels with tunable physical and mechanical properties, *Biomaterials* 31(29) (2010) 7494-7502.
- [83] J.T. Oliveira, T.C. Santos, L. Martins, R. Picciochi, A.P. Marques, A.G. Castro, N.M. Neves, J.F. Mano, R.L. Reis, Gellan Gum Injectable Hydrogels for Cartilage Tissue Engineering Applications: In Vitro Studies and Preliminary In Vivo Evaluation, *Tissue Engineering Part A* 16(1) (2010) 343-353.
- [84] J. Silva-Correia, J.M. Oliveira, S.G. Caridade, J.T. Oliveira, R.A. Sousa, J.F. Mano, R.L. Reis, Gellan gum-based hydrogels for intervertebral disc tissue-engineering applications, *Journal of Tissue Engineering and Regenerative Medicine* 5(6) (2011) E97-E107.
- [85] H. Du, P. Hamilton, M. Reilly, N. Ravi, Injectable in situ Physically and Chemically Crosslinkable Gellan Hydrogel, *Macromolecular Bioscience* 12(7) (2012) 952-961.
- [86] S. Santhanam, J. Liang, R. Baid, N. Ravi, Investigating thiol-modification on hyaluronan via carbodiimide chemistry using response surface methodology, *Journal of Biomedical Materials Research Part A* 103(7) (2015) 2300-2308.
- [87] J. Liang, J.J. Struckhoff, H. Du, P.D. Hamilton, N. Ravi, Synthesis and characterization of in situ forming anionic hydrogel as vitreous substitutes, *Journal of Biomedical Materials Research Part B: Applied Biomaterials* (2016) n/a-n/a.
- [88] J.P. Urban, J.F. McMullin, Swelling pressure of the intervertebral disc: influence of proteoglycan and collagen contents, *Biorheology* 22(2) (1985) 145-57.
- [89] Y. Shi, D. Xiong, Y. Liu, N. Wang, X. Zhao, Swelling, mechanical and friction properties of PVA/PVP hydrogels after swelling in osmotic pressure solution, *Materials Science and Engineering: C* 65 (2016) 172-180.
- [90] F. Horkay, J. Magda, M. Alcoutlabi, S. Atzet, T. Zarembinski, Structural, mechanical and osmotic properties of injectable hyaluronan-based composite hydrogels, *Polymer (Guildf)* 51(19) (2010) 4424-4430.
- [91] H. Vink, Precision measurements of osmotic pressure in concentrated polymer solutions, *European Polymer Journal* 7(10) (1971) 1411-1419.
- [92] N.O. Chahine, F.H. Chen, C.T. Hung, G.A. Ateshian, Direct Measurement of Osmotic Pressure of Glycosaminoglycan Solutions by Membrane Osmometry at Room Temperature, *Biophysical Journal* 89(3) (2005) 1543-1550.

- [93] P.A. Ramachandran, *Advanced Transport Phenomena: Analysis, Modeling, and Computations*, Cambridge University Press 2014.
- [94] A. Karimi, R. Razaghi, M. Navidbakhsh, T. Sera, S. Kudo, Quantifying the injury of the human eye components due to tennis ball impact using a computational fluid–structure interaction model, *Sports Engineering* 19(2) (2016) 105-115.
- [95] P.J. Flory, J. Rehner, Statistical Mechanics of Cross-Linked Polymer Networks II. Swelling, *The Journal of Chemical Physics* 11(11) (1943) 521-526.
- [96] D.J. Lloyd, R.H. Marriott, W.B. Pleass, The swelling of protein fibres. Part I. The swelling of collagen, *Transactions of the Faraday Society* 29(140) (1933) 554-563.
- [97] A. Maroudas, Balance between swelling pressure and collagen tension in normal and degenerate cartilage, *Nature* 260(5554) (1976) 808-809.
- [98] F. Horkay, P.J. Basser, *Osmotic Properties of Cartilage, Biophysics and Biochemistry of Cartilage by NMR and MRI* 2016, pp. 44-61.
- [99] R.W. Hart, R.A. Farrell, Structural theory of the swelling pressure of corneal stroma in saline, *The bulletin of mathematical biophysics* 33(2) (1971) 165-186.
- [100] C.S. Nickerson, H.L. Karageozian, J. Park, J.A. Kornfield, Internal tension: A novel hypothesis concerning the mechanical properties of the vitreous humor, *Macromolecular Symposia* 227 (2005) 183-189.
- [101] M. Piccirelli, O. Bergamin, K. Landau, P. Boesiger, R. Luechinger, Vitreous deformation during eye movement, *Nmr in Biomedicine* 25(1) (2012) 59-66.
- [102] H.B. Dowse, S. Norton, B.D. Sidell, The Estimation of the Diffusion Constant and Solubility of O₂ in Tissue Using Kinetics, *Journal of theoretical biology* 207(4) (2000) 531-541.
- [103] K. Bhunia, S.S. Sablani, J. Tang, B. Rasco, Non-invasive measurement of oxygen diffusion in model foods, *Food Research International* 89(Part 1) (2016) 161-168.
- [104] C. Penicaud, S. Guilbert, S. Peyron, N. Gontard, V. Guillard, Oxygen transfer in foods using oxygen luminescence sensors: Influence of oxygen partial pressure and food nature and composition, *Food Chemistry* 123(4) (2010) 1275-1281.
- [105] D.L. Wise, G. Houghton, Solubilities and diffusivities of oxygen in hemolyzed human blood solutions, *Biophysical Journal* 9(1) (1969) 36-&.
- [106] R.J. Borg, G.J. Dienes, *An introduction to solid state diffusion*, Elsevier 2012.
- [107] D. Poncelet, R. Leung, L. Centomo, R.J. Neufeld, Microencapsulation of silicone oils within polyamide—polyethylenimine membranes as oxygen carriers for bioreactor oxygenation, *Journal of Chemical Technology & Biotechnology* 57(3) (1993) 253-263.

- [108] V. Compañ, J. San Román, E. Riande, T.S. Sørensen, B. Levenfeld, A. Andrio, Oxygen transport through methacrylate-based hydrogels with potential biological capability, *Biomaterials* 17(12) (1996) 1243-9.
- [109] B. Amsden, Solute diffusion within hydrogels. Mechanisms and models, *Macromolecules* 31(23) (1998) 8382-8395.
- [110] A.G. Ogston, B.N. Preston, J.D. Wells, On the transport of compact particles through solutions of chain-polymers, *The Royal Society*, pp. 297-316.
- [111] S. Santhanam, Y.-B. Shui, J. Struckhoff, B. Karakocak, P. Hamilton, G. Harocopos, N. Ravi, Bioinspired Fibrillary Hydrogel with Controlled Swelling Behavior: Applicability as an Artificial Vitreous, *Biomaterials* (Submitted).
- [112] V.P. Sarthy, S.J. Brodjian, K. Dutt, B.N. Kennedy, R.P. French, J.W. Crabb, Establishment and characterization of a retinal Muller cell line, *Investigative Ophthalmology & Visual Science* 39(1) (1998) 212-216.
- [113] K.A. Toops, L.X. Tan, A. Lakkaraju, A detailed three-step protocol for live imaging of intracellular traffic in polarized primary porcine RPE monolayers, *Exp Eye Res* 124 (2014) 74-85.
- [114] S. Arndt, J. Seebach, K. Psathaki, H.J. Galla, J. Wegener, Bioelectrical impedance assay to monitor changes in cell shape during apoptosis, *Biosensors & Bioelectronics* 19(6) (2004) 583-594.
- [115] J. Wegener, C.R. Keese, I. Giaever, Electric cell-substrate impedance sensing (ECIS) as a noninvasive means to monitor the kinetics of cell spreading to artificial surfaces, *Experimental Cell Research* 259(1) (2000) 158-166.
- [116] I. Giaever, C.R. Keese, A morphological biosensor for mammalian-cells, *Nature* 366(6455) (1993) 591-592.
- [117] M. van Deemter, R. Kuijer, H.H. Pas, R.J. van der Worp, J.M.M. Hooymans, L.I. Los, Trypsin-mediated enzymatic degradation of type II collagen in the human vitreous, *Molecular Vision* 19 (2013) 1591-1599.
- [118] G. Tezel, G.M. Seigel, M.B. Wax, Density-dependent resistance to apoptosis in retinal cells, *Current Eye Research* 19(5) (1999) 377-388.
- [119] F.Q. Pereira, B.S. Bercht, M.G. Soares, M.G. Bittencourt da Mota, J.A. Tadeu Pigatto, Comparison of a rebound and an applanation tonometer for measuring intraocular pressure in normal rabbits, *Veterinary ophthalmology* 14(5) (2011) 321-326.
- [120] J. Mackiewicz, B. Mühlring, W. Hiebl, H. Meinert, K. Maaijwee, N. Kociok, C. Lüke, Z. Zagorski, B. Kirchhof, A.M. Joussem, In Vivo Retinal Tolerance of Various Heavy Silicone Oils, *Investigative Ophthalmology & Visual Science* 48(4) (2007) 1873-1883.

[121] I.A. Barbazetto, J.H. Liang, S. Chang, L. Zheng, A. Spector, J.P. Dillon, Oxygen tension in the rabbit lens and vitreous before and after vitrectomy, *Experimental Eye Research* 78(5) (2004) 917-924.

Appendix A

Response Surface Methodology

Design of Experiments (DoE) is a statistical tool to effectively design the experiments in order to quantitatively identify the relationship of the significant factor(s) that affect the response. Factors are the independent variables that can be changed in an experiment, and the response is the outcome measured from the experiment and is the dependent variable. For this study, the factors were the concentration of thiolated gellan and the copolymer of the two-component hydrogel, and the responses were the refractive index, optical transmittance, density, storage and loss modulus, the degree of swelling of the hydrogel in 1X PBS and PVP solution of 3kPa osmotic pressure. The objectives of this study were: (1) To quantify the relationship between each factor (including their interaction) and the properties of the hydrogel, (2) To determine the optimal formulation of the hydrogel that exhibits properties similar to the native vitreous, and (3) To minimize the number of experimental runs and variability. Varying one-factor-at-a-time results in more number of experimental runs, is time-consuming and expensive, and does not reveal the confounding effect between the factors over the responses. Therefore, we used the multi-variate statistic technique, DoE, to efficiently achieve our primary objectives.

Several designs, such as factorial design, response surface, and mixtures designs, can be used to design the experiments. Factorial designs [1, 2] are useful for pre-screening the process to identify the significant factor(s) from a number of factors that affect the responses. Mixtures designs [3, 4] are useful when independent factors are proportions of different components, which are subjected to a constraint. Response surface designs [5, 6] are beneficial to identify the

relationship between the significant factors and the responses, as well as to determine the optimal point that may satisfy all the criteria in the design space. Design space is the domain where the experiments are performed to investigate the response. Both response surface and mixtures designs are applicable to our study; however, response surface was chosen to obtain the same information in a minimal number of experimental runs.

Response surface design allows one to understand how the factors influence the shape of the response and give a sense of direction. RSM has been extensively used in automobile industries, food science, engineering, physical and biological sciences. Depending on the order of the polynomial design and the application, several RSM designs, such as central composite design, Box-Behnken, and optimal designs, are used to design the experiments. Central composite designs [7-9] are commonly used design for optimizing the response affected by two or three variables. The variables are varied at five different levels, which include the factorial points and the axial points. Box-Behnken design [10, 11] is an efficient design model that selects points from a three-level-factorial design space to estimate the first- and second-order coefficients of the model. Optimal designs are those which allow estimation of a variable with minimal variance. D-optimal [12, 13] is an optimal design of RSM that enables one to obtain maximum information with a minimal number of runs and minimal variance. A D-optimal design of RSM is chosen for this study, whose design development is discussed in the upcoming section A1.

A1 Experimental Design Development

The first step in developing a design is to identify the design space. The design space for this study is constructed by varying the concentration of gellan and the copolymer. Based on our

previous study, the concentration of gellan ([G]) is varied at five different levels (values of a variable) from 0.5 mg/mL to 1.5 mg/mL, and the concentration of copolymer ([CoP]) is varied from 5 to 15 mg/mL at five different levels. Based on the degree of polynomial, different models of experimental design can be investigated. The upcoming sections explain the development of the experimental design, and how each design affects the response, i.e., the transition temperature of the hydrogel.

A1.1 Linear Model

The simplest model of the RSM is based on the linear function. The minimum number of experimental runs is 3 for this design, which pertains to the vertices of the design space. Figure A1 represents the design space of a simple linear model with an additional point. The surface of the response developed based on the linear model should fit the equation given below:

$$y = \beta_0 + \beta_1x_1 + \beta_2x_2 + \varepsilon, \quad \text{[Equation 23]}$$

where y is the response, β_0 , β_1 , and β_2 are the regression coefficients, x_1 and x_2 are the factors, and ε is the error.

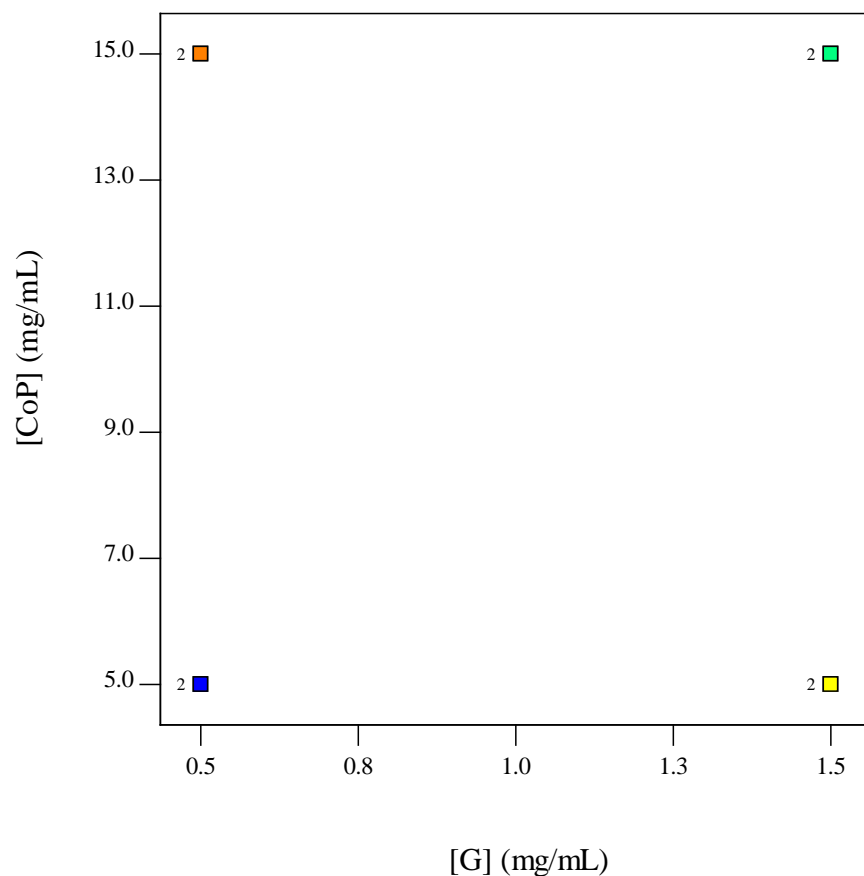


Figure A23: Design space for a linear model of an RSM. Squares represent the formulation, and the number represents the number of repeats at each formulation.

The design space shown in Figure A1 is initially written in terms of coded factors, which are the factors that have a value in terms of levels and not the actual value; high levels have a value of +1, and low levels have a value -1 (Table 1). A multiple regression model analysis is used to identify the quantitative relationship between the factors and the response.

Table A2: The factors and response for a linear model of RSM.

Coded factor	Actual factor	Coded factor	Actual factor	y
x_1	[G]	x_2	[CoP]	(Response: Transition temperature)
(reflects[G])	(mg/mL)	(reflects [CoP])	(mg/mL)	

1	1.5	1	15.0	41.8
1	1.5	-1	5.0	40.0
-1	0.5	1	15.0	40.5
-1	0.5	-1	5.0	35.5
1	1.5	1	15.0	42.5
1	1.5	-1	5.0	39.5
-1	0.5	1	15.0	38.8
-1	0.5	-1	5.0	36.0

The equation 23 is derived from the multiple regression model analysis of the data given in Table 1. Data in Table 1 can be written in its matrix format, $y = X\beta + \varepsilon$, which has a least square solution $\beta = (X'X)^{-1}X'y$. The y is the response matrix, for instance, the average transition temperature of the hydrogel, X is the factor matrix, β is the matrix of regression coefficient, and ε is the error matrix.

$$y = \begin{bmatrix} 42.15 \\ 39.75 \\ 39.65 \\ 35.75 \end{bmatrix} \quad X = \begin{bmatrix} 1 & 1 & 1 \\ 1 & 1 & -1 \\ 1 & -1 & 1 \\ 1 & -1 & -1 \end{bmatrix} \quad \beta = \begin{bmatrix} \beta_0 \\ \beta_1 \\ \beta_2 \end{bmatrix} \quad \varepsilon = \begin{bmatrix} \varepsilon_0 \\ \varepsilon_1 \\ \varepsilon_2 \end{bmatrix}$$

As mentioned before, the least square solution of the matrix equation is calculated as follows:

$$X' = \begin{bmatrix} 1 & 1 & 1 & 1 \\ 1 & 1 & -1 & -1 \\ 1 & -1 & 1 & -1 \end{bmatrix}$$

$$X'X = \begin{bmatrix} 4 & 0 & 0 \\ 0 & 4 & 0 \\ 0 & 0 & 4 \end{bmatrix}$$

The model matrix is orthogonal because the off-diagonal elements of the matrix $X'X$ are zero [6].

Also, the optimality criteria for the D-optimal design are to maximize the $|X'X|$ matrix.

The inverse matrix is given as:

$$(X'X)^{-1} = \begin{bmatrix} 0.25 & 0 & 0 \\ 0 & 0.25 & 0 \\ 0 & 0 & 0.25 \end{bmatrix}$$

The product $X'y$, is calculated to be:

$$X'y = \begin{bmatrix} 157.3 \\ 6.5 \\ 6.3 \end{bmatrix}$$

The regression matrix β is found to be:

$$\beta = (X'X)^{-1}X'y = \begin{bmatrix} 39.33 \\ 1.62 \\ 1.58 \end{bmatrix}$$

The transition temperature (y) can be predicted by substituting the values for β_0 , β_1 , β_2 obtained from the regression matrix into equation 23,

$$y = 39.33 + 1.62x_1 + 1.58x_2 \quad \text{[Equation 24]}$$

The impact of the factors that affect the responses can be identified from the above-coded equation. For instance, the factor x_1 that reflects the variable – concentration of gellan – has a higher impact over the response, transition temperature of the hydrogel, than the concentration of copolymer.

The coded factor equation is then converted to actual values of the factors,

$$y = 32.93 + 3.25 \times [G] + 0.32 \times [CoP]$$

[Equation 25]

The surface response for the above equation is depicted in a 3-D plot as given in Figure A2.

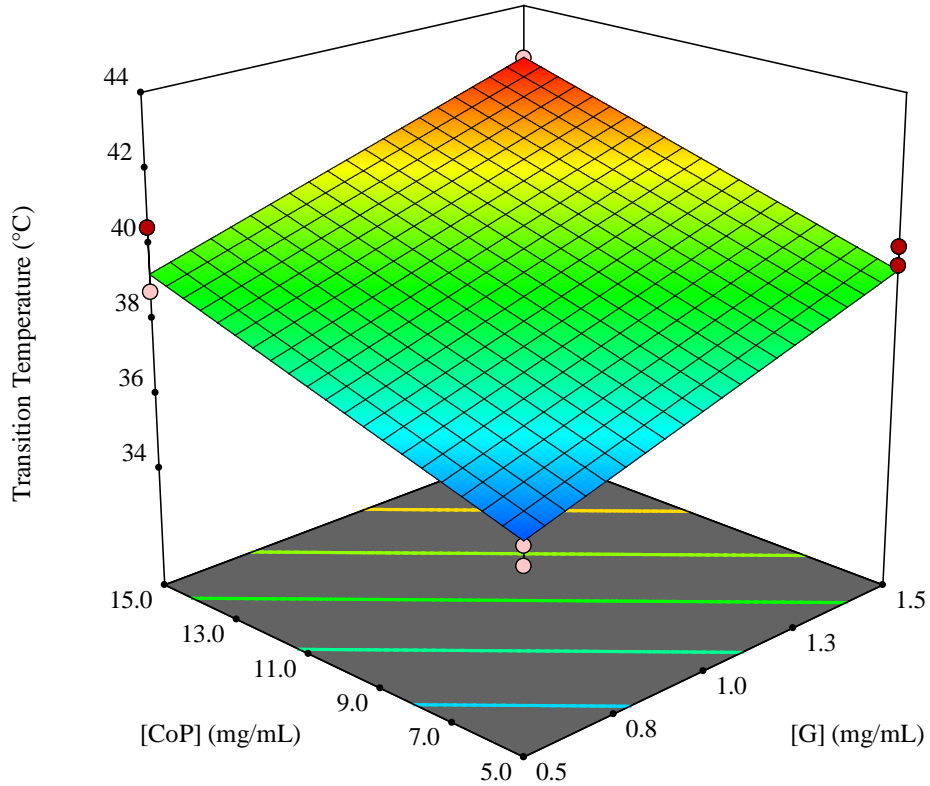


Figure A24: A modeled planar surface plot of sol-gel transition temperature against the concentration of thiolated gellan [G] and copolymer [CoP] in mg/mL.  represents increasing transition temperature from 35.5 to 43 °C.

The linear model of the response is analyzed using analysis of variance (ANOVA), to determine if it's the best fit for the measured experimental data. The Design Expert software from Stat-Ease (version 11) computes the regression equation and analyzes the quality of the fitted surface using ANOVA, normal probability, box-cox analysis, distribution of residuals.

The analysis of variance is a statistical test used to analyze whether the means of two or more groups are equal. Table A2 summarizes the ANOVA analysis for the experimental data

obtained from Design-Expert. Based on the analysis, the modeled surface fits the experimental data significantly with a p-value of 0.0013 and a goodness of fit R^2 of 0.93.

Table A3: ANOVA for a linear model based on coded factors.

Source	Sum of Squares	Degree of freedom (df)	Mean Square	F-value	p-value	Model significance
Model	40.97	2	20.48	33.42	0.0013	significant
A-[G]	21.12	1	21.12	34.46	0.0020	
B-[CoP]	19.85	1	19.85	32.37	0.0023	
Residual	3.07	5	0.6130			
Lack of Fit	1.13	1	1.13	2.32	0.2024	not significant
Pure Error	1.94	4	0.4850			
Cor Total	44.03	7				

The sum of squares, the degree of freedom, and the mean square are calculated using standard formulas described in [14]. The F-test is a characteristic statistical test, which assesses if the model fits the experimental data. The F-value is calculated as the ratio of Mean square of the model to that of the residual. A model F-value of 33.42 implies the model is significant and there is only a 0.13% chance that an F-value this large could occur due to noise. Similarly, a p-value less than 0.05 indicate model terms are significant. In this case, A and B, which reflects [G] and [CoP] respectively are significant model terms. The lack-of-fit test, as the name describes, assesses the lack of fit of the model to that of the experimental data. A Lack of Fit F-

value is calculated as the ratio of Mean square of the lack-of-fit to that of the pure error, which is found to be 2.32. The corresponding p-value is 0.2, indicating that the lack-of-fit is not significant relative to the pure error. The distribution of residuals is analyzed via ANOVA, the normal probability, and box-cox analysis. Minimal is the mean square residual value, better is the design. The normal probability distribution, box-cox, and other residual analysis are described in Appendix B and reference [15].

The linear model is restricted to a planar response surface. Also, this simplest model does not enable one to understand how the interaction between factors affects the response. To understand the interaction effects and the curvatures of the response, higher degree polynomial model has to be constructed.

A1.2 Simple Second-order Model

The simplest second-order model of the RSM is based on a function given in equation 26 that allows one to understand a linear and two-factor-interaction effect over the response. The minimum number of experimental runs is 4 for this design, which pertains to the vertices and the center of the design space (Figure A3). The surface of the response developed based on the model would fit the equation given below:

$$y = \beta_0 + \beta_1x_1 + \beta_2x_2 + \beta_3x_1x_2 + \varepsilon, \quad \text{[Equation 26]}$$

where y is the response, β_0 , β_1 , β_2 , and β_3 are the regression coefficients, x_1 and x_2 are the factors, and ε is the error.

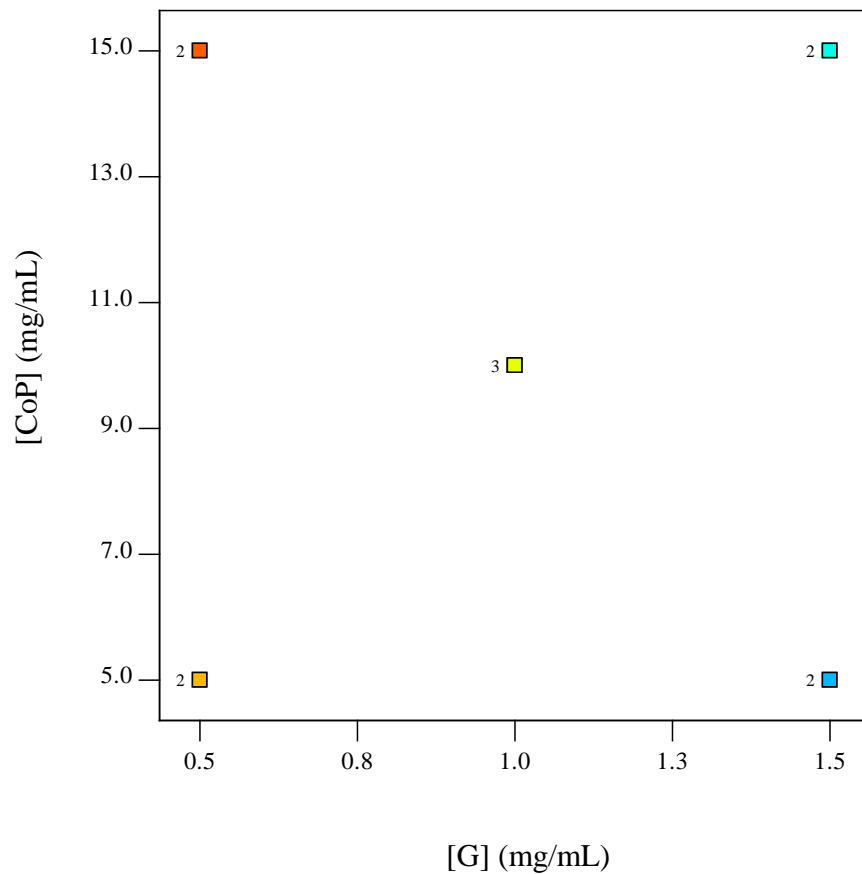


Figure A25: Design space for a simplest second-order model of an RSM. Squares represent the formulation, and the number represents the number of repeats at each formulation.

The 3-D surface developed based on multiple regression analysis of the second-order model is depicted in Figure A4. Similar to the first order model, a planar surface model is still the best fit for the second-order design. The model fits the experimental data with a p-value of 0.0024 and an R^2 of 0.78. The transition temperature of the hydrogel can be predicted using the equation given below:

$$y = 33.45 + 3.25 \times [G] + 0.32 \times [CoP] \quad \text{[Equation 27]}$$

The above equation approximates the equation 25 predicted using first-order model. Both the factors had a significant influence over the transition temperature of the hydrogel.

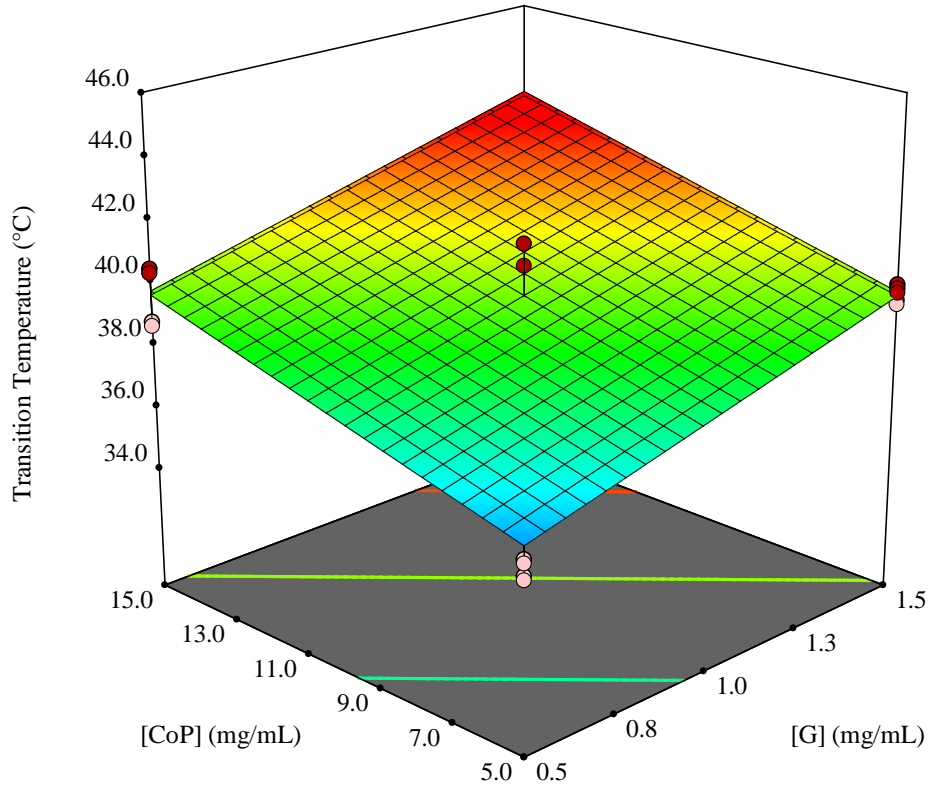


Figure A26: A modeled planar surface plot of sol-gel transition temperature against the concentration of thiolated gellan [G] and copolymer [CoP] in mg/mL.  represents increasing transition temperature from 35.5 to 43 °C.

A1.3 Simple Quadratic Model

A higher-order polynomial allows one to identify the curvature of the response. A simple quadratic model allows understanding the second-degree factorial effect over the response given in equation

$$y = \beta_0 + \beta_1x_1 + \beta_2x_2 + \beta_3x_1x_2 + \beta_4x_1^2 + \beta_5x_2^2 + \varepsilon, \quad \text{[Equation 28]}$$

A simplest quadratic model needs a six minimal experimental runs, which includes points in the center edge, vertices, and center. The vertices and center point account for the factorial effects over response, while the center of edges accounts for the quadratic effects. Figure A5 depicts the

design space made of eight different formulations with repeats. The number of replicates helps to calculate the pure error of the response surface.

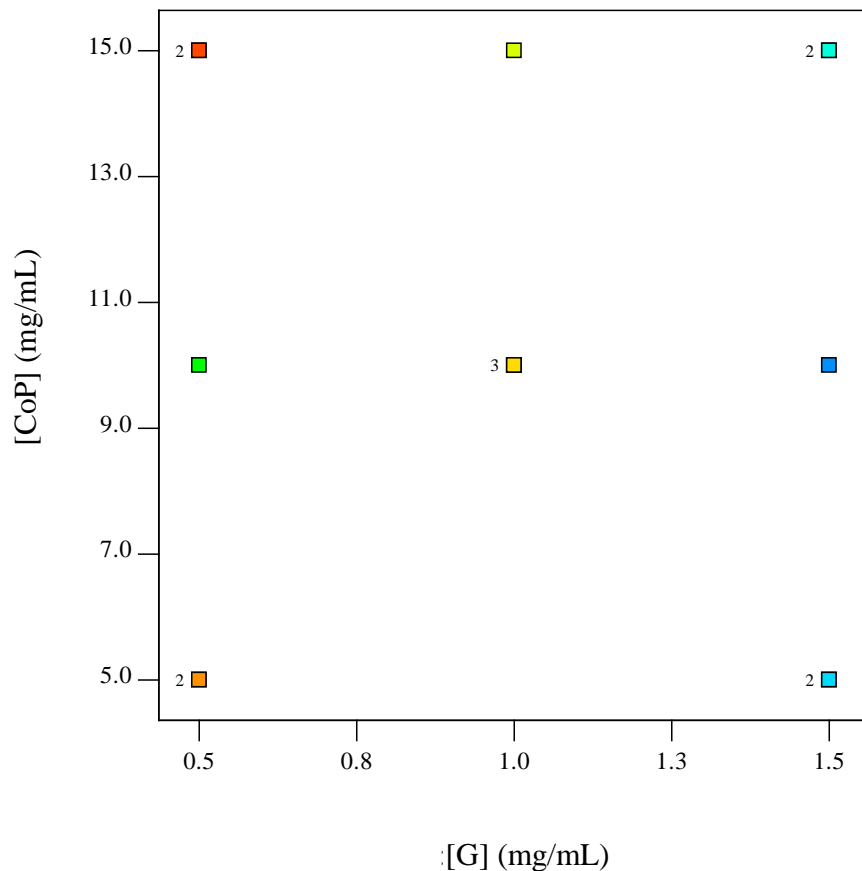


Figure A27: Design space for a simple quadratic model of an RSM. Squares represent the formulation, and the number represents the number of repeats at each formulation.

A quadratic modeled surface was found to be the best for the experimental data (Figure A6). The modeled surface fits the experimental data with a p-value < 0.0001 and an R^2 of 0.95. The regression equation that predicts the transition temperature is given by:

$$y = 25.46 + 20.23 \times [G] + 0.46 \times [CoP] - 0.15 \times [G] \times [CoP] - 7.59 \times [G]^2$$

[Equation 29]

The significant factors that affect the transition temperature were found to be [G], [CoP], and [G]².

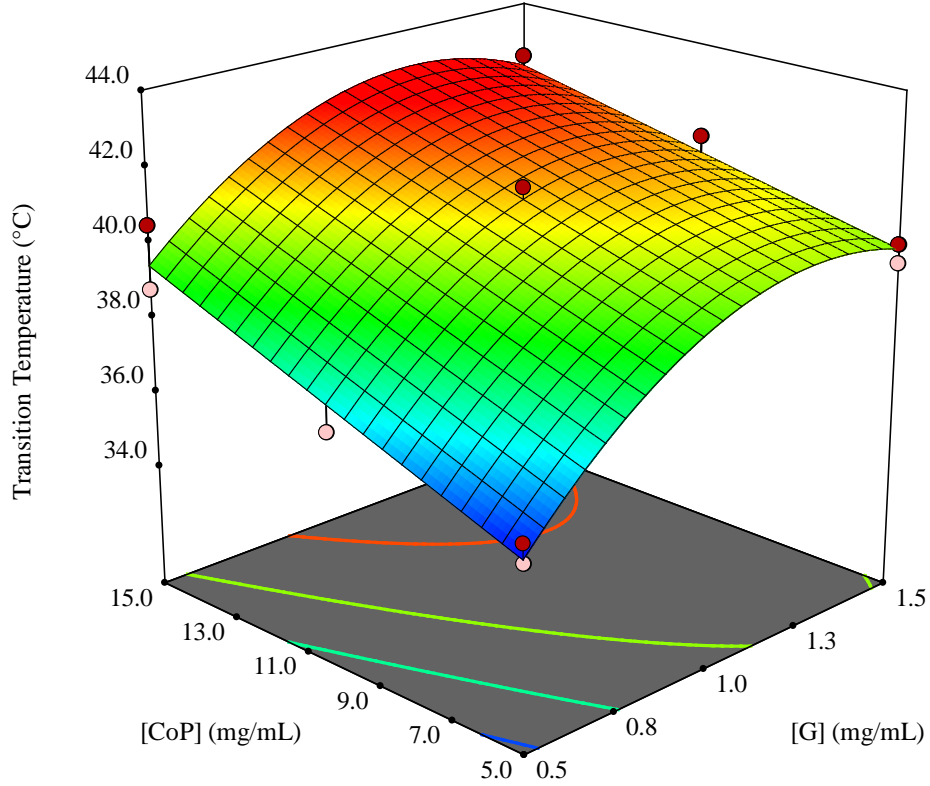


Figure A28: A modeled quadratic surface plot of sol-gel transition temperature against the concentration of thiolated gellan [G] and copolymer [CoP] in mg/mL.  represents increasing transition temperature from 35.5 to 43 °C.

A1.4 Quadratic Model of a D-optimal Design of RSM

A D-optimal design of RSM with additional points based on a quadratic model was designed with 11 different formulations as shown in Figure A7. This design allows one to investigate up-to a third-degree factorial effect over the response as given in equation below:

$$y = \beta_0 + \beta_1x_1 + \beta_2x_2 + \beta_3x_1x_2 + \beta_4x_1^2 + \beta_5x_2^2 + \beta_6x_1^2x_2 + \beta_7x_1x_2^2 + \beta_8x_1^3 + \beta_9x_2^3 + \varepsilon, \quad \text{[Equation 30]}$$

In addition to those described in a simple quadratic model, the experimental points in the design space include the axial check points and interior check points that account for the cubic interaction effects.

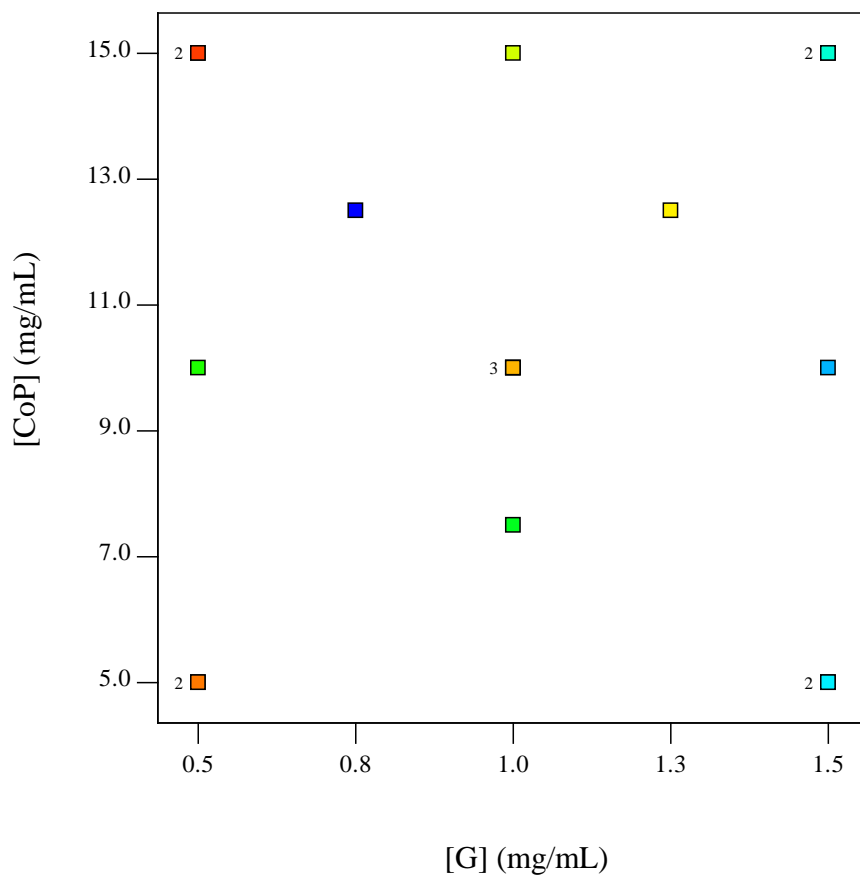


Figure A29: Design space for a quadratic model of a D-optimal RSM design. Squares represent the formulation, and the number represents the number of repeats at each formulation.

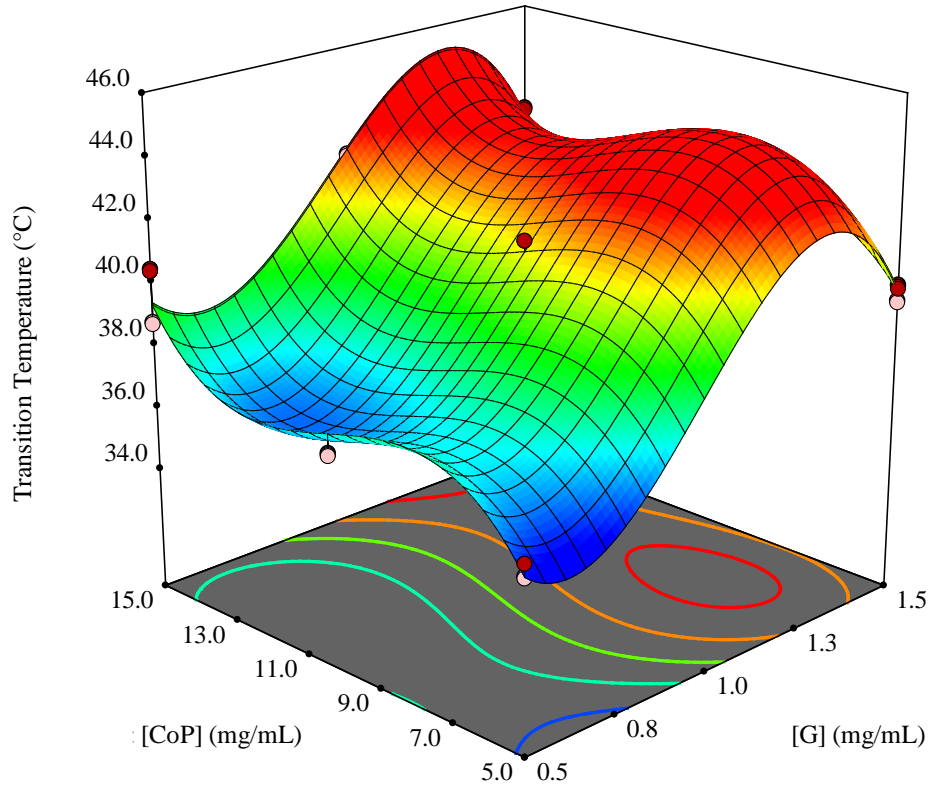


Figure A30: A modeled cubic surface plot of sol-gel transition temperature against the concentration of thiolated gellan and copolymer in mg/mL.  represents increasing transition temperature from 35.5 to 43 °C.

As already mentioned in section 3.2.1, the cubic surface is the best fit for the quadratic model design with a p-value of <0.0001 and an R^2 of 0.97. The cubic equation used to predict the transition temperature is given by:

$$\text{Transition temperature} = 37.40 - 109.40 \times [G] + 8.93 \times [\text{CoP}] - 0.15 \times [G] \times [\text{CoP}] + 133.80 \times [G]^2 - 0.93 \times [\text{CoP}]^2 - 47.12 \times [G]^3 + 0.03 \times [\text{CoP}]^3 \quad [\text{Equation 31}]$$

In order to obtain maximal information from the factorial effects and their interaction over the response, a D-optimal design with additional points was chosen in our study (Refer Chapter 3).

A2 Conclusions

The development of the experimental design from a simple first-order model to a quadratic model was discussed. A simple first-order design model accounts for the effects of factors over the response. A higher-order polynomial model will enable one to fully-understand the effect of the factorial interaction and higher-degree factorial effects over the response. Also, the model may influence the curvatures and shape of the response surface. Therefore, we recommend a D-optimal response surface design made of 11 different formulations with repeats to evaluate the structure-property relationships of the two-component hydrogel. Furthermore, the D-optimal design allows one to precisely predict the optimal formulation that approximates the properties of the native vitreous humor.

References

- [1] G. Vicente, A. Coteron, M. Martinez, J. Aracil, Application of the factorial design of experiments and response surface methodology to optimize biodiesel production, *Industrial crops and products* 8(1) (1998) 29-35.
- [2] J.F.d.M. Burkert, F. Maugeri, M.I. Rodrigues, Optimization of extracellular lipase production by *Geotrichum* sp. using factorial design, *Bioresource technology* 91(1) (2004) 77-84.
- [3] H. Scheffe, The simplex-centroid design for experiments with mixtures, *Journal of the Royal Statistical Society. Series B (Methodological)* (1963) 235-263.
- [4] J.A. Cornell, *Experiments with mixtures: designs, models, and the analysis of mixture data*, John Wiley & Sons 2011.
- [5] R. Mead, D.J. Pike, A Biometrics Invited Paper. A Review of Response Surface Methodology from a Biometric Viewpoint, *Biometrics* 31(4) (1975) 803-851.
- [6] R.H. Myers, D.C. Montgomery, G.G. Vining, C.M. Borrer, S.M. Kowalski, Response surface methodology: a retrospective and literature survey, *Journal of quality technology* 36(1) (2004) 53.
- [7] W. Wu, G. Cui, B. Lu, Optimization of multiple evariables: application of central composite design and overall desirability, *Chinese Pharmaceutical Journal-Beijing-* 35(8) (2000) 530-532.

- [8] M. Ahmadi, F. Vahabzadeh, B. Bonakdarpour, E. Mofarrah, M. Mehranian, Application of the central composite design and response surface methodology to the advanced treatment of olive oil processing wastewater using Fenton's peroxidation, *Journal of Hazardous Materials* 123(1) (2005) 187-195.
- [9] P.A.J. Rosa, A.M. Azevedo, M.R. Aires-Barros, Application of central composite design to the optimisation of aqueous two-phase extraction of human antibodies, *Journal of Chromatography A* 1141(1) (2007) 50-60.
- [10] G. Annadurai, R.Y. Sheeja, Use of Box-Behnken design of experiments for the adsorption of verofix red using biopolymer, *Bioprocess and Biosystems Engineering* 18(6) (1998) 463-466.
- [11] S.L.C. Ferreira, R.E. Bruns, H.S. Ferreira, G.D. Matos, J.M. David, G.C. Brandao, E.G.P. da Silva, L.A. Portugal, P.S. Dos Reis, A.S. Souza, Box-Behnken design: an alternative for the optimization of analytical methods, *Analytica chimica acta* 597(2) (2007) 179-186.
- [12] S.-E. Fang, R. Perera, Damage identification by response surface based model updating using D-optimal design, *Mechanical Systems and Signal Processing* 25(2) (2011) 717-733.
- [13] K.M. Kim, B.S. Kim, D.H. Lee, H. Moon, H.H. Cho, Optimal design of transverse ribs in tubes for thermal performance enhancement, *Energy* 35(6) (2010) 2400-2406.
- [14] M.A. Bezerra, R.E. Santelli, E.P. Oliveira, L.S. Villar, L.A. Escaleira, Response surface methodology (RSM) as a tool for optimization in analytical chemistry, *Talanta* 76(5) (2008) 965-977.
- [15] S. Santhanam, J. Liang, R. Baid, N. Ravi, Investigating thiol-modification on hyaluronan via carbodiimide chemistry using response surface methodology, *Journal of Biomedical Materials Research Part A* 103(7) (2015) 2300-2308.

Appendix B

Investigating Thiol-Modification on Hyaluronan via Carbodiimide Chemistry using Response Surface Methodology

Hyaluronan (HA) is a naturally occurring glycosaminoglycan widely researched for its use as a biomaterial in tissue engineering, drug delivery, angiogenesis, and ophthalmic surgeries. The mechanical properties of this biomaterial can be altered to a required extent by chemically modifying the pendant reactive groups. However, derivatizing these polymers to a predetermined extent has been the Achilles heel for this process. In this study, we investigate the modification of HA in which the carboxyl group, in one of the saccharide groups, is derivatized to an amide containing a thiol group. The derivatization is accomplished by the well-known carbodiimide-based activation [1-3] of the carboxyl group of HA with *N*-(3-Dimethylaminopropyl)-*N'*-ethylcarbodiimide hydrochloride (EDC) and *N*-hydroxysuccinimide (NHS), followed by its reaction with a disulfide-containing amine [1-10]. Based on the details of experimental conditions from several published sources, we focused on identifying the relative effects of various reaction parameters or factors. Using the design of experiments (DoE) statistics, involving fractional factorial design (FF) [11, 12] and response surface methodology (RSM) [13-15], one can effectively design experiments to quantitatively identify the relationship of significant factor(s) that affect the reaction output (response). This enables one to statistically optimize the reaction parameters to yield a desired output, carry out better trade-offs when multiple critical factors are governing the reaction, and minimize variability. In DoE involving

multiple factors, a particular design is chosen based on the number of factors to be tested and the levels over which they vary. In general, the factors affecting the process are initially screened using fractional factorial designs to determine their significance. Two to four key factors are further optimized using RSM to maximize, minimize, or stabilize the response [11, 16, 17].

In this work, we have attempted to identify the relative importance of reaction variables or factors influencing the amidation reaction, and determine the quantitative relationship between the factors and their responses. The five main factors we investigated, using FF design, were the pH, duration of reaction, and the mole ratios of Cys, EDC, and NHS with respect to a repeat unit of HA (disaccharide consisting of glucuronic acid and N-acetyl glucoseamine). The mole ratios of reactants to repeat unit of HA, will be mentioned as moles of reactant. The response was the degree of amidation of HA. We used a D-optimal design of RSM to determine how each factor affected the degree of thiolation of HA and the formation of side products. We optimized the reaction for a pre-determined extent of derivatization with minimal side product. This work uses material from the reference [18]

B1 Materials and Methods

B1.1 Materials

Hyaluronic acid (MW 60 kDa) was purchased from Lifecore Biomedical (Chaska, MN). 1-ethyl-3-(3-dimethylaminopropyl) carbodiimide (EDC), N-hydroxysuccinimide (NHS), cystamine dihydrochloride (Cys), dithiothreitol (DTT), glycine, sodium sulphite, sodium hydroxide, sodium chloride, and ethylenediaminetetraacetic acid were purchased from Sigma Aldrich (St. Louis, MO). The FF and RSM experiments were designed using Design-Expert® software, version 7, Stat-Ease (Minneapolis, MN).

B1.2 Design of Experiments

Selection of factors affecting the reaction

An essential step of planning the factorial process is selecting the factor(s) and their levels of variation. Five main factors affecting the degree of amidation of HA were moles of Cys, EDC and NHS; pH, and duration of the reaction. The other critical factor affecting the reaction was the temperature, which was kept constant at 37 °C. The factors were varied at two levels for FF and five levels for RSM.

Fractional factorial design for screening the significant factors

The experimental design and statistical analysis were carried out in Design-Expert 7.0.0. We chose a two-level fractional factorial design to investigate the factors and screen for the significant variables affecting the response. We chose a design of resolution V in which the main effects were un-confounded, while two-factor interactions were confounded with three-factor interactions (Table B4) in 16 experimental runs ($2^{(5-1)}$). We conducted the experiments in random order to nullify the effect of systematic errors.

Table B4: Alias structure of the 2(5-1) fractional-factorial design

Effect	Factors
[A]	A
[B]	B
[C]	C
[D]	D
[E]	E
[AB]	AB+CDE
[AC]	AC+BDE
[AD]	AD+BCE
[AE]	AE+BCD
[BC]	BC+ADE
[BD]	BD+ACE
[BE]	BE+ACD
[CD]	CD+ABE
[CE]	CE+ABD
[DE]	DE+ABC

D-Optimal design for optimizing the degree of amidation of HA

The relationships between the significant factors obtained from FF analysis, were determined by a two-factor, five-level D-Optimal design with a quadratic model of RSM. A second-order polynomial, was used to calculate the predicted response:

$$Y = b_0 + b_1X_1 + b_2X_2 + b_{11}X_1^2 + b_{22}X_2^2 + b_{12}X_1X_2 \quad \text{[Equation 32]}$$

where Y is the predicted response, X_1 and X_2 are independent variables (factors), b_0 is the intercept, b_1 and b_2 are linear, b_{11} and b_{22} are squared, and b_{12} are interaction effects of the factors. To investigate their effect over the responses, the degree of amidation of HA (Y), the factors, X_1 and X_2 were varied over 5 levels, with different combinations resulting from 16 experiments.

B1.3 Amidation of HA

We did the FF as a single block design. Stock solutions of HA (1% (w/v)); EDC, NHS, and Cys of respective moles at two levels of concentration and pH were prepared. The total reaction volume of the experiment was 5 mL. A required volume of HA repeat unit, EDC, NHS, and Cys was added to 0.5 M MES buffer, and the mixture was maintained at the correct pH in a closed 20-mL glass vial. This was continuously agitated in a shaker at 200 rpm for a required duration at 37°C. The reaction was stopped by adding 1 N NaOH, and the final pH was adjusted to 8-9. Excess EDC, NHS, and Cys were removed from the reaction mixture by dialyzing (MWCO: 6,000-8,000) in deionized (DI) H₂O (thrice). The pH of samples was adjusted to 7.5, and reduced with DTT for 3 h. Excess DTT was removed by dialyzing (semi-permeable membrane of MWCO: 6,000-8,000) in N₂-bubbled 1 mM HCl (six times). The samples were analyzed for the percentage of derivatization of HA with thiols, using a disulfide and an Ellman's test.

The 16 combinations of RSM were performed using the same procedure as specified in FF design.

B1.4 Determination of degree of amidation via disulfide linkage

Using the 2-nitro-5-thiosulfobenzonate (NTSB) assay [19], we determined the total thiol and disulfide content of the derivatized HA before and after reducing with DTT. Briefly, Cys standards of concentrations from 0.05 to 1.5 mM were prepared using a 10 mM Cys stock by serial dilution, using N₂-bubbled DI water. About 900 μL of NTSB solution, prepared as described in the literature [19], was added to 100 μL of the sample and the standards. Because the reactions are photo-activated, assay samples were incubated in the dark for 15 minutes and their absorbance was read with a spectrophotometer at 412 nm.

B1.5 Ellman's reaction

The amount of thiol content was also determined spectrophotometrically, using an Ellman's reagent as described by Ellman [20]. Briefly, we diluted 10 mg of each lyophilized sample with 2 mL of N₂-bubbled water. To 100 μL of this sample, we added 500 μL of 0.1 M phosphate buffer (pH 8), 400 μL of water, and 50 μL of Ellman's reagent. Samples were incubated for 15 min at room temperature, and their absorbance measured at 412 nm in a spectrophotometer. Thiol content was calculated as per the equation given below:

$$SH \text{ (moles)/g of HA} = (Ab/13600) * (V_{total}/V_{sample}) * (1/HA \text{ conc}) \quad \text{[Equation 33]}$$

where Ab is the absorbance and V_{total} is the total volume, while V_{sample} is the sample volume and 13600 is the extinction coefficient. The concentration of the HA ($HA \text{ conc}$) is in mg/mL.

B1.6 Characterization of Amidated HA

The amidated HA was characterized using ^1H NMR spectroscopy. ^1H NMR spectra were obtained on a Varian Unity Inova 500 (Palo Alto, CA). HA samples were dissolved in D_2O (8 mg/mL) with NaOD (20 μmol). Each sample was scanned for 128 times at 25 $^\circ\text{C}$.

B2 Results and Discussion

B2.1 Amidation and Characterization of HA

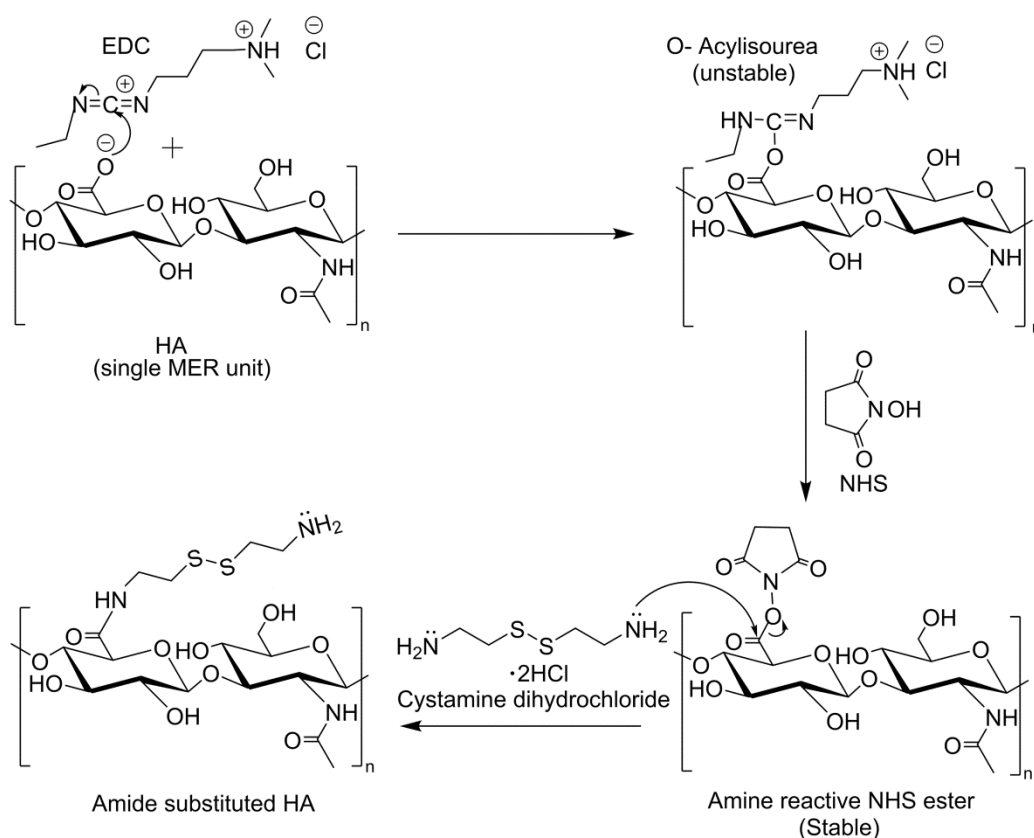


Figure B31: Carbodiimide crosslinking reaction of HA and Cys with EDC and NHS

Derivatization of carboxylic moieties of HA, to an amide containing thiol group with cystamine dihydrochloride via carbodiimide crosslinking chemistry, proceeds as described in Figure B1. Mechanistically, the negatively charged carboxylate group attacks the electron-deficient diimide carbon atom on the carbodiimide molecule (EDC) to form the activated O-

acylisourea intermediate. The result is that the carbon atom of the HA carboxylate group becomes sufficiently electron-deficient to be susceptible to nucleophilic attack by the lone pair of electrons on the amine group of the Cys, thereby forms an amide-substituted HA molecule and acylurea. The O-acylisourea, which is very unstable, is usually stabilized by substituting it with NHS while maintaining it in an active form.

Several investigators [1-4] have derivatized HA through this mechanism; however, these procedures did not describe the quantitative relationship needed for optimization between the reactants and the degree of thiolation. Sehgal [5] optimized the reaction conditions one factor at a time to link monovalent butyric acid over Affi-gel 102 with the use of EDC and NHS. These studies showed the significance of NHS for better yield of products, as well as the advantage of an MES buffer rather than a phosphate buffer. The experiments were carried out over a range of carboxylic acid:amine mole ratios with a maximum of 1:15; EDC:NHS mole ratios with a maximum of 15:1; pH of 3 to 8; and a duration of 1-24 h. Kafedjiiski [1] focused on synthesizing a novel HA-cysteine ethyl ester conjugate mediated by EDC and NHS. The experiments were performed at pH 5.5 for 4 h with varying EDC:NHS ratios. Similarly, Cao [6] analyzed the mechanical stability of collagen-chondroitin sulfate scaffolds with various EDC concentrations. The experiments were carried out for about 4 h in MES buffer for various concentrations of EDC with a constant EDC:NHS ratio of 4:1. In the literature, the duration of the crosslinking reaction has varied from 1 h to 24 h, with the majority being around 4 h [7-9]. Sehgal [5] observed that the percentage of coupling plateaued beyond 6 h. Most investigators used a pH of 4.5 to 6.5; while the majority used a pH of 5 [9, 10].

Table B5: The experimental condition (factors) and thiol content (response) obtained from a disulfide test for each experiment using FF design.

Run	Factor A: Cystamine	Factor B: pH	Factor C: NHS	Factor D: EDC	Factor E: Time	Response: Thiol content
-----	------------------------	--------------	---------------	---------------	----------------	----------------------------

	(moles)		(moles)	(moles)	(hours)	(in % of derivatization of HA)
13	0.1	4.5	0.1	1	6	0.27
3	10	4.5	0.1	1	1	0.77
11	0.1	6.5	0.1	1	1	3.73
5	10	6.5	0.1	1	6	10.22
2	0.1	4.5	1	1	1	0.28
14	10	4.5	1	1	6	0.35
4	0.1	6.5	1	1	6	6.28
15	10	6.5	1	1	1	19.55
10	0.1	4.5	0.1	15	1	4.67
6	10	4.5	0.1	15	6	29.28
8	0.1	6.5	0.1	15	6	5.44
9	10	6.5	0.1	15	1	17.16
7	0.1	4.5	1	15	6	5.05
16	10	4.5	1	15	1	13.89
12	0.1	6.5	1	15	1	5.01
1	10	6.5	1	15	6	22.21

We analyzed the dependence of these factors on one-another by designing experiments using FF design varying at two levels whose limits were chosen based on the literature (Table B5). The final product of the reaction, amide-substituted HA, was reduced with DTT, purified with DI water free of oxygen (achieved through nitrogen bubbling) at acidic pH, and lyophilized to obtain a white fluffy, fibrous solid. The degree of thiolation of the derivatized HA was determined, using the disulfide test and Ellman's test. The disulfide test measures both thiol and disulfide content in the sample, and the Ellman's test measures only the thiol content. The results from Ellman's test are 30%-50% lower than the disulfide test results. This is because

HA-SH is partially oxidized to disulfide, during the purification process. Hence, the disulfide test results were chosen for statistical analysis.

B2.2 Fractional factorial design

Determination of significant factors from FF design

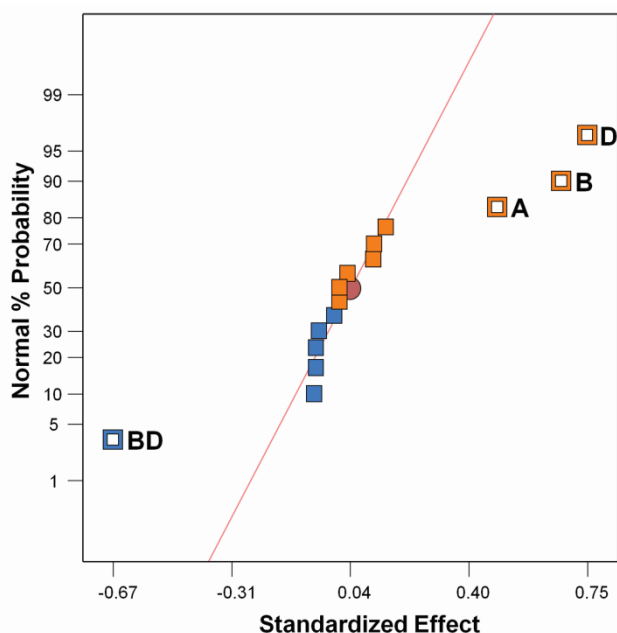


Figure B32: Normal probability plot of the effects of the factors and their interactions. Effect of single factors is represented by A, B, C, D, E; their interactions with other variables are represented as AB, BC, etc. In this figure, A- Cys; B- pH; D- EDC; BD- two factorial interaction of pH and EDC. ■ represents positive effects; while ■ represents negative effects. The model is framed based on selecting the dominant factors that are highlighted, and labeled in plots; other factors are considered as errors.

The response from the disulfide test for FF design (Table 5) varied from a minimum of 0.27% to a maximum of 29.28% with a mean of 9.01% and standard deviation of 8.59%. We identified significant factors from the normal probability plot by choosing those factors that fall away from the standard line (Figure B2). The normal probability plot shows that the single factors EDC, the pH of the reaction medium, and Cys have a positive effect on the response, while the two-factor interaction between pH and EDC has a negative effect. Also, the Pareto diagram gives the contribution of each factor, which is useful in selecting the factors (Figure

B3(a)). Having selected the important factors, we determined the need for transformation of data based on value of the ratio of maximum over minimum response. Generally, the response ratio above 10 may require a transformation, while a ratio below 3 may not need transformation. In our design, for a high response ratio of 108.4, we needed a log transformation, which is confirmed by the Box-Cox plot of power transforms (Figure B3(b)).

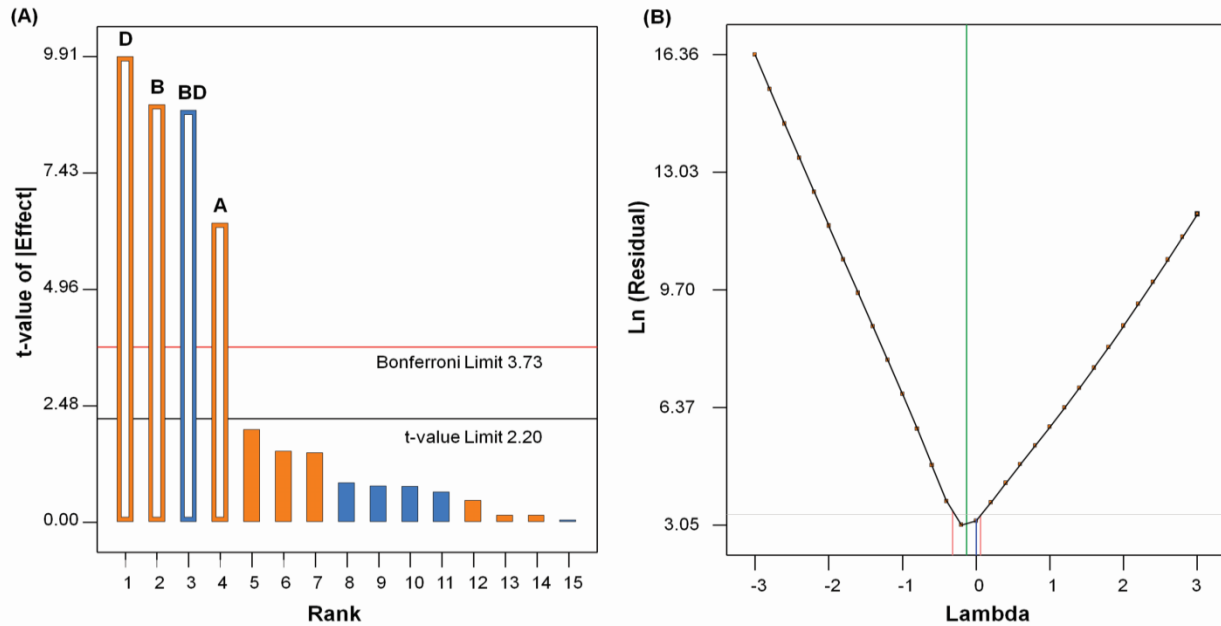


Figure B33: (a) Pareto chart representing the effect of each factor over response variable in the descending order from greatest to lowest contribution for FF design. Bonferroni limit is the threshold where the effect emerging above this limit are significant. T limit is the threshold where the effect emerging above this but below Bonferroni limit may possibly be significant. Effects D, B, BD, A are significant. b) Box-Cox plot of power transforms representing the required transformation of data for FF design. In this figure, blue line represents lambda current = 0; green line is best lambda current = -0.13. The recommended transform is Log transformation with lambda = 0.

The quality of the fitted model was evaluated by analysis of variance (ANOVA), a statistical method for making simultaneous comparisons between two or more means. It yields values that are analyzed for the existence of a significant relationship between the variables. In this study, we found the fitted model to be highly significant, with a determination coefficient (R^2) of 0.96. Also, the predicted R^2 of 0.92 was in reasonable agreement with the adjusted R^2 of 0.95. The F-test assesses whether any of the effect of factors on response is, on average, superior

or inferior to the others versus the null hypothesis, which considered all factors to yield the same mean response. The *p-value* helps to assess if the main effect of each factor is statistically significant ($p < 0.05$) or marginally significant ($p < 0.1$).

Table B6: Table representing the experimental conditions (factors) and thiol content (response) obtained from disulfide tests for each experiment using response-surface design

Run	Factor A: EDC (moles)	Factor B: Amine (moles)	Response: Thiol Content (in % of Derivatization of HA)
16	0.5	0.5	6.80
3	10	0.5	15.74
14	0.5	10	7.61
12	10	10	27.5
10	5.25	10	22.52
4	10	5.25	26.33
5	5.25	2.88	23.95
11	0.5	5.25	5.52
15	2.88	7.63	25.89
7	7.63	7.63	37.12
9	5.25	0.5	21.47
8	0.5	0.5	6.82
13	10	0.5	24.87
2	0.5	10	7.65
1	10	10	34.50
6	10	5.25	36.34

The Model F value of 73.67 and *p-value* of < 0.0001 indicates that the model is significant (Table B4). There is only a 0.01% chance that a Model F-value this large could occur

due to noise. Thus, the significant factors influencing the response from FF design are EDC, pH of the reaction medium, Cys, and interaction between EDC and pH.

Table B7: Model Summary Statistics of the FF and RSM Models

Models	F-value	p-value	R ²	Adjusted R ²	Predicted R ²	Adequate Precision
FF	73.67	< 0.0001	0.96	0.95	0.92	22.51
RSM- Thiol Content	39.43	< 0.0001	0.91	0.88	0.84	14.79
RSM- Side reaction	56.09	< 0.0001	0.92	0.90	0.87	14.37

Diagnostic plots of residuals

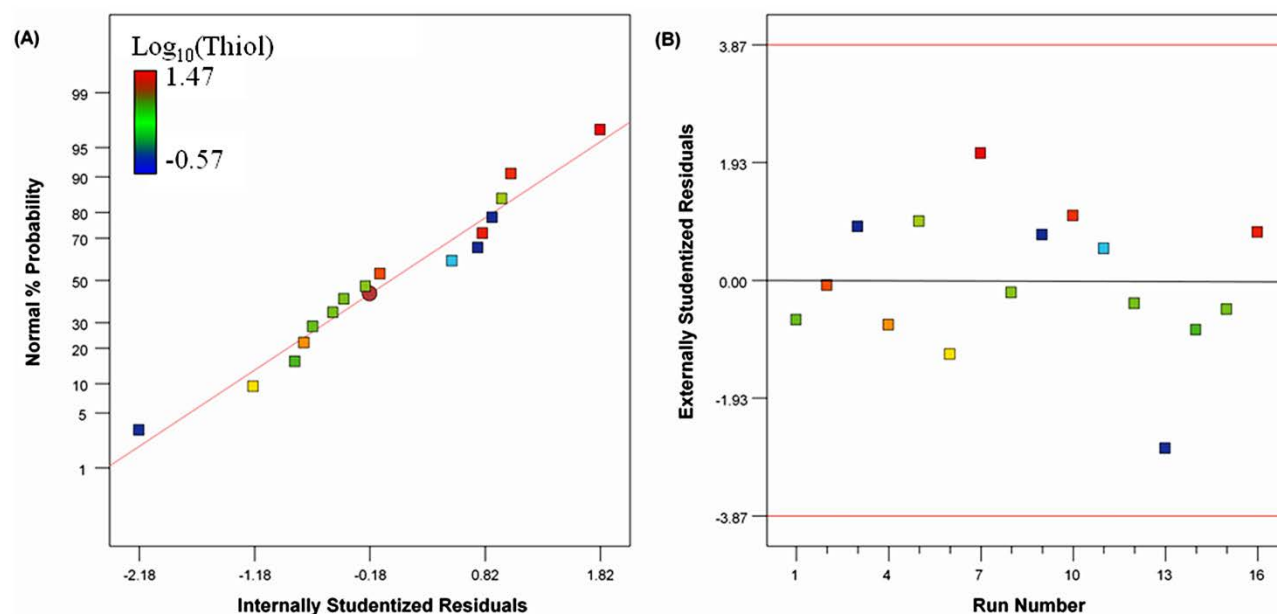


Figure B34: Residual analysis of the FF design. (a) Plot of normal probability of residuals and (b) Plot of external studentised residuals with each run.

While the ANOVA emphasizes the significance of the chosen model of contributory factors over the response, the distribution of residuals, which are the difference between the predicted and observed values, is also a crucial part to be examined. The normal probability plot

of residuals helps us assess how closely the observed values follow the theoretical distribution, which was indicated by a straight line showing normal distribution (Figure B4(a)). The externally studentized residual is the plot of residuals versus run, which tests whether the run in question is consistent with the rest of the data for this model. This helps to determine the outliers, and whether there is a need to investigate them. For this model, the residuals are uniformly distributed for each run (Figure B4(b)), and lie within the control limits, thereby indicating the run is consistent with the rest of the data.

Plots of dominant effects on response

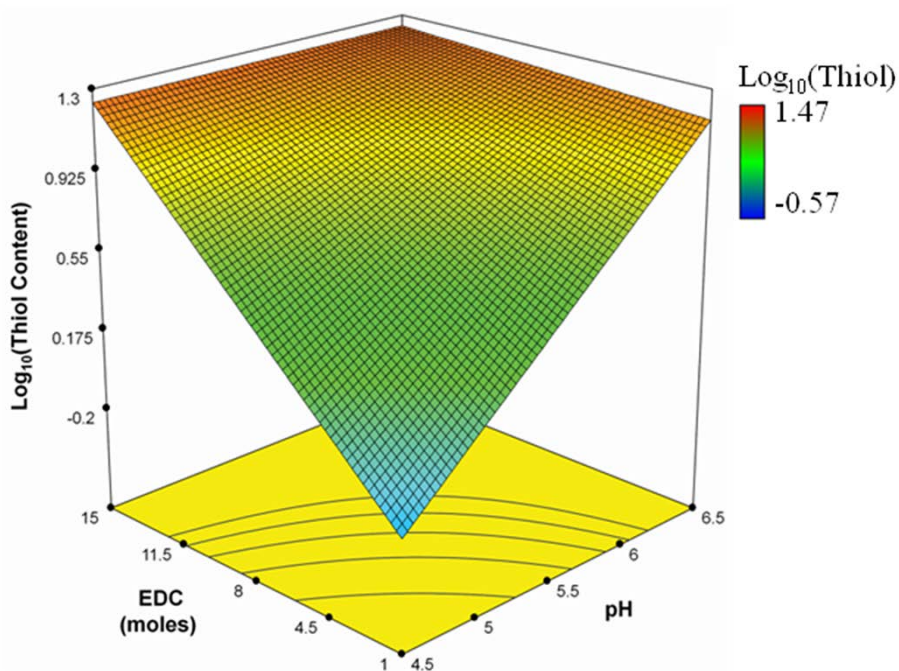


Figure B35: Model graph depicting the nature of interactions between the factors EDC and the pH of the reaction medium in response to amidation at constant values of other factors of Cys = 10 (moles), NHS = 0.1 (moles), time = 3.5 h for FF design. Note that thiol content is a surrogate for amide content.

In this study, based on the ANOVA and residual analysis, it is evident that the EDC, pH of the reaction medium and Cys are the significant single factors governing the thiolation of HA. These factors show a positive effect in the specified range, indicating the higher degree of

amidation near the maximum range of the factors. This is in agreement with the one factor analysis performed by Sehgal [5] for optimizing the amidation reaction. However, FF provides additional information on the interaction between the factors, which is not obtained through one-at-a-time factor analysis. We observed the effect of a two-factor interaction between EDC and the pH of the reaction medium to be significant. The graph for the interaction between the factors enables us to understand how the independent variables interact with one another and affect the response (Figure B5). This helps us to predict the change in response with the change in experimental conditions.

B2.3 D-optimal design of RSM

Response-surface methodology is used to evaluate the nonlinear effects of factors and search for optimum conditions to stabilize the response. This methodology is useful for quantifying the relationships between the factors and one or more responses to determine optimal conditions. Of several design in RSM, D-Optimal design maximizes the determinant of the information matrix [16, 17]. We used this design to investigate the factors affecting the response and to build empirical models for optimizing their formulations. Two significant factors considered for the analysis were EDC and Cys (Table B3). The FF results also show pH as a significant single factor affecting the response. A pH of 6.5 is considered for RSM since, statistically, pH in the range of 4.5 to 6.5 had a positive effect on the response. Also, at pH lower than 6.5, the carboxylate moieties of HA are less dissociated, which makes HA less reactive to attack the electron-deficient carbon atom of EDC. At pH higher than 6.5, hydrolysis of the intermediate may occur. The experimental results required a log transformation, indicated by the Box-Cox plot of power transforms. The results were fitted into a second-order response surface model, a quadratic fit, for which the polynomial equation is as follows:

$$\mathbf{Log_{10}(Amide\ Content) = 0.69 + (0.19 * EDC) + (0.013 * Cys) + (-0.013 * EDC^2)}$$

(Equation 34)

where 0.69 is the intercept of the data.

Analysis of RSM

The ANOVA for the results of disulfide tests indicated that the quadratic regression models were statistically significant, with an R^2 of 0.91 and no significant lack of fit (Table B4). The R^2 value indicates a good correlation between the experimental and predicted model. The adjusted R^2 that tests the goodness-of-fit of the regression equation was 0.88. Also, the model had a high F-value, 39.43, from the F-test and a *p-value* of < 0.001 . This quadratic model was graphically represented by the three dimensional response surfaces. We observed the effect of EDC and Cys, and their mutual interaction over the response from the graphs (Figure B6). Also, we noted a normal distribution of residuals with the theoretical values from the normal probability plot of residuals. We found that there are no outliers to be investigated and that the run was consistent with the rest of the data for this model using the externally studentized residual plot.

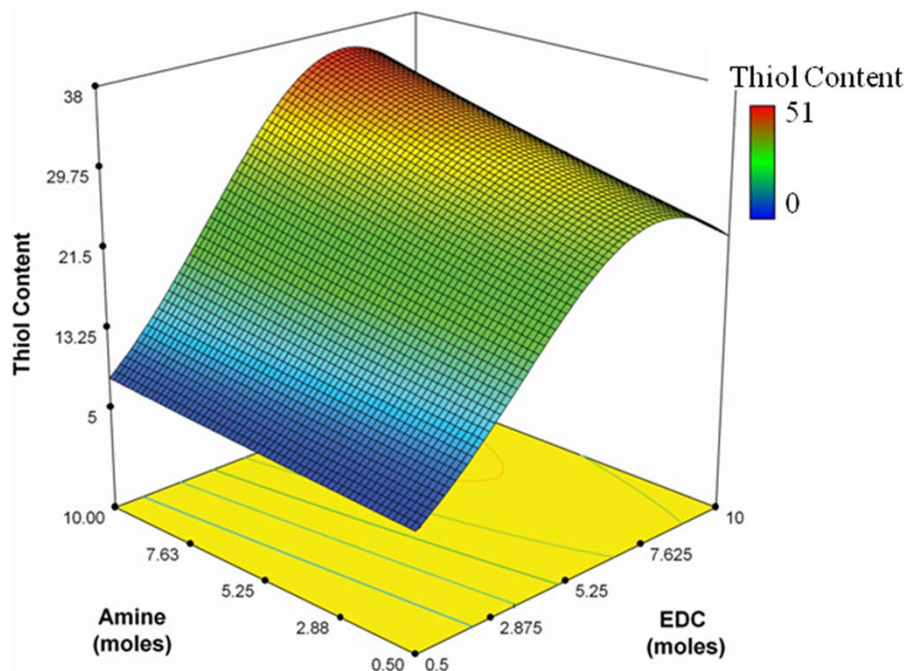


Figure B36: Model graph depicting the nature of interaction between factors EDC and Cys in response to thiol derivatization at constant values of other factors of pH = 6.5, NHS = 0.5 (moles), and time = 3.5 h D-optimal design of RSM.

From the ANOVA and the residual analysis, we observed that the significant factor controlling the amidation reaction is EDC rather than amine. As shown by analysis of the reaction mechanism (Figure B1), HA reacts with EDC to give the intermediate, *O*-acylisourea. The intermediate reacts with NHS to give a stable NHS-ester, followed by its reaction with cystamine yielding the desired product. However, this may be accompanied by certain side reactions. One of the drawbacks of the carbodiimide-based condensation is that the intermediate *O*-acylisourea can react not only with primary amine and NHS, but also with EDC and water [21-23]. The side reaction of the intermediate *O*-acylisourea with water leads to hydrolysis and decreases the efficacy of EDC. Hydrolysis of the intermediate *O*-acylisourea produces urea as the side product which can be removed by dialysis. The side reaction of the intermediate *O*-acylisourea with EDC produces the side product *N*-acylurea on the carboxyl groups, especially when excess amount of EDC is used during the reaction. In this study, the carboxyl groups are

on the backbone of HA, which makes the removal of the side product *N*-acylurea very difficult. We measured the contents of *N*-acylurea by ¹H NMR in D₂O (Figure B7). The integration from 3.1 to 3.9 ppm, which corresponds to the methine groups on the six-membered rings, was set as 10, and was used as a standard to calculate other contents.

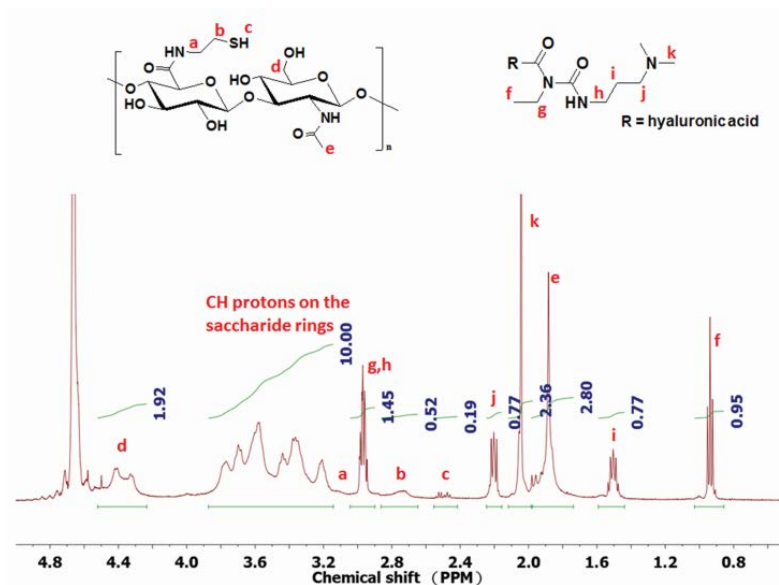


Figure B37: A characteristic ¹H NMR spectrum of amidated HA with side product

Statistically analyzing the correlation between this side reaction and the reactant formulation, the significant factors controlling the reaction are EDC and (EDC)². It follows a second order quadratic fit with a square root transformation given by the polynomial equation:

$$\sqrt{\text{Side reaction}} = 0.20 + (1.81 * \text{EDC}) + (-0.12 * \text{EDC}^2) \quad (\text{Equation 35})$$

It is evident from ANOVA that this quadratic regression model is statistically significant with p-value < 0.0001 and model F value of 56.09. The lack of fit F-value is 0.77, which implies it is not significant and the quadratic fit is apt for this model (Table B4). The graphical correlation of the side reaction with factors Amine and EDC is shown in (Figure B8). The statistical analysis also confirms that this side reaction is mainly caused by EDC, which is consistent with the

mechanism mentioned above. Another possible reaction between HA and cystamine, apart from the side reactions of intermediate, is that the terminal aldehyde group of polysaccharide in its open-chain form can react with a primary amine to form a Schiff-base [24-26]. This introduces a terminal thiol group to the HA. However, the amount of terminal aldehyde group in open-chain form is relatively small compared to the side NHS-activated carboxyl groups.

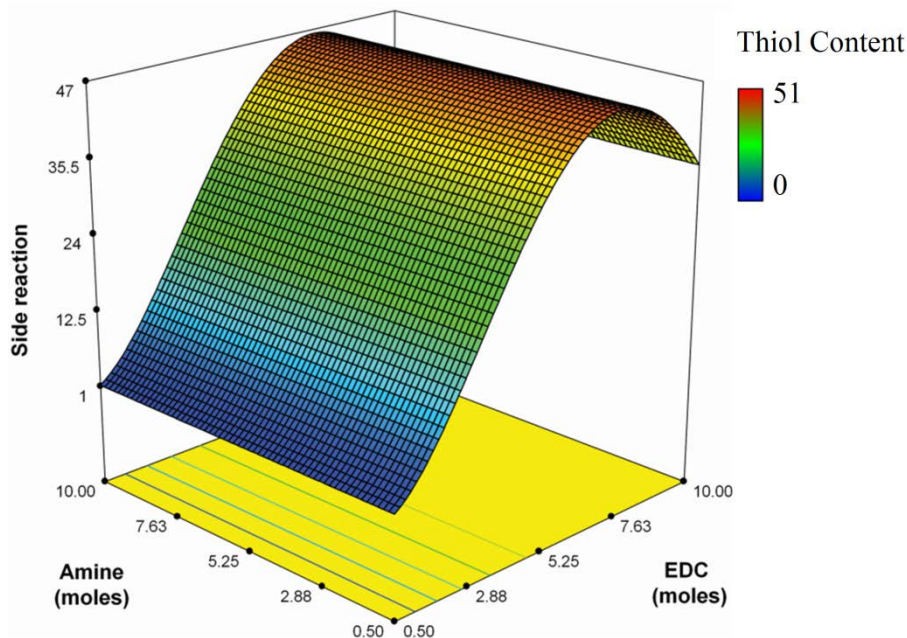


Figure B38: Model graph depicting the nature of interaction between factors EDC and Cys in response to the side reaction

In summary, EDC is the critical factor which controls the desired as well as the undesired substitution. However, since the concentration of NHS was kept constant for RSM design in this study, the effect of NHS on the side reaction is not investigated. But it is noteworthy that, using sufficient amount of NHS would be critical to suppress the formation of the side product *N*-acylurea because NHS competes with EDC to react with the intermediate *O*-acylisourea.

B2.4 Optimization of factors

The aim of this study was to optimize the amidation reaction to determine the experimental conditions and the formulations needed to synthesize HA hydrogels of a specified

degree of amidation and thus thiolation. DoE predicts the optimal formulations for carrying out the amidation reaction with the help of the polynomial model equation for any specified degree of amidation. For instance, to amidate 7.5 mole % of HA (based on repeat units) with minimal side reactions, the optimal formulation would be 0.5 moles of EDC and NHS (each) and 8 moles of Cys with the pH of the reaction medium at 6.5 for 3.5 h at 37°C. This formulation is effective in producing the desired amidation of HA with negligible side product.

B3 Conclusions

The chemical modification of HA plays a significant role in designing the scaffolds for its use in applications such as tissue engineering, targeted drug delivery via thiol-modified-HA coated gold nanoparticles, and permanent vitreous substitute with *in-vivo* gelling properties. Pre-determining the degree of derivatization of HA is critical for defining the mechanical properties of the scaffolds specific to its application. We investigated the factors controlling derivatization of HA through the carbodiimide reaction and determined the quadratic polynomial model to obtain hydrogels with desired degree of amidation. We designed the experiments and analyzed the carbodiimide reaction with the help of DoE statistics involving FF and RSM. The percentage derivatization of HA via this mechanism is dependent on the formulation of reactants and experimental conditions. Based on the formulation of the reactants, the yield of desired product and the side product can be effectively controlled. EDC is the critical factor which controls the desired as well as the undesired substitution. An adequate quadratic polynomial model for predicting the degree of thiolation and the side reaction from the response surface design is respectively:

$$\text{Log}_{10} (\text{Amide Content}) = 0.69 + (0.19 * \text{EDC}) + (0.013 * \text{Cys}) + (-0.013 * \text{EDC}^2)$$

$$\sqrt{\text{Side reaction}} = 0.20 + (1.81 * \text{EDC}) + (-0.12 * \text{EDC}^2)$$

This model can be used to design optimal formulations of the reaction to obtain the desirable degree of amidation with cystamine on HA with minimal side reaction.

References

- [1] K. Kafedjiiski, R.K. Jetti, F. Foger, H. Hoyer, M. Werle, M. Hoffer, A. Bernkop-Schnurch, Synthesis and in vitro evaluation of thiolated hyaluronic acid for mucoadhesive drug delivery, *Int J Pharm* 343(1-2) (2007) 48-58.
- [2] P.L. Lu, J.Y. Lai, D.H. Ma, G.H. Hsiue, Carbodiimide cross-linked hyaluronic acid hydrogels as cell sheet delivery vehicles: characterization and interaction with corneal endothelial cells, *J Biomater Sci Polym Ed* 19(1) (2008) 1-18.
- [3] J.W. Kuo, D.A. Swann, G.D. Prestwich, Chemical modification of hyaluronic acid by carbodiimides, *Bioconjug Chem* 2(4) (1991) 232-41.
- [4] S.N. Park, J.C. Park, H.O. Kim, M.J. Song, H. Suh, Characterization of porous collagen/hyaluronic acid scaffold modified by 1-ethyl-3-(3-dimethylaminopropyl)carbodiimide cross-linking, *Biomaterials* 23(4) (2002) 1205-12.
- [5] D. Sehgal, I.K. Vijay, A method for the high efficiency of water-soluble carbodiimide-mediated amidation, *Anal Biochem* 218(1) (1994) 87-91.
- [6] H. Cao, S.Y. Xu, EDC/NHS-crosslinked type II collagen-chondroitin sulfate scaffold: characterization and in vitro evaluation, *J Mater Sci Mater Med* 19(2) (2008) 567-75.
- [7] N. Davidenko, J.J. Campbell, E.S. Thian, C.J. Watson, R.E. Cameron, Collagen-hyaluronic acid scaffolds for adipose tissue engineering, *Acta Biomater* 6(10) (2010) 3957-68.
- [8] T.W. Wang, M. Spector, Development of hyaluronic acid-based scaffolds for brain tissue engineering, *Acta Biomater* 5(7) (2009) 2371-84.
- [9] F. Everaerts, M. Torrianni, M. Hendriks, J. Feijen, Quantification of carboxyl groups in carbodiimide cross-linked collagen sponges, *J Biomed Mater Res A* 83(4) (2007) 1176-83.
- [10] T. Taguchi, T. Ikoma, J. Tanaka, An improved method to prepare hyaluronic acid and type II collagen composite matrices, *J Biomed Mater Res* 61(2) (2002) 330-6.
- [11] H.T. Peng, M.D. Blostein, P.N. Shek, Experimental Optimization of an In Situ Forming Hydrogel for Hemorrhage Control, *Journal of Biomedical Materials Research Part B-Applied Biomaterials* 89B(1) (2009) 199-209.
- [12] P.M. Narayan, D. Marchant, M.A. Wheatley, Optimization of spray drying by factorial design for production of hollow microspheres for ultrasound imaging, *Journal of Biomedical Materials Research* 56(3) (2001) 333-341.

- [13] Y. Ma, Y. Zhang, S. Zhao, Y. Wang, S. Wang, Y. Zhou, N. Li, H. Xie, W. Yu, Y. Liu, W. Wang, X. Ma, Modeling and optimization of membrane preparation conditions of the alginate-based microcapsules with response surface methodology, *J Biomed Mater Res A* 100(4) (2012) 989-998.
- [14] M. Abul Kalam, Y. Sultana, A. Ali, M. Aqil, A.K. Mishra, I.A. Aljuffali, A. Alshamsan, Part I: Development and optimization of solid-lipid nanoparticles using Box-Behnken statistical design for ocular delivery of gatifloxacin, *Journal of Biomedical Materials Research Part A* 101(6) (2013) 1813-1827.
- [15] B. Nottelet, E. Pektok, D. Mandracchia, J.C. Tille, B. Walpoth, R. Gurny, M. Moller, Factorial design optimization and in vivo feasibility of poly(epsilon-caprolactone)-micro- and nanofiber-based small diameter vascular grafts, *Journal of Biomedical Materials Research Part A* 89A(4) (2009) 865-875.
- [16] P. Valencia, I. Cornejo, S. Almonacid, A.A. Teixeira, R. Simpson, Kinetic Parameter Determination for Enzyme Hydrolysis of Fish Protein Residue Using D-optimal Design, *Food and Bioprocess Technology* 6(1) (2013) 290-296.
- [17] B. Motealleh, P. Zahedi, I. Rezaeian, M. Moghimi, A.H. Abdolghaffari, M.A. Zarandi, Morphology, drug release, antibacterial, cell proliferation, and histology studies of chamomile-loaded wound dressing mats based on electrospun nanofibrous poly(epsilon-caprolactone)/polystyrene blends, *Journal of Biomedical Materials Research Part B-Applied Biomaterials* 102(5) (2014) 977-987.
- [18] S. Santhanam, J. Liang, R. Baid, N. Ravi, Investigating thiol-modification on hyaluronan via carbodiimide chemistry using response surface methodology, *Journal of Biomedical Materials Research Part A* 103(7) (2015) 2300-2308.
- [19] T.W. Thannhauser, Y. Konishi, H.A. Scheraga, Analysis for disulfide bonds in peptides and proteins, *Methods Enzymol* 143 (1987) 115-9.
- [20] G.L. Ellman, Tissue sulfhydryl groups, *Archives of Biochemistry and Biophysics* 82(1) (1959) 70-77.
- [21] N. Nakajima, Y. Ikada, Mechanism of Amide Formation by Carbodiimide for Bioconjugation in Aqueous-Media, *Bioconjugate Chem* 6(1) (1995) 123-130.
- [22] F. Palazon, C.M. Benavides, D. Leonard, E. Souteyrand, Y. Chevolut, J.P. Cloarec, Carbodiimide/NHS Derivatization of COOH-Terminated SAMs: Activation or Byproduct Formation?, *Langmuir* 30(16) (2014) 4545-4550.
- [23] P. Bulpitt, D. Aeschlimann, New strategy for chemical modification of hyaluronic acid: Preparation of functionalized derivatives and their use in the formation of novel biocompatible hydrogels, *J Biomed Mater Res* 47(2) (1999) 152-169.

- [24] M.Y. Lee, J.A. Yang, H.S. Jung, S. Beack, J.E. Choi, W. Hur, H. Koo, K. Kim, S.K. Yoon, S.K. Hahn, Hyaluronic Acid-Gold Nanoparticle/Interferon alpha Complex for Targeted Treatment of Hepatitis C Virus Infection, *Acs Nano* 6(11) (2012) 9522-9531.
- [25] H. Lee, M.Y. Lee, S.H. Bhang, B.S. Kim, Y.S. Kim, J.H. Ju, K.S. Kim, S.K. Hahn, Hyaluronate-Gold Nanoparticle/Tocilizumab Complex for the Treatment of Rheumatoid Arthritis, *Acs Nano* 8(5) (2014) 4790-4798.
- [26] W.J. Kim, Y. Sato, T. Akaike, A. Maruyama, Cationic comb-type copolymers for DNA analysis, *Nat Mater* 2(12) (2003) 815-820.

Curriculum Vitae

Sruthi Santhanam

sruthi.santhanam@wustl.edu

Chemical engineering doctoral candidate, who is passionate to work at the interphase of material, engineering, and biological sciences. Doctoral research focused on the development of two-component hydrogels to solve one of the major clinical problems in ophthalmology.

Education

Washington University in St. Louis 2013- 2017

Saint Louis, Missouri, USA

Ph.D. in Energy, Environmental, and Chemical Engineering **CGPA: 3.8/4**

Doctoral Thesis: Two-component Hydrogel as Biomimetic Vitreous Substitutes

Advisor: Dr. Nathan Ravi

Ph.D. Training in Ophthalmology from **Washington University School of Medicine**

Selected Courses: Introduction to Polymer Science and Engineering, Polymer blends and composites, Aquatic Chemistry, Transport Phenomena, and Biological Transport.

Anna University –Sri Venkateswara College of Engineering 2009-2013

Chennai, Tamil Nadu, India

Bachelors of Technology in Chemical Engineering **CGPA: 9.4/10**

Research Experience

Graduate Student Researcher 2013 - 2017

Project: “Development of Biomimetic Hydrogel as Vitreous Substitutes”

- Developed a reversible water-soluble polysaccharide as a biomaterial for ophthalmic use, investigated the polysaccharide modification synthesis reaction mechanism and enabled precise control of the product yield, cost, and side reactions using the statistical design of experiments (DoE).
- Developed a novel, *in-situ* forming two-component water-soluble polymer with tunable properties as a biomimetic substitute of the vitreous humor. The material addresses the major gap in vitreous substitute research and overcomes the disadvantages of the existing commercial substitutes.
- Analyzed the structure-property relationship of the two-component hydrogel using DoE, to optimize the polymer formulation that can match the optical, physical and mechanical properties of natural vitreous.
- Evaluated the bio-degradability of the composite hydrogels in contact with enzymatic solutions and ocular cell lines to assess their bio-performance.
- Collaborated with a team of vitreo-retinal surgeons, veterinary staffs, and research technicians to evaluate the biocompatibility of hydrogels on rabbit models.
- Investigated the swelling and osmotic properties of the composite polymer to understand its potential in drug delivery applications.
- Evaluated the oxygen transport through the polymeric gel using oxy-probe associated with LabView to assess their potential use in cell encapsulation.

Undergraduate Student Researcher

2010 - 2013

Project: “Biogas Upgradation – Production of Biomethane”

- Designed the industrial scale biogas upgrading plant that allows low energy consumption as well as very low methane losses using membrane separation technique.

- Designed the plant using Aspen and analyzed the economic aspects of the Upgrading Unit and compared with the available biogas plant.

Project: “Permeability set up for gas separation”

- Designed and commissioned the permeability set-up to investigate the selective gas diffusion through polymeric hollow fiber membrane.

Project: “Numerical Investigations of Impedance Response”

- Performed numerical simulations to investigate the effect of solution resistance on the large amplitude electrochemical impedance response of metal corrosion process, using MATLAB.
- Investigated the impedance spectral response of electrochemical systems to multi sine potential perturbations using numerical techniques.

Publications

- **S.Santhanam**, Y.Shui, J.Struckhoff, B.B.Karakocak, P.Hamilton, G.J. Harocopos, N.Ravi. Bioinspired Fibrillary Hydrogel with Controlled Swelling Behavior: Applicability as an Artificial Vitreous. *Biomaterials (Submitted)*
- **S.Santhanam**, J.Liang, J.Struckhoff, P.Hamilton, N.Ravi. Biomimetic Hydrogel with Tunable Mechanical Properties for Vitreous Substitutes. *Acta Biomaterialia*. (2016)
- **S.Santhanam**, J.Liang, R.Baid, N.Ravi. Investigating Thiol-Modification on Hyaluronan via Carbodiimide Chemistry using Response Surface Methodology. *Journal of Biomedical Materials Research – Part A*. (2015)
- **S.Santhanam**, V. Ramani, R. Srinivasan. Numerical Investigations of Solution Resistance Effects on Nonlinear Electrochemical Impedance Spectra. *Journal of Solid State Electrochemistry*. (2012).

Awards

- **Hot Topic Award**, Poster Presentation @ ARVO (2016)
- **University Gold Medal recipient**, First Rank holder @ Anna University (2013)
- **Outstanding Chemical Engineer Award**, Sri Venkateswara College of Engineering (2013)
- **Merit Scholarship** for two semesters, Sri Venkateswara College of Engineering (2010)
- **VICAL Award and Late Lakshmi Nandakumar Award** for Best Technical Paper Presentation, Oral Presentation @ SCHEMCON (2010)

Presentations

- **S.Santhanam**, N.Ravi. Osmotic Properties of Biomimetic Fibrillar Hydrogel as a Vitreous Substitute. ACS Fall Meeting (2017) (*Oral Presentation*)
- N. Ravi, J.Struckhoff, Y.Shui, **S.Santhanam**, P.Hamilton. Evaluation of the biocompatibility of an *in situ* forming hydrogel vitreous substitute *in vivo*: a one month study. ARVO (2016) (*Poster Presentation*)
- **S.Santhanam**, J.Liang, J.Struckhoff, P.Hamilton, N.Ravi. Biomimetic Hydrogel with Tunable Mechanical Properties for Vitreous Substitutes. MRS Fall Meeting (2015) (*Poster Presentation*)
- **S.Santhanam**, R. Baid, N. Ravi. Optimization of Thiolation for Biomimetic Vitreous Substitute. ARVO (2014) (*Poster Presentation*)
- R. Srinivasan, V. Ramani, **S. Santhanam**. Multi-Sine EIS-Drift, Non-Linearity and Solution Resistance Effects. The Electrochemical Society (ECS) Annual Meet, (2012)

Mentoring Experience

- Mentored ChemE Seniors at WashU on the fundamentals and design of chemical process and product development, using HYSIS software.
- Trained ChemE Seniors at WashU for the laboratory experiments on fluid transport, focusing on the operations of pumps and flow through the pipes.
- Guided ChemE Juniors at WashU on the concepts of mass transfer in various industrial processes, such as gas absorption, distillation, humidification, leaching, evaporation, and membrane separations.

Leadership Experience

- **Programming and Research Associate – Liberman Graduate Center at WashU:** Analyzed the graduate center and student groups' performances using Tableau, and provided recommendations to focus towards the group's mission, improve the goals, and marketing the events. Also, interacted with graduate students, addressed their questions on graduate affairs, and designed the webpage for the graduate center.
- **President for UMANG - The Indian Graduate Student Association at WashU:** Headed a team of graduate students and organized technical and cultural events throughout the academic year. Also provided logistical support, and guidance to the incoming students, managed the financial budgets of the organization, and collaborated with other groups to put-up the events.
- **Executive member of Graduate Council at WashU – Teaching and Professional Development:** Served as a student representative of the department, and reviewed the policy proposals and changes pertaining to the Graduate School. Also, voted for policy decisions focused on the scholarly development of graduate students.

- **President for IICHE-Indian Institute of Chemical Engineers at AnnaU:** Organized a National level ChemE symposium, with invited lectures from eminent professors, and research presentation from students all over India. Over 60 students participated in the symposium, delivering research talks, and taking part in other technical events. Also, interacted with established professionals in the field, and organized the seminar series.

Professional Associations

- American Chemical Society, Member (2017-2018)
- Indian Institute of Chemical Engineers, Member (2010-2013)